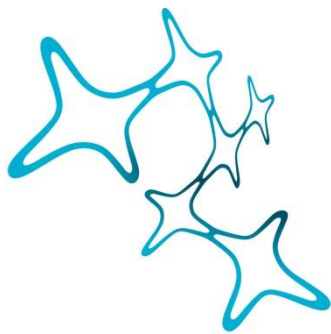


---

# COMPLEX AND SPATIALLY SEGREGATED AUDITORY INPUTS OF THE MOUSE SUPERIOR COLLICULUS

---

Veronika Bednárová



Graduate School of  
Systemic Neurosciences

LMU Munich



Dissertation der Graduate School of Systemic  
Neurosciences der Ludwig-Maximilians-Universität  
München

October, 2018

Supervisor

Prof. Dr. Benedikt Grothe

Division of Neurobiology, Department Biologie II

Ludwig-Maximilians-Universität München

First Reviewer: Prof. Dr. Benedikt Grothe

Second Reviewer: PD Dr. Conny Kopp-Scheinpflug

External Reviewer Prof. Dr. Jennifer Linden

Date of Submission: 15/October/2018

Date of Defense: 13/December/2018

## ABSTRACT

The superior colliculus (SC) is a midbrain structure, which integrates auditory, somatosensory, and visual inputs to drive orientation movements. While much is known about how visual information is processed in the superficial layers of the SC, little is known about the SC circuits in the deep layers that process auditory inputs. I therefore characterized intrinsic neuronal properties in the auditory-recipient layer of the SC (stratum griseum profundum, SGP) and confirm three electrophysiologically-defined clusters of neurons, consistent with literature from other SC layers. To determine the types of inputs to the SGP, I expressed Channelrhodopsin-2 in the nucleus of the brachium of the inferior colliculus (nBIC) and external cortex of the inferior colliculus (ECIC) and optically stimulated these pathways while recording from SGP neurons. Probing the connections in this manner, I describe a monosynaptic excitation which additionally drives feed-forward inhibition via circuits intrinsic to the SC. Moreover, I find a profound long-range monosynaptic inhibition in 100% of recorded SGP neurons, a surprising finding considering that only about 15% of SGP-projecting neurons in the nBIC/ECIC are inhibitory. The inhibitory nBIC/ECIC population of SGP-projecting neurons is to some extent parvalbumin positive. Furthermore, I find spatial differences in the cell body locations as well as axon trajectories between the monosynaptic excitatory and inhibitory inputs, suggesting that these inputs may be functionally distinct. Together with recent anatomical evidence suggesting an auditory excitation from nBIC and a GABAergic multimodal inhibition from ECIC I propose that sensory integration in the SGP is more multifaceted than previously thought.



## ACKNOWLEDGEMENTS

First and foremost, my gratitude belongs to my parents, Ol'ga and Stanislav, who have unconditionally supported my interest in Biology since I was 16 years old, perhaps without always knowing exactly what I was up to. Without their trust and support, studying in London, which ultimately set the path for the PhD here in Munich, would have remained a distant dream. Ďakujem vám mami a tati!

I am also most grateful to you, Mike Myoga, for taking me on board that autumn of 2014 and for your diligent supervision in the years since. I'll always remember that day when we physically moved to the MPI and set our feet into the empty laboratory that now contains the beastly (and sometimes gentle) microscope. With laser-protection goggles, we switched on the Mai Tai of the inherited two-photon setup room and started steering the laser through the very dangerous mirrors. Looking back now, I really did know nothing and while being the super versatile, hands-on, and extremely capable researcher and supervisor, you never took the project over completely. To me, our cooperation was always a creative process whereby I learned along the way and you provided your time, suggestions, and advice. I think without such an approach I would never have learned as much as I did. For the big days to come I wish you all the best and I hope your approach to supervision will not change. Here I also want to wish best of luck to the younger Myoga PhD student, Matthias! I also hope that our internal jokes will persevere to an unspecified time in future when we again shout out: "Eight! It is eight!" Or that someone's tick marks point inside the plot.

Thank you to Benedikt Grothe for your trust and leadership throughout my PhD. I thank you Benedikt for always having a genuine perspective and for directing me towards the important aims. Thank you for your time and your questions that always lead to further scientific endeavours.

Others deserving of thanks include the members of my TAC committee – Pieter Goltstein, Mario Wullimann, Alex Loebel, Conny Kopp-Scheinpflug and of course Benedikt and Mike. Your perspectives, unique points of view, and your critical questions were invaluable. I would like to thank Conny in particular for her advice on animal license, tracing experiments, and her suggestion to use potassium-internal solution to carry out both voltage- and current-clamp experiments.

For the generous provision of space and infrastructure to carry out this study, I am grateful to Tobias Bonhoeffer and the Department Synapses – Circuits – Plasticity at the MPI. Simon Weiler, Volker Scheuss, Tobias Rose, and Volker Staiger helped with the two-photon laser-stimulation setup and Mark Hübener helped with the animal license. Claudia Huber and Frank Voss provided further technical help. All past PhD students of the department who have showed me the reality of lab life at the beginning of my PhD. All current PhD students and postdocs of the department for their support, wealth of knowledge, inspiration, and the jolly times that have become my everyday life.

Thank you to all members of the Grothe Lab on the 3rd floor of the Biocenter. Thank you to everyone who attended the lab meetings and asked the questions that improved our line of thought and argument, especially to Lutz, Boris, Mario, Mischko, and Lars. To Grothe's Lowenzähne – the PhD students and postdocs: Although our time with each other decreased throughout the years, I cherish the time we spent together in the early years, at the Indian restaurant or at the Frida bar or playing volleyball without a net at the Teambuilding in 2018. Thank you to Matt, Jim, and Eli from Conny's lab for your help with the tracer experiments. Thank you to Hilde Wohlfrom for help with all immunohistology experiments, from designing the protocols through testing the antibodies to helping with the histological staining procedures. Thank you also to Olga Alexandrova for all antibody-specific knowledge and the constant supply of chocolate at your desk.

I extend my gratitude also to the Munich scientific community, to the MPI of Neurobiology, and to the GSN. The GSN provided financial support without which my studies would have not been possible, and supported me at FENS 2018, Neurophotonics Summer School 2015, scientific visit to Israel in 2015, and at many more other events. Thank you to the GSN administration (to Lena, Stefanie, Renate, Catherine, Raluca, and Birgit) for dealing with my issues and always having your doors open.

Thank you to the Boehringer Ingelheim Fonds for accepting me as a fellow and thus financially supporting me for two years of my PhD. I am very grateful to have been part of the BIF community and to the events yet to come.

Thank you to the very strong fast-track/master/PhD 2013 GSN year (Alex, Vilim, Elena, Judi, Jaime, Oriol, Isa, Laura, Ksenia, Sara) and all associates of this wonderful group (Anna, Niko, Lili) for the good and the bad times, the mirrors you have set for my self-reflection, the relentless discussions on all current and old topics, the lunches, the events, the dinners and the community. Thank you Sara, Anna, and Martin, the past and current Klingerstrasse WG crew (Je mehr wir zu Hause Deutsch sprechen, desto besser wird mein Deutsch!).

On a more personal level, I want to thank Judi and Ksenia, the Trinity. Without you, these pages would have been empty. (Ha-ha!) On a serious note, thank you for always being there and for liking me for who I am.

Lastly, thank you to Marc, My Dear.





# TABLE OF CONTENTS

ABSTRACT .....	iii
ACKNOWLEDGEMENTS.....	v
LIST OF FIGURES.....	xiii
LIST OF TABLES.....	xv
LIST OF ABBREVIATIONS .....	xvii
INTRODUCTION .....	1
1.1 Navigation, orientation, and superior colliculus .....	1
1.2 Coding for space in the superior colliculus .....	3
1.3 Multisensory processing in the superior colliculus.....	9
1.4 Literature review of intrinsic and extrinsic SC circuits.....	11
1.4.1 Visual SC circuits .....	13
1.4.2 Integrative SC circuits and the SC output.....	17
1.4.3 Somatosensory SC circuits.....	22
1.4.4 Auditory SC circuits .....	23
1.5 Motivation to study the SC and the objectives of PhD thesis .....	27
MATERIALS AND METHODS .....	29
2.1 Ethical approval.....	29
2.2 Stereotactic injections .....	29
2.3 Acute superior colliculus slices .....	32
2.4 Electrophysiology .....	32
2.5 Current-clamp experiments .....	33
2.6 Laser stimulation setup.....	34
2.7 Voltage-clamp/photostimulation experiments.....	34
2.8 Synaptic current analysis.....	35
2.9 Analyses of direct excitation and inhibition distribution differences.....	36
2.10 Distinguishing polysynaptic and monosynaptic inhibitory inputs .....	37
2.11 Analysis of intrinsic electrophysiological properties .....	38
2.12 Analysis of the strength of direct inhibition on SGP cell clusters .....	39

2.13 Analysis of somatodendritic morphology .....	39
2.14 Immunohistochemistry .....	40
2.15 Confocal microscopy .....	42
2.16 Analysis of confocal images and cell counting.....	42
RESULTS .....	43
3.1 Electrophysiological and morphological characterization of cell types in the SGP layer of the mouse SC .....	43
3.1.1 Three electrophysiologically-defined cell types populate the SGP of the mouse SC.....	43
3.1.2 SGP cell types exhibit distinct orientation of dendrites .....	46
3.1.3 Conclusion .....	48
3.2 Anatomical and functional connectivity of the nBIC/ECIC and the SGP of the mouse SC .....	49
3.2.1 Anatomical projection of the nBIC/ECIC to the SGP in the mouse confirmed by tracer injection.....	49
3.2.2 AAV-based ChR2 vectors effectively transduce nBIC/ECIC neurons .....	51
3.2.3 Photoactivatable nBIC/ECIC neurons after the AAV.eYFP.ChR2 injection .....	52
3.2.4 Optically-induced postsynaptic currents in the SGP neurons reveal diverse inhibitory connections from the nBIC/ECIC .....	54
3.2.5 Direct inhibition from the nBIC/ECIC reaches all three types of SGP neurons .....	60
3.2.6 Difference in the distribution of direct excitatory and inhibitory nBIC/ECIC axons.....	65
3.2.7 Physiological approach to finding differences in spatial distribution between excitatory and inhibitory neuron bodies in the nBIC/ECIC.....	71
3.2.8 Anatomical approach to finding distribution differences between excitatory and inhibitory neuron bodies in the nBIC/ECIC .....	74
3.2.9 The majority of inhibitory nBIC/ECIC SGP-projecting neurons are PV positive .....	76
3.2.10 Conclusion .....	77
3.3 Anatomical and functional connectivity of PV nBIC/ECIC neurons with the SGP of the mouse SC .....	79
3.3.1 PV is expressed in somas and axons of the mouse nBIC/ECIC neurons ..	79

3.3.2 Putative PV neurons in the nBIC/ECIC provide direct inhibition but also excitatory synaptic connection to the SGP .....	80
3.3.3 The PV <sup>cre!</sup> mouse line does not drive expression in an exclusive population of PV neurons in the nBIC/ECIC .....	88
3.3.4 Conclusion .....	90
3.4 Multisensory integration in the SGI.....	91
DISCUSSION .....	93
4.1 Cell types within the SGP.....	93
4.2 Input circuitry from the nBIC/ECIC to the SGP .....	94
4.3 Spatially distinct excitatory and inhibitory inputs from the nBIC/ECIC to the SGP.....	97
4.4 Functional implications of a direct inhibitory nBIC/ECIC input to the SC.....	98
4.5 Methodological limitations .....	100
4.6 Outlook and future applications .....	103
4.7 Conclusions .....	106
REFERENCES.....	109
PUBLICATION.....	123
CURRICULUM VITAE .....	125



## LIST OF FIGURES

Figure 1.1 The mammalian superior colliculus – overview.....	3
Figure 1.2 Movement vectors for eye deviation expected in some compartments of the cat AChE staining pattern in the SC .....	5
Figure 1.3 Auditory coding principles in the primates and other mammals.....	8
Figure 1.4 The honeycomb-like model after AChE staining in the rat intermediate SC overlaying the SGP .....	12
Figure 1.5. The visual SC circuits - cell types and their projection targets.....	15
Figure 1.6 Scheme of the main motor targets of the SC.....	20
Figure 1.7 Scheme of modular/extramodular ECIC.....	26
Figure 3.1 Identification of three SGP neuron types on the basis of their electrophysiological properties.....	44
Figure 3.2 Identification of three SGP neuron types on the basis of their morphological properties .....	47
Figure 3.3 Anatomical tracing of the nBIC/ECIC connections with the SGP layer in the SC.....	51
Figure 3.4 AAV-based eYFP.ChR2 expresses in the nBIC/ECIC and their axons in the SGP .....	52
Figure 3.5 Optical activation of ChR2 positive neurons in the nBIC/ECIC.....	54
Figure 3.6 Optical activation of ChR2 positive axons in the nBIC/ECIC-SGP circuit.....	56
Figure 3.7 Comparison of IPSC amplitudes to distinguish polysynaptically from monosynaptically-induced inhibitions in SGP neurons .....	59
Figure 3.8 Hierarchical clustering analysis of SGP neurons with direct inhibition ....	63
Figure 3.9 Strength of direct inhibition on SGP neurons cell type-wise and stimulation position-wise .....	65
Figure 3.10 ChR2-assisted circuit mapping of the nBIC/ECIC - SGP circuit.....	67
Figure 3.11 Mapping the locations of the excitatory and the inhibitory nBIC/ECIC inputs to SGP neurons.....	70
Figure 3.12 ChR2-assisted circuit mapping of SGP-projecting cell bodies located in the nBIC/ECIC using ChR2-eYFP.Kv2.1 .....	72
Figure 3.13 More examples of ChR2-assisted circuit mapping of SGP-projecting cell bodies located in the nBIC/ECIC using ChR2-eYFP.Kv2.1 .....	74
Figure 3.14 Retrogradely traced nBIC/ECIC neurons and their immunoreactivity for GAD67 and calretinin.....	75
Figure 3.15 PV positivity in the rostrocaudal extent of the IC to the SC in a WT CBA/Caj mouse .....	80
Figure 3.16 Histological investigation of tdTomato positivity after the injection of Flex.ChR2.tdTomato into PVcre! mouse line .....	81
Figure 3.17 Postsynaptic voltage-clamp recording of PV optical activation in a SGP neuron number 1, showing PV-mediated inhibition only .....	83

Figure 3.18 Postsynaptic voltage-clamp recording of PV optical activation in a SGP neuron number 2, showing PV-mediated excitation only .....	85
Figure 3.19 Postsynaptic voltage-clamp recording of PV optical activation in a SGP neuron number 3, showing PV-mediated excitation and inhibition.....	87
Figure 3.20 tdTomato positive nBIC/ECIC neurons and their colocalization with PV antibody.....	89
Figure 3.21 tdTomato positive nBIC/ECIC neurons and their colocalization with GAD67 antibody .....	89
Figure 3.22 Example SGI recording of auditory/multisensory and visual stimulation .....	92
Figure 4.1 Proposed scheme of the nBIC/ECIC projections into the mouse SC.....	96

## LIST OF TABLES

Table 1   Coordinates of stereotactic injections	31
Table 2   List of main reagents used for immunochemistry	41
Table 3   Numbers and percentage of retrogradely labelled neurons GAD67 immunopositive	76
Table 4   Numbers and percentage of retrogradely labelled neurons calretinin immunopositive	76
Table 5   Numbers of retrogradely labelled cells calbindin immunopositive	77
Table 6   Numbers of retrogradely labelled neurons PV immunopositive	77
Table 7   Number and percentage of tdTomato and PV positive nBIC/ECIC neurons	90
Table 8   Number and percentage of tdTomato and GAD67 positive nBIC/ECIC neurons	90





## LIST OF ABBREVIATIONS

AAV	adeno-associated virus
AChE	acetylcholinesterase
aCSF	artificial cerebrospinal fluid
AMPA	$\alpha$ -amino-3-hydroxy-5-methyl-4-isoxazolepropionic acid receptor
AOI	arbour orientation index
AP	action potential
CG	central grey
ChAT	choline acetyltransferase
ChR2	Channelrhodopsin-2
cMRF	central mesencephalic reticular formation
DCN	dorsal column nuclei
ECIC	external cortex of the inferior colliculus
EPSP/C	excitatory postsynaptic potential/current
eYFP	enhanced yellow fluorescent protein
FEF	frontal eye field
GABA	gamma-aminobutyric acid receptor
GAD	glutamate decarboxylase
HRP	horseradish peroxidase
IC	inferior colliculus
ICC	central nucleus of the inferior colliculus
ILD	interaural level difference
InC	interstitial nucleus of Cajal
IPSP/C	inhibitory postsynaptic potential/current
ISI	inter-spike interval
ITD	interaural time difference

LGN	lateral geniculate nucleus
LL	lateral lemniscus
LP	lateral posterior nucleus of the thalamus
ME	multisensory enhancement
MD	multisensory depression
MdRF	medullary reticular formation
MGB	medial geniculate body
MPRF	medial pontine reticular formation
MT	middle temporal cortex
nBIC	nucleus of the brachium of the inferior colliculus
NF	narrow-field neurons
NMDA	<i>N</i> -methyl- <i>D</i> -aspartate receptor
nPC	nucleus of the posterior commissure
nPH	nucleus prepositus hypoglossi
PBg	parabigeminal nucleus
PBS	phosphate-buffered saline
PFA	paraformaldehyde
PPRF	paramedian reticular formation of the pons
PV	parvalbumin
RGC	retinal ganglion cell
riMLF	rostral interstitial nucleus of the medial longitudinal fasciculus
RIP	nucleus raphe interpositus
rpIC	rostral pole of the inferior colliculus
SAI	stratum album intermediale
SAP	stratum album profundum
SC	superior colliculus

SIG	stratum griseum intermediale
SGP	stratum griseum profundum
SGS	stratum griseum superficiale
SNr	substantia nigra pars reticulata
SO	stratum opticum
SOC	superior olivary complex
SZ	stratum zonale
TRITC	tetramethylrhodamine
WF	wide-field neurons
WT	wild-type



*Dedicated to my parents*



---

# INTRODUCTION

---

## 1.1 NAVIGATION, ORIENTATION, AND SUPERIOR COLLICULUS

Orientation towards behaviourally relevant stimuli is essential for navigation and thus crucial to survival of all living creatures. Animals employ different senses and behaviours to orient towards salient objects. For example, the barn owl relies entirely on audition to orient the head and to hunt prey in darkness. Humans and other primates rely on multiple senses to orient themselves in the environment. To illustrate, imagine a lecture hall full of students. After the lecture has already started a student enters the hall through the side door. Naturally, the listeners make a saccade (fast eye movement towards the target) to centre the tardy student in the middle of their visual fields. However, if the student was not visible, for example if he entered through the back door that makes a terrible creaking noise, the auditory system would detect the noise and direct the entire upper body towards back of the hall. Thus, we employ multiple senses in concert to inform the brain of the ever-changing world.

Early lesion studies of the superior colliculus (SC) pointed towards the involvement of this brain structure in orientation behaviour (Sprague & Meikle, 1965). The SC is located in the midbrain (Fig. 1.1a) and is well conserved amongst species (commonly called the optic tectum in non-mammalian vertebrates). In cats for example, unilateral lesioning of the SC showed circling behaviour towards the lesioned side and a profound neglect for stimuli presented on the contralateral side (Sprague & Meikle, 1965). Furthermore, SC electrical activation studies in primates demonstrated its involvement in generating head turns and eye movements (Schiller & Stryker, 1972), arm-reaching movements (Lünenburger *et al.*, 2001), and attentional shifts, while in other species it is

involved in further orientation behaviours, such as upper-body turns in rats or fang-strikes in snakes (Tehovnik, 1989). Thus, the SC is implicated in sensory-to-motor transformation and coordinates various orientation behaviours of the head and the upper body (Fig. 1.1b).

Years of research of how the SC achieves such functionality have uncovered increasingly more of its operational principles (for review see May, 2006). It is now well known that the sensory inputs entering the SC are segregated, with the visual information reaching the superficial layers while the somatosensory and auditory inputs reach the deep SC layers (Fig. 1.1c). These inputs converge on neurons in the intermediate layers which project to different motor centres in order to perform appropriate behavioural responses. The intermediate SC neurons are under the control of the cortex and the basal ganglia. Furthermore, neuromodulatory circuits have been implicated to modulate the SC activity. It has been proposed that the SC integrates spatial information from multiple senses and possibly generates a map of motor error between where an object is located in space and where the head/eyes/upper body are presently oriented. However, there are still many open questions regarding the spatial coding of various sensory parameters and their integration on a single-cell level.



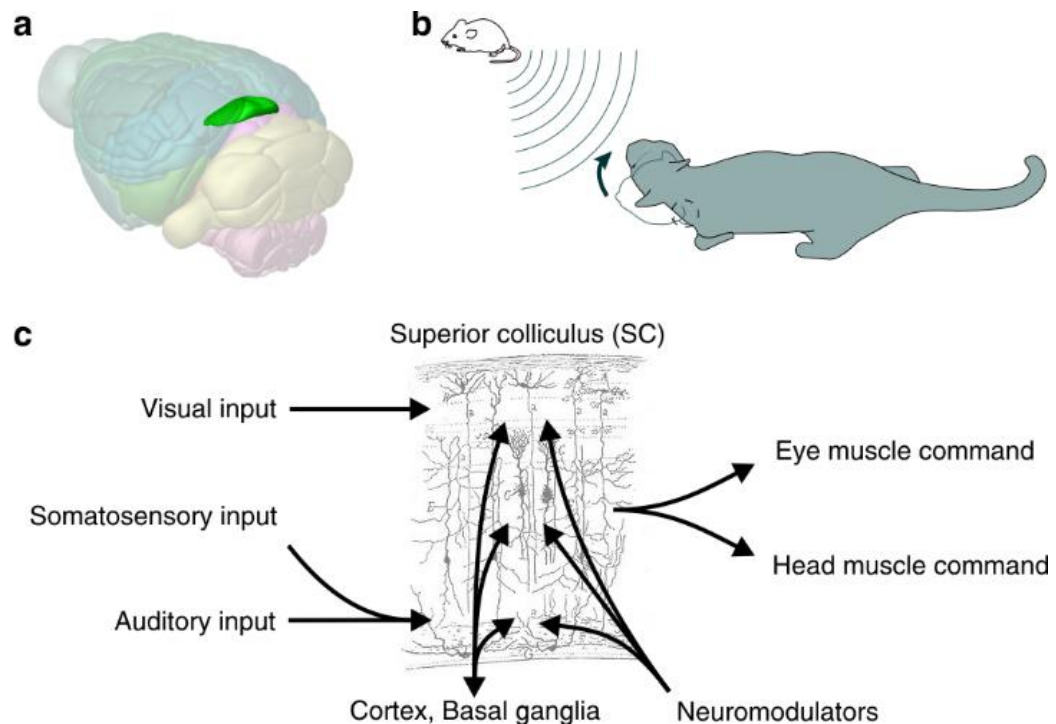


**Figure 1.1 The mammalian superior colliculus – overview**

**a**, The location of the SC (in green) in the brain of the mouse (adapted from the Allen Brain Atlas – Brain Explorer). **b**, Scheme showing SC function in orientation. The cat (in grey) makes a head turn to orient the head and the upper body towards the interesting object in space – the mouse (in white). **c**, Overview of the general input and output organization of the mammalian SC. The retinal inputs target superficial SC while somatosensory and auditory inputs target deep SC. The information they provide gets integrated in intermediate layers which project to motor nuclei of the head and the eyes to initiate movement. Such sensory-to-motor transformation is under the control of the cortex and the basal ganglia and is modulated by various neuromodulatory inputs. Adapted from Ramón y Cajal’s drawing of the SC (Cajal, 1888).

## 1.2 CODING FOR SPACE IN THE SUPERIOR COLLICULUS

Space perception may seem trivial to perform, but it is a tremendous computational challenge for the brain, considering that each sense is mapped differently in its corresponding sensory epithelium (i.e. position on the retina for vision and area of the skin for somatosensation). The situation more complicated in the auditory system where the position of an auditory object is not directly

mapped onto the cochlea. The brain must resolve these variant parameters in order to incorporate them into a coherent representation of the world. Moreover, it must maintain this coherence during animal's dynamic interaction with its environment.

The findings that the retinal and somatosensory projections to the various laminae of the SC are anatomically topographically organized (Graybiel, 1975; Drager & Hubel, 1976; Benedetti, 1991) suggested that a functional topography of the converging inputs exists. Indeed, visual and somatosensory spatial maps were found to be in functional register in the SC (Drager & Hubel, 1975, 1976; Stein *et al.*, 1975), where the rostral SC represents frontal visual field and the face, while the caudal SC represents the periphery and the back, thereby coding for azimuth along the rostrocaudal SC axis. Similarly, the medial SC represents the upper visual field and the upper parts of the body, while the lateral SC the lower visual field and the lower parts of the body, thereby coding for elevation along the mediolateral SC axis. These sensory spatial maps converge onto a motor map, best understood in terms of saccades from nonhuman primate studies. Neurons in the motor parts of the SC are tuned to trigger a saccade of a particular direction and amplitude (not to a particular location in space) (Schiller & Stryker, 1972). It has been hypothesized that such a representation provides a motor error signal (Sparks, 1986) which initiates a motor shift in order for the eyes to be directed to a particular target. How the error signal gets computed, however remains elusive. The motor part of the SC displays a striking organization when stained against acetylcholinesterase (AChE). The pattern of this organization resembled honeycomb and divides the SC into dorso-ventrally oriented columns. A hypothesis has been brought forward that each of the columns codes for a particular saccade direction (Fig. 1.2).

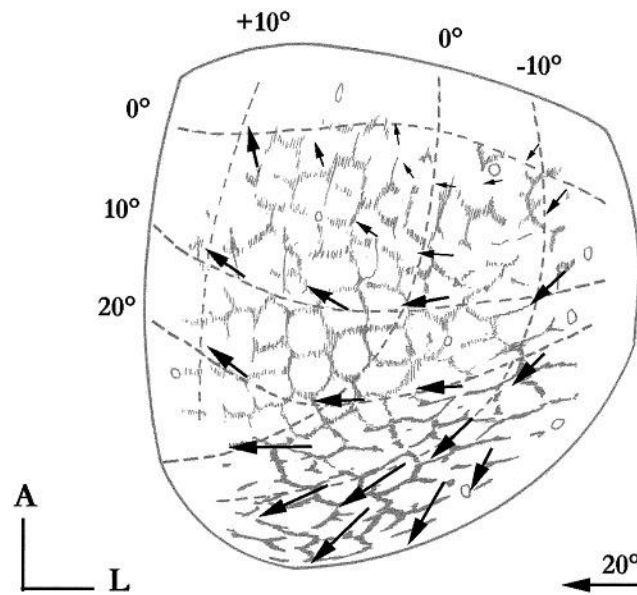


**Figure 1.2** Movement vectors for eye deviation expected in some compartments of the cat AChE staining pattern in the SC

The arrows represent the eye saccades one would expect assuming that the activity in a given SC column evokes a saccade which brings the gaze to the point of the visual field. This visual field is retinotopically projected to the same SC column that was activated. A, anterior; L, lateral. With permission from Chevalier & Mana (2000).

The involvement of the SC in perceptual continuity across saccades was well studied in primates and has been recently reviewed (Wurtz, 2018). In order to analyse visual scenes, animals perform numerous saccades of various directions and amplitudes to foveate onto specific features of the scene. The image displacement that each saccade produces is however not perceived. Rather it is perceived as a smooth visual transition during saccades and visual stability (together termed visual continuity). Two circuits involving the SC are implicated in this process and involve a copy of the SC signal for saccade production (termed corollary discharge) transmitted to thalamo-cortical circuits. First, a projection from the intermediate SC via the lateral edge of the medial dorsal thalamus to the frontal eye field (FEF) sends a copy of the presaccadic burst activity to the thalamo-cortical centres. Second, the superficial SC circuit via the pulvinar to the

middle temporal cortex (MT), sends information on saccadic suppression. These circuits work together to control the production of saccades and reduce the blur during saccades.

Topographical auditory space coding is much less trivial to understand because the position of an auditory object is not directly encoded in the cochlea. Unlike in the visual and the somatosensory systems, where positional information is mapped directly onto the sensory periphery, only frequency is mapped onto the cochlea, and frequency by itself carries no positional information. The auditory space must therefore be calculated completely within the brain. The cues that provide spatial information about auditory objects (interaural level differences (ILDs), interaural time differences (ITDs), and spectral notches of the pinnae) are very well known (Grothe *et al.*, 2010; Grothe & Pecka, 2014). It remains debated however, how the brain interprets these cues in order to form a coherent percept of the auditory space.

Much of what we know about auditory spatial coding we know from experiments performed in the barn owl. In the 80s the Knudsen laboratory showed the existence of an auditory spatial map in the optic tectum of the barn owl which was also in a considerable register with the visual map (Knudsen & Konishi, 1978; Knudsen, 1982). The optic tectum in the barn owl inherits the spatial map from its primary auditory input, the external cortex of the inferior colliculus (IC) (Knudsen & Knudsen, 1983). The barn owls however, are not mammals. Primate literature on the other hand suggests that maps might not be the preferred auditory spatial coding principle for primate SC (Maier & Groh, 2009; Lee & Groh, 2014) (Fig. 1.3, right). Here, SC neurons exhibit open-ended response pattern upon auditory stimulation which is more consistent with a rate code (and not with a map/place code). In addition, in other auditory brain structures, rate code has been suggested for auditory spatial representation (for review see Grothe, 2003; Grothe *et al.*, 2010; Grothe & Pecka, 2014). Here, the

auditory space is thought to be represented by the relative activity of two hemispheric populations of neurons and not by a single-cell coding of a particular position (labelled line code).

Intriguingly, reports of auditory spatial maps in the superior colliculus of several other non-primate mammalian species have been published (Palmer & King, 1982; Middlebrooks & Knudsen, 1984; King & Hutchings, 1987; Gaese & Johnen, 2000) (Fig. 1.3, left), making the non-primate mammalian SC possibly an outlier in auditory spatial coding strategies. In the reported auditory spatial maps, the azimuth is represented in the rostro-caudal SC and the elevation on the medio-lateral SC axis, a representation that is in register with the visual maps.

How does the SC build such an auditory spatial map? Does it inherit it from its major auditory input, the nucleus of the brachium of the inferior colliculus (nBIC), or does it build it from the auditory cues, the ITDs, the ILDs, and the spectral notches? It was reported that the ITDs, which are the cues used to detect the location of a sound source for low frequency sounds, do not contribute to the auditory spatial map (Campbell *et al.*, 2006), making the high frequencies an important point. The spectral cues are directionally sensitive, making higher frequencies restricted to lateral/pinna-directed orientations (Carlile & Pettigrew, 1987; Middlebrooks & Knudsen, 1987). In addition, most studies that reported a map of auditory space in the SC used broadband auditory stimuli which contained both high and low sound frequencies. Thus, a combination of these factors could mistakenly report a high frequency tuned SC neuron (activated by high frequency in the broadband sound stimulation presented) to have a 'place code' of a lateral location at the pinna (this region would be high-frequency restricted due to the spectral filtering of the pinna). Here, the question at hand is whether the frequency tuning of the SC neurons could provide a mechanism by which the SC can encode spectral cues which are generated in the auditory periphery. In addition, it is important to note that the

nBIC, the main auditory input of the SC in the mammals, was not found to contain a map of auditory space (Schnupp & King, 1997). It is thus unclear how the apparent auditory spatial map in the mammalian SC is generated and there is a need for a thorough reinvestigation of the relationship between spatial and frequency tuning of SC neurons.

To conclude, while map-like spatial coding is advantageous to somatic and visual spatial representations, the auditory spatial representation in the mammalian SC might employ a different code as the primate literature suggests and thus research should revisit spatial auditory coding in the mammalian SC.

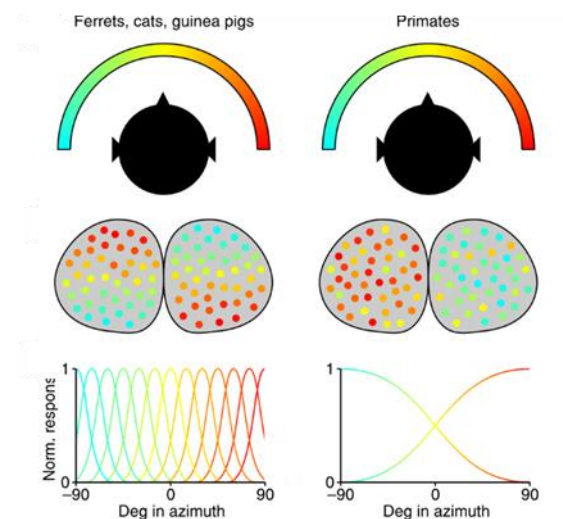


**Figure 1.3 Auditory coding principles in the primates and other mammals**

In ferrets, cats and guinea pigs, current literature suggests the existence of a place code in the SC (left). In the place code, all locations along the azimuth are encoded topographically in each SC hemispheres and SC neurons have best responses for a particular azimuth location. In primates, the literature suggests the existence of a rate code (right). The object location is represented by relative firing of a population of SC neurons in the contralateral hemisphere.

### 1.3 MULTISENSORY PROCESSING IN THE SUPERIOR COLLICULUS

It is generally accepted that multiple senses must be integrated in order to create a coherent representation of our world. The term 'multisensory integration' has been consistently defined in literature in terms of behavioural responses or the number of action potentials a neuron fires, which were statistically different when a single sensory modality versus multiple sensory modalities were presented (Stein & Stanford, 2008).

One constantly used measure of multisensory integration across the literature is multisensory enhancement (ME), where the response to a multimodal stimulus is greater than the sum of the responses to the individual sensory modality stimuli. In terms of behavioural responses, ME is characterized by enhanced accuracy and speed of stimulus localization (for review see Stein *et al.*, 2014). In terms of single-cell responses, ME is described as increased number of action potentials and supralinear integration (when modalities are combined, the number of action potentials exceeds the linear sum of when the modalities were presented alone). The opposite can be the case at both behavioural and cellular level, termed multisensory depression (MD). In terms of behaviour, MD is described as a failure to move or as an approach to the wrong location. At single-cell level, the response to a multimodal stimulus is lower than the sum of the responses to the individual sensory modality stimuli.

Seminal papers from the laboratory of Barry E. Stein identified ME and MD on both behavioural and single-cell level in the SC of the cat. Behaviourally, the orientation to visual cues in the cat was affected by auditory stimuli with both ME and MD present, results strikingly similar to the electrophysiological single-cell SC recordings (Stein *et al.*, 1989). Single multisensory neurons in the SC produced ME and MD when visual, auditory, or somatosensory inputs were

activated together, providing evidence for multisensory integration in single SC neurons (Meredith & Stein, 1986). Three guiding principles of multisensory integration have been postulated since (for review see Stein *et al.*, 2014). Spatial (1) and temporal (2) register of multi-modal cues generally enhances the response of multisensory neurons, while depression occurs in the case when the cues are temporally and spatially disparate. For weakly effective sensory stimuli, the integration follows an ‘inverse effectiveness’ principle (3), in which weaker stimuli, when combined, produce greater ME or MD effects than sensory stimuli that are strongly effective on their own.

Recently, and for the first time, a behavioural and cellular mechanism for the third multisensory integration principle, the inverse effectiveness, has been described in the tadpole optic tectum (Truskowski *et al.*, 2017). Behaviourally, pairing a weak mechanosensory with low-contrast visual stimulation induced changes in swimming speed in a nonlinear fashion. On a single-cell level, a combined electrical stimulation of the optic chiasm (visual input) and the contralateral hindbrain (mechanosensory input) evoked single-cell ME nonlinearly amplified responses in the optic tectum when the stimuli alone were weak (termed subthreshold, i.e. not evoking action potentials). The authors furthermore showed that such nonlinear amplification of subthreshold inputs involves the recruitment of *N*-methyl-D-aspartate (NMDA) receptors. On the other hand, an *in vitro* study in the rat brain slices showed that multi-modal electrical stimulation of the auditory and visual pathways evoked single-cell subthreshold SC responses that summed linearly (Skaliora *et al.*, 2004). Thus, the studies of subthreshold multisensory integration processes have so far provided inconsistent results. There is insufficient research into the processes underlying ME in terms of the number of action potentials (superthreshold summation), leaving the cellular and circuit mechanisms of multisensory integration an enigma in the field.



## 1.4 LITERATURE REVIEW OF INTRINSIC AND EXTRINSIC SC CIRCUITS

The mammalian SC is composed of well-defined, alternating grey and white layers (May, 2006). In a transverse brain section, the layer located most superficially is called stratum zonale (SZ), and although its definition is disputed and sometimes it is left out, it is densely packed with small cells. Immediately underneath lies the stratum griseum superficiale (SGS), which is often divided into two or even three sublaminae (2: Kanaseki & Sprague, 1974; 3: Albano *et al.*, 1979; 3: Major *et al.*, 2000). Beneath the SGS lies the most prominent SC layer, the stratum opticum (SO), which contains mostly axons of the retinal ganglion cells (RGCs). The SZ, SGS and SO are commonly called the superficial SC. Further ventrally begins the stratum griseum intermediale (SGI) with two sublaminae: the cellular SGIa (or upper SGI) and the SGIb (or lower SGI) which contains rostrocaudally running fibres (Kanaseki & Sprague, 1974; Helms *et al.*, 2004). Ventral from the SGI is the stratum album intermediale (SAI), a fibrous layer with a very small number of cells. The SGI and SAI are commonly referred to as the intermediate SC. A honeycomb-like pattern of staining against AChE can be observed in the SGI and SAI but no other SC layers (Fig. 1.4) (Chevalier & Mana, 2000). This pattern was suggested to reflect the modular organization for generation of orienting movements (already discussed in the Subsection 1.2).

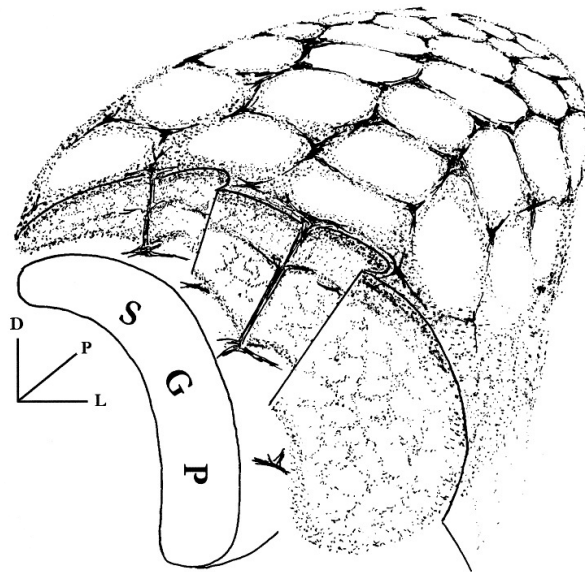


**Figure 1.4 The honeycomb-like model after AChE staining in the rat intermediate SC overlaying the SGP**

D, dorsal; P, posterior; L, lateral; SGP, stratum griseum profundum. With permission from Chevalier & Mana (2000).

Below the intermediate SC lies the stratum griseum profundum (SGP) which contains loosely arranged cells (Fig. 1.4). The innermost thin fibrous layer, the stratum album profundum (SAP) lies just dorsally from the central grey (CG), and contains axons of output neurons located in the SGI and SGP as well as some intercollicular axons.

It must be noted that in many publications, the layers below SO are sometimes referred to as 'deep', although this is imprecise taken that below the SO, one finds at least two separate cellular layers (SGI and SGP). To avoid further confusions, this thesis will always refer to each layer by its Latin name. Another consideration to be made is on the comparison of the nonmammalian optic tectum and the mammalian superior colliculus. It has been proposed that the superficial SC (SZ, SGS, SO) in mammals is a correlate of the entire optic tectum in avians (Luksch, 2009). In avians, the SGI, SAI, SGP, and SAP of mammals are

rather subtectal and tegmental areas and not layers of the tectum at all. Thus, this thesis will always highlight when studies of avian species are presented, and comparisons with mammals in these cases will only be made about the superficial SC layers.

#### 1.4.1 VISUAL SC CIRCUITS

The major output neurons of the retina, the RGCs, project directly to the SC. Their axons enter the SC via the SO and terminate predominately in the SGS (Graybiel, 1975; Pollack & Hickey, 1979). Although most of the axons cross at the optic chiasm to terminate in the contralateral SC, there is however also an ipsilateral projection whose size depends on the extent of binocular visual field in a given animal. While rodents have mostly contralaterally-projecting RGCs in the SGS (Lund *et al.*, 1980; Cusick & Kaas, 1982; Major *et al.*, 2003), cats and primates have many more ipsilateral SC projections (Graybiel, 1975; Hubel *et al.*, 1975; Pollack & Hickey, 1979; Tigges & Tigges, 1981). Interestingly, birds with relatively large binocular visual fields have only contralaterally-projecting RGCs (Luksch, 2009).

The termination of RGC axons in the SC is organized topographically, where nasal-temporal retina projects along the rostral-caudal axis, and the dorsal-ventral retina projects along the medial-lateral SC axis. In this way, the central-peripheral world is represented rostro-caudally and the superior-inferior world is represented medio-laterally in the SGS. The development of cell-type specific transgenic animals together with *in vivo* imaging approaches allowed for thorough examination of the cell types in the SGS and their processing of visual information. In a study by Gale & Murphy (2014), five predominant types of neurons based on electrophysiological, morphological, target projection area, and visual stimuli responses were identified in the SGS (Fig. 1.5). Wide-field (WF)

neurons (1) have cell bodies in the SO and extend elaborately branched dendrites obliquely towards the SGS. They have relatively depolarized resting membrane potentials and largest and fastest depolarizing sags (Endo *et al.*, 2008). Their main axonal target is the lateral posterior nucleus of thalamus (LP) and they respond well to small moving stimuli in a large region of the visual field. Horizontal cells (2) have long horizontally-extending dendrites, high input resistances, and cannot sustain firing rates above 100 spikes/s. They are *gamma*-Aminobutyric acid (GABA) -ergic neurons whose axons project to the dorsal and ventral lateral geniculate nucleus (LGN) and the parabigeminal nucleus (PBg). They have large receptive fields and respond to large stationary objects or swiftly moving stimuli. Narrow-field (NF) cells (3) have thick dendrites extending ventrally into the SO and dorsally into the SGS and the SZ. They have very hyperpolarized resting membrane potentials and relatively low membrane resistances, and they mainly target the PBg and SGI layers of the SC. Predominantly, NF cells have small receptive fields, they prefer small stimuli and are often direction selective. Stellate cells (4) have small multipolar dendrites and after depolarizing current steps they respond with a large afterdepolarization. Stellate cells have small receptive fields, prefer small stimuli, and project to the PBg and the LGN. Gale and Murphy (2014) also characterized the so-called marginal cells (5) which populate mostly the SZ and extend their dendrites into the SGS. Although their electrophysiological properties matched those of stellate cells, the marginal cells were subsequently identified to be highly direction selective (Inayat *et al.*, 2015). Thus, clear neuronal types in the superficial SC might have distinct functions for processing visual stimuli.

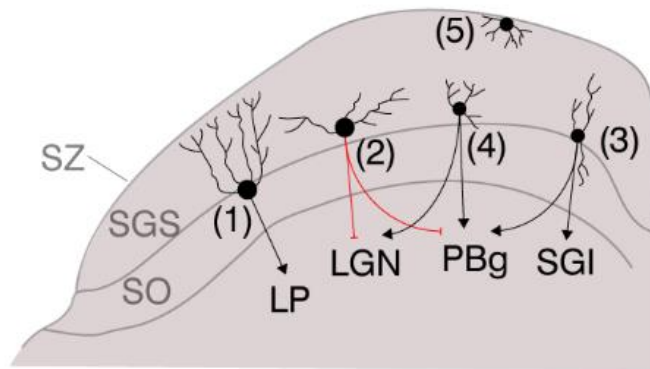


**Figure 1.5. The visual SC circuits - cell types and their projection targets**

WF neurons (1), horizontal neurons (2), NF neurons (3), stellate neurons (4), marginal cells (5). The black connections ended with arrows are excitatory connections and the red connections are inhibitory connections. SZ, stratum zonale; SGS, stratum griseum superficiale; SO, stratum opticum; LP, lateral posterior nucleus of the thalamus; LGN, lateral geniculate nucleus; PBg, parabigeminal nucleus; SGI, stratum griseum intermediale. The illustration is based on Gale & Murphy (2014).

Although as mentioned previously, comparisons with the nonmammalian tectum must be taken with caution, at least two neuron types seem to be conserved across species. In the chicken optic tectum, the horizontal cells, whose dendrites span 1000  $\mu\text{m}$ , get direct RGCs input and make connections with tectal output neurons (Luksch & Golz, 2003). They were also found to be GABAergic and immunopositive for calbindin. The projection neurons of layer 13 (the major output layer of the avian optic tectum) in the avians closely resemble those of WF mammalian neurons. Their large dendrites course obliquely towards the superficial layers, sampling 40° of visual angle in the retinotopic map and they respond to small fast-moving stimuli (Luksch *et al.*, 1998, 2001). The projection neurons of layer 13 also predominantly send axons to the homologue of the mammalian pulvinar (nucleus rotundus) through which they can, like WF neurons, influence visually guided behaviours. Interestingly, the projection neurons of layer 13 in the chicken were found to have bottlebrush dendritic

endings, the predominant site of RGCs axonal endings, hypothesized to be the basis for motion detection in these neurons. The very same dendritic endings were also found in the squirrel superior colliculus WF neurons (Major *et al.*, 2000), making this cell type in the tectopulvinar pathway conserved across different vertebrates.

In the rat, the physiological connectivity of the RGC axons in the SO with the SGS has been studied *in vitro*. Electrical stimulation of the incoming retinal axons in the SO induced monosynaptic excitatory postsynaptic potentials (EPSPs) in neurons of the SGS (Isa *et al.*, 1998) which resemble the neurons identified in Gale & Murphy (2014). Furthermore, electrical stimulation of the SO induced disynaptic EPSPs in the SGI, which were mediated by both  $\alpha$ -amino-3-hydroxy-5-methyl-4-isoxazolepropionic acid (AMPA) and NMDA receptors (Isa *et al.*, 1998).

Together, this data could provide basis for the role of specific superficial SC neurons in visually guided behaviour. For example, the NF cells could supply the intermediate SC with visual information via the excitatory SO-SGI connection. The WF cells could influence visually guided behaviour through their projection to the LP which is connected with higher-order cortical areas. The glutamate decarboxylase (GAD)2-Cre mouse line provides access to specific manipulations of the horizontal neurons in the SGS (Gale & Murphy, 2014). Because of their LGN projection, their influence in visually guided behaviour can be now tested with various novel molecular techniques. In summary, having detailed information about the SGS circuitry and its connectivity with other brain regions provides correlates for possible behaviours. These circuits can then be targeted *in vivo* to provide causal links to understand visually-guided behaviour mediated through the SC.

### 1.4.2 INTEGRATIVE SC CIRCUITS AND THE SC OUTPUT

Electrophysiological and morphological properties of cells populating the SGI have been thoroughly studied by joint efforts of the laboratories of Tadashi Isa & William C. Hall. Based on intrinsic electrophysiological properties, they characterized regular-spiking, burst-spiking, late-spiking, fast-spiking neurons, neurons with marked spike frequency adaptation, and neurons with rapid spike inactivation (only found in young animals) (Saito & Isa, 1999). Thus, five main firing patterns can be observed in the SGI neurons, and all of them exhibited linear input-output spiking upon injection of current via the recording pipette. Morphologically, neurons in the SGI were classified as multipolar, pyramidal-shaped, horizontal, fusiform, WF vertical cells (Ma *et al.*, 1990; Saito & Isa, 1999), and round-shaped neurons (Sooksawate *et al.*, 2011). Good correspondence of morphological and electrophysiological characteristics was only found for WF neurons which exhibited fast and large amplitude time dependent inward rectification caused by hyperpolarization activated current  $I_h$  (Endo *et al.*, 2008). As these WF neurons have their cell bodies in the upper part of the SG Ia, it has been suggested that the SG Ia and SO overlap to some extent (Endo *et al.*, 2008). In addition to WF neurons, retrograde tracer injection into medial pontine reticular formation (MPRF) identified the major types of SGI neurons to be regular-spiking with multipolar morphology (Sooksawate *et al.*, 2005). Furthermore, in a GABAergic knock-in mouse model, the most common firing pattern of GABAergic SGI neurons was fast spiking (~60%) and burst spiking (~30%) (Sooksawate *et al.*, 2011). Half of the GABAergic neurons in the SGI were morphologically multipolar, with some fusiform (22%), round-shaped (17%), and horizontal (10%). Thus, the GABAergic SGI fast and burst spiking neurons did not exhibit a distinct morphology in the SGI. In summary, the regular-spiking multipolar neurons in the SGI serve as the major SC output to motor-related

structures whereas the GABAergic SGI neurons are mostly fast-spiking. Currently the functions of the many other SGI cell types in sensory-to-motor transformation and multisensory processing are still undiscovered.

### *Interlaminar connections in the SC and non-linear amplification*

The best understood interlaminar pathway in the SC is the visuomotor SGS to SGI circuitry. Lee *et al.* (1997) found in the tree shrew that electrical stimulation of the SGS evoked the strongest excitatory synaptic currents (EPSCs) in the SGI when electrical stimulation was placed within a column dorsally from the SGI neuron recorded. Subsequently, electrical stimulation of the SO axonal bundle induced polysynaptic EPSPs in SGI neurons, which were mediated by both AMPA and NMDA glutamate receptors (Isa *et al.*, 1998). Using a glutamate uncaging method, Helms *et al.* (2004) showed a direct excitatory synaptic connection between the SGS and the SGI.

It has been suggested that the high-frequency burst activity in the SGI that precedes a saccade (termed the presaccadic burst) triggers the saccade generating motor circuits in the brainstem (Sparks, 1986). A mechanism for the presaccadic burst in the SC has been proposed *in vitro*, which may share one property, namely nonlinear amplification, with the presaccadic burst activity observed *in vivo*. *In vitro* experiments showed that SGI neurons produced a prolonged bursting response upon electrical stimulation of the SO when GABA<sub>A</sub> receptors were blocked (Özen *et al.*, 2000; Saito & Isa, 2003). The bursting response was not due to the intrinsic properties of the SGI neurons but rather due to the recurrent excitatory networks within the local circuits of the SGI, and the bursting was dependent on NMDA receptors (Pettit *et al.*, 1999; Saito & Isa, 2003). Corresponding data was also obtained by recording field potentials in the SGI upon SO stimulation using a microelectrode array (Phongphanphanee *et al.*, 2008). Altogether, the experiments suggest that a reduction of tonic inhibition on



SGI neurons allows for nonlinear amplification of columnar visual inputs to the SGI neurons evoking high-frequency bursting responses.

*Main motor targets of the SC and connections with the cerebellum and the basal ganglia*

The major output of the SC is a bundle of fibres running in the SAP layer (often termed the predorsal bundle) towards the brainstem and the spinal cord. Once the fibres cross to the contralateral side at the dorsal tegmental decussation, they are termed tectospinal and tectobulbar tracts. The collicular connections with motor-related brain regions are numerous and have been extensively reviewed (May, 2006). Depending on their target motor nucleus, their cell bodies are located in the SGI, SAI, and SGP layers of the SC.

Briefly, SC neurons send axons to all components of the brainstem saccade circuitry (Grantyn & Grantyn, 1982), namely the paramedian reticular formation of the pons (PPRF), the nucleus prepositus hypoglossi (nPH), and the central mesencephalic reticular formation (cMRF) for horizontal saccade components. For vertical saccade components the SC neurons project to the rostral interstitial nucleus of the medial longitudinal fasciculus (riMLF), the interstitial nucleus of Cajal (InC), the nucleus of the posterior commissure (nPC), and the nucleus raphe interpositus (RIP, for saccade halt during fixation). The rostral SC neurons also send axonal branches of the predorsal bundle directly to motoneurons located in the supraoculomotor area (Edwards & Henkel, 1978). However, the existence of this direct tecto-oculomotor pathway is still disputed (May, 2006).

The SC is also connected with many motor nuclei related to the movements of the head and the upper body. Multipolar neurons located in the SGI and SGP send axons in the tectospinal tract to the cervical enlargement in the cat, rat (Huerta & Harting, 1982; Murray & Coulter, 1982), and to the upper cervical levels in monkeys (May & Porter, 1992). In the contralateral spinal cord, they terminate on spinal interneurons within ventral spinal cord laminae

(Rexed's laminae V-IX). The second major head movement related SC projection is to the medullary reticular formation (MdRF). The SC tract of this projection runs parallel to that of the tectospinal neurons, suggesting that they might be functionally topographically aligned. Interestingly, it is yet unclear how the SC receives head movements information. This is because projections to the SC from the spinal cord are rather thought to provide somatosensory input for production of somatosensory map, and the MdRF is not known to project to the SC. Related to head movements, recent findings suggest that SGI neurons are tuned to specific head movements – namely pitch, roll, and yaw (Wilson *et al.*, 2018).

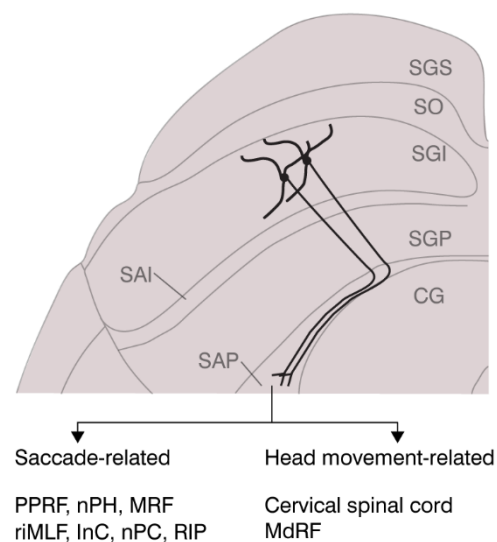


**Figure 1.6 Scheme of the main motor targets of the SC**

The axons of SC output neurons within the SAP (predorsal bundle) run towards many nuclei of saccade-related centres as well as head-movement related nuclei. SGS, stratum griseum superficiale; SO, stratum opticum; SGI, stratum griseum intermediale; SAI, stratum album intermediale; SGP, stratum griseum profundum; SAP, stratum album profundum; CG, central grey; PPRF, paramedian reticular formation of the pons; nPH, nucleus prepositus hypoglossi; MRF, mesencephalic reticular formation; riMLF, rostral interstitial nucleus of the medial longitudinal fasciculus; InC, the interstitial nucleus of Cajal; nPC, the nucleus of the posterior commissure; RIP, nucleus raphe interpositus; MdRF, medullary reticular formation.

There are also extensive SC connections with the cerebellum, mainly via projections to the precerebellar nuclei of the pons and the inferior olive, which provide the efferent copy of the collicular output. The cerebellum in turn also projects to the SC, mostly into the SGI. The connections of the cerebellum with the SC have been suggested to coordinate the activity between the colliculi but also to correlate the modality maps within the SC.

The basal ganglia influence over the SC is extensive and has also been relatively well studied (May, 2006). The connections originate in the substantia nigra [specifically from the ipsilateral substantia nigra pars reticulata (SNr)]. The main SC target of the SNr is the SGIb, with sparser terminations in the SGIa and the lateral portions of the SGP. Although the majority of nigrotectal projection is ipsilateral, there is also a less strong contralateral projection which terminates in roughly the same SC layers as the ipsilateral one. Its function is currently still debated however. The main targets of the nigrotectal projection are SC neurons projecting within the predorsal bundle. The SNr projection is exclusively GABAergic inhibitory and is topographically organized (Mana & Chevalier, 2001). An important observation is that SNr neurons are tonically active but pause firing before a saccade (Hikosaka & Wurtz, 1983). This observation is in line with the hypothesis of SGI neurons release from inhibition (basal ganglia disinhibition) after which a circuit mechanism in the SC causes nonlinear amplification of the signal, a burst of activity (presaccadic burst) and a motor response (saccade). Thus, the nigrotectal pathway represents a disinhibitory pathway with which the basal ganglia can influence SC activity.

One of the best understood SC circuit is the visuo-motor transformation for the production of saccades. Here, a position of an object on the retina is carried into a specific location of the superficial SC where the features of the object get scrutinized by the five neuron types. Most of the information is then transmitted to the pulvinar and the thalamus which carries it further to the cortex. In turn,

the cortex, through the influence of the SNr and its direct connections with the SC, releases a column in the SGI from inhibition. The very same column also receives a weak direct input from NF neurons located just dorsally in the SGS. The release from inhibition allows for a nonlinear amplification of the SGS input, causing a presaccadic burst in a column of the SGI, which in turn sends signals to the oculomotor circuitry in the brainstem to move the eyes towards the object the eyes fixated on. Although simplified here and still very hypothetical, the current literature points towards such mode of operation. Many open questions still remain. For example, we still do not know the exact cell type target of NF cells in the SGI. We also do not know the functions of the multiple neuron types found in the intermediate SC.

### 1.4.3 SOMATOSENSORY SC CIRCUITS

Major somatosensory projections to the SC originate in the spinal cord and the somatosensory cortex. Projections from the grey matter of the spinal cord at the cervical and lumbar levels were found to terminate somatotopically in the rostral and caudal SC, respectively (Edwards *et al.*, 1979; Wiberg *et al.*, 1987). Fine touch and proprioceptive information from the body is carried to the contralateral SC via both dorsal column nuclei (DCN) (Edwards *et al.*, 1979; Wiberg *et al.*, 1984, 1987; García Del Caño *et al.*, 2004), while specific subnuclei within the trigeminothalamic pathways deliver somatosensory facial inputs to the contralateral SC (Huerta *et al.*, 1981; Killackey & Erzurumlu, 1981; Harting & Van Lieshout, 1991). In the rat, the corticotectal pathway is formed by layer 5 cells in the barrel cortex (Wise & Jones, 1977; Killackey & Erzurumlu, 1981; Triplett *et al.*, 2012). The termination targets of the trigeminothalamic and corticotectal projections were found to overlap extensively in the mouse SG1a (Castro-Alamancos & Favero, 2016).

The cell type targets of the trigeminotectal and corticotectal projections are for now unknown, but some implications were provided from recent *in vitro* experiments (Castro-Alamancos & Favero, 2016). Here, optical activation of Channelrhodopsin-2 (ChR2) in trigeminotectal and corticotectal fibres evoked monosynaptic EPSPs in various types of neurons described in the SGI (including the WF neurons). Thus, the circuits underlying somatosensory SC integration are being unravelled only now.

#### 1.4.4 AUDITORY SC CIRCUITS

There are complex ascending and descending auditory projections to the SC. Early retrograde horseradish peroxidase (HRP) tracing studies in the cat, the rat, and the bat identified the IC, various nuclei of the superior olivary complex (SOC), and nuclei of the lateral lemniscus (LL) to project to the SC (Edwards *et al.*, 1979; Druga & Syka, 1984; Covey *et al.*, 1987). Subsequent anatomical studies in the ferret and guinea pig, using an alternative methodological approach (fluorescent microspheres or retrograde tracers instead of HRP), have identified the ipsilateral nBIC and the external nucleus of the IC (ECIC) as the main auditory inputs and only weak SOC and LL projections (Jiang *et al.*, 1997; Mellott *et al.*, 2018). In addition, the pattern of nBIC-SC innervation was shown to be organized topographically (King *et al.*, 1998), where rostral tracer injections into the SC labelled cells in the rostral part of the nBIC, while caudal SC injections produced labelling in the caudal nBIC portions. Such topographical arrangement was not found for the ECIC-SC projection (King *et al.*, 1998). A small population of inhibitory neurons originating in the nBIC projecting to the SC was also found, however their role in auditory projections to the SC was concluded to be small (Mellott *et al.*, 2018). Finally, the rostral pole of the IC (rpIC), a region not well defined in literature, has also been shown to project to the SC in the cat (Harting & Van Lieshout, 2000).

Initial reports of anterograde labelling on nBIC projections into the SC identified SAI as the main auditory-recipient layer in the SC (Nodal *et al.*, 2005), while later this was extended to the SGP and to the very ventral parts of the SGI (Doubell *et al.*, 2000; Skaliora *et al.*, 2004).

The physiological connectivity of the nBIC and ECIC with the SC been investigated in two studies. In one study, electrical stimulation of the SC below the SO evoked EPSPs in the nBIC neurons (Doubell *et al.*, 2000), however it is unclear whether the electrical stimulation activated axons of the nBIC neurons or the SC circuits projecting to the nBIC. In the second study, the recording was performed in the SGI and electrical stimulation was applied to the nBIC with a Teflon-coated bipolar silver wire (Skaliora *et al.*, 2004). With this configuration, the authors recorded EPSPs with a latency comparable to the previously mentioned study by Doubell *et al.* (2000). Thus, the physiological connectivity of either nBIC or ECIC with the SGP layer specifically (the main recipient layer of the auditory input in the SC) has been understudied. For example, the identity of SC-residing neurons that receive the nBIC/ECIC input is currently unknown. Similarly, the influence of the inhibitory nBIC/ECIC projection, although small, has not been studied physiologically.

#### *Auditory input circuitry of the nBIC*

The brachium of the IC was already described by Ramón y Cajal as a cover of the ECIC which in the cat contains descending corticotectal fibres and IC fibres passing towards the medial geniculate body (MGB) (Kudo & Niimi, 1980; Winer *et al.*, 1998). The nBIC is a cellular structure which is located more medially than the brachium and receives auditory inputs from the central IC (ICC). The nBIC (perhaps together with the ECIC) was suggested to be the mammalian counterpart of the external cortex in the barn owl (Winer & Schreiner, 2005). The external cortex in the barn owl contains a spatial map of sound location that is conveyed to the optic tectum (Knudsen & Knudsen, 1983). The nature of the

auditory signals sent by the nBIC to the SC in the mammal is unknown (Winer & Schreiner, 2005).

#### *Multimodal input circuitry of the ECIC*

Being part of the IC, the ECIC receives much of its auditory input from the ICC via the intracollicular connections (Aitkin & Phillips, 1984), and from the layer 5 of the auditory cortex (Winer *et al.*, 1998). Many tracing studies already pointed out to somatosensory projections to the ECIC which could provide an anatomical framework for audio-tactile integration. Projections from the DCN, the trigeminal nuclei, and the somatosensory cortex to the ECIC have been described in the cat (Aitkin *et al.*, 1981; Wiberg *et al.*, 1984), mouse (Lesicko *et al.*, 2016), and rat (Feldman & Kruger, 1980; Coleman & Clerici, 1987).

Although specific molecular markers do not exist in the ECIC that would separate this structure well from the neighbouring nBIC, the ICC, and the SC, three distinct layers have been identified in the rat (Faye-Lund & Osen, 1985). Out of those, the second layer contains clusters of many small neurons, distinguishing it from the fibrous first layer and layer three with large multipolar neurons. The clusters in the second layer have been subsequently identified as ECIC modules, which express specific molecular markers [GAD67, parvalbumin (PV) and other neurochemical markers] (Lesicko *et al.*, 2016) (Fig. 1.7). On the other hand, layers one and three, which are now called extramodular ECIC, specifically express calretinin (Dillingham *et al.*, 2017) (Fig. 1.7). In addition, it has been found that while somatosensory structures terminate within the ECIC modules, the projections of auditory structures always terminate within the extramodular ECIC (Lesicko *et al.*, 2016). Thus, such anatomical segregation of inputs calls for investigation into distinct functional roles that might accompany it. However, this hypothesis has not been tested so far. Furthermore, because the ECIC projects into the SC, it would be interesting to specifically study the

modular and extramodular ECIC projections into the SC (if they both exist) and their role in SC spatial coding and multisensory integration.

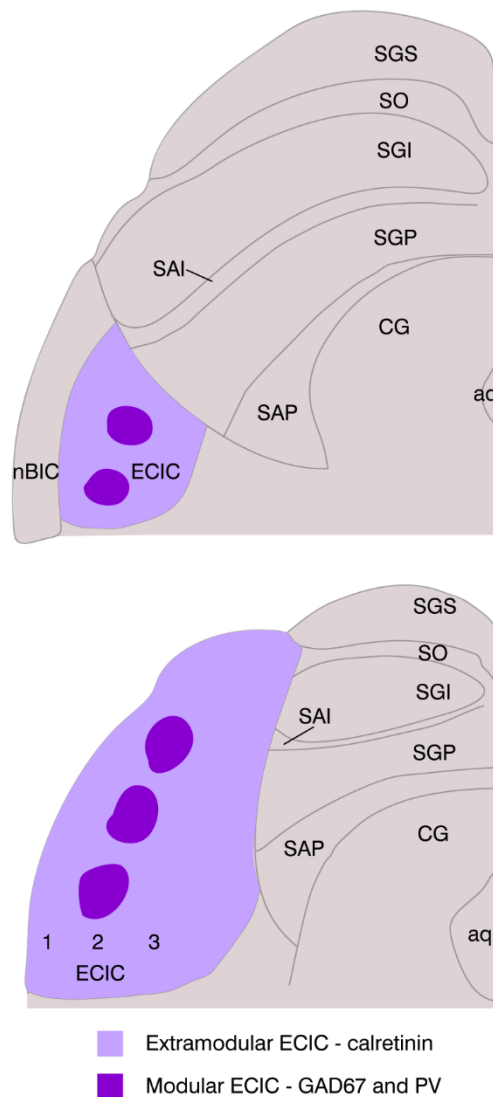


**Figure 1.7 Scheme of modular/extramodular ECIC**

In the rostral section (top), the anatomical locations of the ECIC in relation to the nBIC and the SGP is shown. In the caudal section (bottom), layers (1, 2, 3) are shown in the ECIC. SGS, stratum griseum superficiale; SO, stratum opticum; SGI, stratum griseum intermediale; SAI, stratum album intermediale; SGP, stratum griseum profundum; SAP, stratum album profundum; CG, central grey; aq, aqueduct; ECIC, external cortex of the inferior colliculus; nBIC, nucleus of the brachium of the inferior colliculus. The illustration is based on Lesicko *et al.* (2016) and Dillingham *et al.* (2017).



## **1.5 MOTIVATION TO STUDY THE SC AND THE OBJECTIVES OF PHD THESIS**

The SC is an important brain structure for coordinating orienting movements, but open questions about the cellular and circuit mechanisms underlying its function remain. Although the mechanisms of visual-to-motor transformation of SGS to SGI are being elucidated, it is unclear whether similar mechanisms also exist for the auditory and multisensory inputs integration in the SC. Moreover, it is not known how such sensory-motor transformation is performed for the auditory system. The lack of knowledge about the physiology of the auditory SC circuits hinders our understanding of multisensory integration as well as auditory spatial coding in the SC. For example, the identity of the SC-recipient auditory neurons is currently unknown. Similarly, the nature of the auditory signals carried into the SC from the nBIC/ECIC is also unexplored. In order to fully understand the SC function, the ultimate goal is to have a similarly-detailed picture for the auditory SC circuits, as we now have for the visual SC circuits. Therefore, the focus of this thesis was to characterize the auditory circuits in the mammalian SC.

First, the identity of neurons residing in the SGP was characterized in order to get insights into their spiking properties and morphology. For this purpose, the electrophysiological and morphological properties of SGP neurons were collected by whole-cell patch-clamp in brain slices obtained from wild-type (WT) mice (Results 3.1). Secondly, their synaptic connectivity with the nBIC and the ECIC was probed by utilization of optogenetic techniques (Results 3.2). An AAV-based method of vector delivery to infect neurons of nBIC and ECIC was used to delivered vectors expressing ChR2. ChR2 was then stimulated with laser in order to activate nBIC/ECIC axons and the postsynaptic currents in their synaptic SGP partners were recorded. Using this method, the connections between the nBIC/ECIC and the SC were characterized in the mouse, which were

then scrutinized further using ChR2-assisted circuit mapping to localize different pathways of nBIC and ECIC inputs. Finally, the molecular identity of the novel connections (namely the novel inhibitory connection) was tested for PV identity (Results 3.3).

---

# MATERIALS AND METHODS

---

## 2.1 ETHICAL APPROVAL

All experimental procedures were carried out in compliance with German animal welfare laws (Tierschutzgesetz), approved by the regional authority (Regierung von Oberbayern) under file number 55.2-1-54-2532.0-91-14 and conform to the principles and regulations as described in the Editorial by Grundy (2015). A total of 41 male and female mice were used in this study. Of those, 36 mice were of the C57BL/6 strain, 2 mice were of the CBA/Caj strain, and 3 were of the transgenic PVcre! line (in a C57 background). All mice originated from the mouse facility at the Max Planck Institute of Neurobiology. At all times the mice had access to fresh water and food ad libitum and were kept under 12/12 hour light/dark cycles.

## 2.2 STEREOTACTIC INJECTIONS

Mice aged postnatal day 24 (with date of birth P1) were anesthetized with an intraperitoneal injection of a mixture of fentanyl (0.05 mg/kg), midazolam (5 mg/kg), and medetomidine (0.5 mg/kg). Each mouse also received an oral dose of the analgesic metamizole (200 mg/kg), and a subcutaneous injection of carprofen (5 mg/kg) as an anti-inflammatory agent. Mice were fitted onto a stereotaxic frame of a Microinjection Robot (NeuroStar). The eyes were covered with Isopto-Max eye cream (Alcon Pharma) for its antiexudative effect to prevent corneal drying, and the skin of the skull was locally anaesthetized using 10% lidocaine. The animal's physiological body temperature was maintained using a heating pad warmed to 37 °C, which was designed and assembled by the in-

house electronics facility. The animal's skin was cut, and a small hole over the target brain area was drilled using a steel bur (Ref. No. 310 104 001 001 004, Hager & Meisinger GmbH) powered by Micro Motor Kit 1045 (Foredom). Viruses or tracers were then injected into the target area using a 10  $\mu$ l NanoFil syringe (WPI) at the rate of 0.05  $\mu$ l/min. Details on specific injection coordinates and substances injected are provided in Table 1. For retrograde tracing experiments, 0.2  $\mu$ l Fluoro-Gold [Hydroxystilbamidine bis(methanesulfonate), Sigma] was injected into the SGP layer of the SC. For electrophysiological experiments 0.1  $\mu$ l of AAV-based viruses [pAAV-hSyn-hChR<sub>2</sub>(H134R)-EYFP was a gift from Karl Deisseroth (Addgene plasmid No. 26973), University of Pennsylvania Vector Core] were injected into the nBIC/ECIC. The syringe was kept in place for 2 minutes after the injection to allow the substance to diffuse within the brain and was then slowly withdrawn. Finally, the skin of the skull was sutured using K802 Perma-hand Silk (Ethicon), and the animal was injected subcutaneously with an antidote mixture of naloxone (1.2 mg/kg), flumazenil (0.5 mg/kg), and atipamezole (2.5 mg/kg) to end the anaesthesia. After the surgery no antibiotics were administered, but on the first day after the surgery a subcutaneous injection of carprofen (5 mg/kg) for anti-inflammatory purposes was administered. The mouse recovery was observed for two consecutive days after the surgery and thereafter every third day until the day of the in vitro (two weeks post-surgery) or histological experiments (4 days post-surgery).

The human synapsin (hSyn) promotor used in this study has been shown to express in both excitatory and inhibitory neurons in the mouse cortex (Nathanson *et al.*, 2009) and under our experimental conditions the AAV2/1 transduction efficiency was 83% (2 out of 12 nBIC/ECIC neurons were negative for eYFP.ChR2), as determined by whole-cell recordings and somatic optical stimulation.

Table 1   Coordinates of stereotactic injections									
Substance	Mouse strain	Titre/ Concentration	Amount	AP	ML	DV	Target	Number of mice	
AAV2/1.hSyn.ChR2.eYFP.WPRE.hGH	C57BL/6	$5.86 \times 10^{16}$	0.1 $\mu$ l	-4.36	-1.6	2.46	nBIC/ECIC	19	
AAV2/1.hSyn.ChR2-eYFP.KV2.1.WPRE.hGH	C57BL/6	$8 \times 10^2$	0.1 $\mu$ l	-4.36	-1.6	2.46	nBIC/ECIC	4	
AAV2/1.CAGGS.Flex.ChR2. tdTomato.WPRE.SV40	B6.129P2-Pvalb <sup>tm1</sup> (cre)Arbr/J	$6.86 \times 10^2$	0.1 $\mu$ l	-4.36	-1.6	2.46	nBIC/ECIC	3	
Hydroxystilbamidine bis(methanesulfonate) (Fluoro-Gold™)	C57BL/6	5% in ddH <sub>2</sub> O	0.5 $\mu$ l	-4.1	-0.77	2.21	SGP	3	
Tetramethylrhodamine (TRITC)	CBA/Caj	5% in PBS	0.2 $\mu$ l	-4.16 (-3.97)	1.65 (-1.41)	2.64 (2.46)	ECIC (nBIC)	1	

Coordinates (in mm) are relative to bregma. AP, anteroposterior; ML, mediolateral; DV, dorsoventral.

### 2.3 ACUTE SUPERIOR COLLICULUS SLICES

The waiting times after the virus injection varied – for AAV.ChR2.eYFP and AAV.ChR2.Kv2.1.eYFP it was two weeks, while for the AAV.CAG.Flex.ChR2 it was three weeks. Thus, two to three weeks after the injection of the virus, mice (or uninjected WT mice aged P28-32) were anaesthetized with 1 ml isoflurane [2-chloro-2-(difluoromethoxy)-1,1,1-trifluoroethane], placed in a 2.4 l induction chamber and decapitated. The brain tissue was immediately placed into an ice-cold (~4 °C) dissecting solution containing the following (in mM): 73 sucrose, 83.8 NaCl, 24 NaHCO<sub>3</sub>, 1.25 NaH<sub>2</sub>PO<sub>4</sub>, 2.5 KCl, 25 D-glucose, 4 MgCl<sub>2</sub>, 0.5 CaCl<sub>2</sub> (pH 7.49 when bubbled with 95% O<sub>2</sub> and 5% CO<sub>2</sub>). Coronal SC slices (300 µm thick) were prepared using a VT 1200S vibratome (Leica). The collected slices originated from regions –4.72 to –4.16 mm relative to Bregma (Franklin & George, 2007). The slices were then incubated for ~20 min at 35 °C in an artificial cerebrospinal fluid (aCSF) containing the following (in mM): 128.3 NaCl, 2.5 KCl, 2 MgCl<sub>2</sub>, 1.25 NaH<sub>2</sub>PO<sub>4</sub>, 26 NaHCO<sub>3</sub>, 2 CaCl<sub>2</sub>, 10 D-glucose (pH 7.48 when bubbled with 95% O<sub>2</sub> and 5% CO<sub>2</sub>), after which they were transferred to the recording chamber.

### 2.4 ELECTROPHYSIOLOGY

All experiments were performed in perfused aCSF (flow rate: 1 ml/min and bubbled with 95% O<sub>2</sub> and 5% CO<sub>2</sub>). Recording temperature was measured near the slice and maintained at 30 °C by an SH-27B in-line heater (Warner Instruments) powered by a TC-324C heater controller (Warner Instruments). The tissue was visualized under an Eclipse FN1 upright microscope (Nikon) equipped with custom-built Dodt gradient contrast optics, a D-CUO DIC oil condenser (Nikon), and a Retiga EXi camera (QImaging). Whole-cell recordings

of SGP neurons [defined as <200  $\mu\text{m}$  dorsal from the CG] were obtained under visual control using a 60 $\times$ /0.90 N.A. water immersion objective (Olympus) with borosilicate glass electrodes using a MultiClamp 700B amplifier (Molecular Devices). Data were acquired at 10 kHz. Analysis was performed offline using Matlab (The Mathworks). Recording electrodes were filled with a K-gluconate based internal solution containing the following (in mM): 144 K-gluconate, 4 KCl, 10 HEPES [4-(2-hydroxyethyl)-1-piperazineethanesulfonic acid], 10  $\text{Na}_2$ -phosphocreatine, 4 Mg-ATP, 0.3  $\text{Na}_2$ -GTP, 0.05 Alexa Fluor 594 (Life Technologies), adjusted to pH 7.3 (at 30  $^\circ\text{C}$ ) and 296 mOsm. Electrodes had 3.8–4.2  $\text{M}\Omega$  tip resistances. Recordings were accepted only if the uncompensated series resistance was <20  $\text{M}\Omega$  and stable over the course of the recording (<20% change).

## 2.5 CURRENT-CLAMP EXPERIMENTS

For intrinsic electrophysiological property measurements, hyperpolarizing and depolarizing current steps of 250 ms duration were delivered through the recording electrode to the neurons, and their membrane responses were recorded in the current-clamp configuration. Depending on the input resistance of the neuron, the hyperpolarizing steps ranged from –100 to 0 pA (10 pA/step) or from –50 to 0 pA (5 pA/step). The depolarizing steps ranged from 0 to 700 pA (50 pA/step). To induce single action potentials (APs), short depolarizing current steps with 10 ms duration and with range of 25 to 250 pA (25 pA/step) were delivered, and the APs from these recordings were used to construct phase-plane plots.

## 2.6 LASER STIMULATION SETUP

ChR2-expressing presynaptic neurons were optically stimulated with 473 nm light from an S3FC473 solid-state laser (ThorLabs) coupled to an RB42F1 optic fibre and an F230FC-A collimator (ThorLabs). The laser pulses were directed via an OPX2250 galvanometer-based scanhead (ThorLabs) to the back aperture of a 4×/0.13 N.A. air objective (Nikon) focused on the brain slice. The laser spot size was ~300 μm (full width at half maximum). This beam was intentionally designed to have a pencil shape, providing better uniform illumination through the slice, but at the expense of diameter, which is larger than what an overfilled 0.13 N.A. objective would produce. The intensity of the light pulses was modulated directly via the 473 nm laser controller and additionally gated with a VS-14 shutter (Uniblitz). Data acquisition was controlled using open source software Ephus (Suter *et al.*, 2010) running on Matlab (The Mathworks).

## 2.7 VOLTAGE-CLAMP/PHOTOSTIMULATION EXPERIMENTS

For ChR2-assisted circuit mapping experiments (Petreanu *et al.*, 2007), laser pulses (2 ms duration, 1 s inter-stimulus interval) were delivered on an 8 × 8 stimulation grid with 175 μm spacing. This stimulation grid area (1.2 × 1.2 mm<sup>2</sup>) was sufficient to cover both the nBIC and the ECIC. Due to the relatively large laser spot size, activation sometime bled into a neighbouring position, but seldom any further. The closest laser stimulation point was >400 μm away from the SGP neuron recorded and the recordings were always performed in the SC hemisphere ipsilateral to the injection site. Neurons were voltage-clamped at -70 and 0 mV to measure excitatory postsynaptic currents (EPSCs) and inhibitory postsynaptic currents (IPSCs), respectively. The EPSCs and IPSCs recorded by stimulation of a particular stimulation grid position were used to construct



excitatory and inhibitory synaptic input maps. Each recording was repeated 3–5 times under control conditions, after which 5  $\mu\text{M}$  (R)-CPP [(R)-4-(3-phosphonopropyl)piperazine-2-carboxylic acid] and 10  $\mu\text{M}$  NBQX [2,3-Dihydroxy-6-nitro-7-sulfamoyl-benzo(f)chinoxalin-2,3-dion] were perfused through the chamber to block NMDA and AMPA receptors, respectively. After 2 minutes of drug perfusion (from the moment the aCSF with the drugs entered the recording chamber), the inhibitory (repeated 3–5 times) and excitatory (repeated once) recordings were acquired again. To block GABA<sub>A</sub> receptors, 20  $\mu\text{M}$  picrotoxin (Tocris) was perfused through the slice. This perfusion protocol was empirically tested in our laboratory to completely block each receptor of interest in this study. The laser intensity (0.06–0.88 mW) was kept constant throughout the experiment. Data from these experiments were used for distribution analyses, IPSC peak analysis (to distinguish polysynaptic from monosynaptic inputs), latency analysis, and the strength of direct inhibition on cell clusters ( $n = 10$  SGP neurons). For experiments where recordings from nBIC and ECIC neurons were performed, voltage-clamp and current-clamp recordings were obtained upon repeated laser stimulation at a single spot over the neuron body with varying laser intensities. The threshold laser power was measured as the laser power that induced a single AP in 80% of all trial repetitions (in current-clamp recording).

## 2.8 SYNAPTIC CURRENT ANALYSIS

For each stimulus position, the EPSC/IPSC strength was calculated as the peak response current of the averaged traces in a time window of 1–21 ms after the stimulus onset. EPSCs and IPSCs were considered non-zero if their amplitudes were larger than 7 times the SD of a 20 ms baseline directly before stimulus onset. Since we do not know the number of nBIC/ECIC projections of a

given SGP neuron and how many of those were infected by the AAVs, it is challenging to compare their strengths onto the same SGP neuron (Petreanu *et al.*, 2009). Thus, the synaptic input maps were normalized. To compare amplitude differences due to blocking of NMDA and AMPA receptors, the maps obtained from recordings during blockade of excitatory transmission were normalized to the maximal value of their respective control input maps (drugs inhibition normalized to control inhibition, drugs excitation normalized to control excitation).

## **2.9 ANALYSES OF DIRECT EXCITATION AND INHIBITION DISTRIBUTION DIFFERENCES**

For the purposes of these analyses, only traces from excitatory input maps in the control condition and the inhibitory input maps in the drugs condition for ten SGP neurons were taken. The reason for only analysing these traces is that they represent the respective direct excitation and inhibition (and not mixed inhibition). To appreciate differences in the locations of the excitation and inhibition in nBIC/ECIC, Kruskal–Wallis tests were performed on the excitatory and inhibitory responses for each stimulation grid position and the resulting *p*-values were plotted as a heat map. For mediolateral and dorsoventral input distribution profiles, the synaptic input maps were collapsed by taking the maximal response along the mediolateral or dorsoventral dimension and then averaged across 10 SGP neurons. Half-maximal response positions were interpolated from cumulative distributions of these profiles (data presented as mean  $\pm$  SEM), and the nonparametric Kruskal–Wallis test was used to check for statistical significance between the distributions of the half-maximal positions. For latency analysis, only the grid stimulus positions within the nBIC/ECIC which evoked EPSCs and IPSCs were considered, and from those a mean direct

inhibitory and excitatory latency for a single cell was calculated and then averaged across 5 SGP neurons which fit that criteria. Latency data are presented as mean  $\pm$  SEM in the results section.

## **2.10 DISTINGUISHING POLYSYNAPTIC AND MONOSYNAPTIC INHIBITORY INPUTS**

In some preparations, no currents could be measured when stimulating the nBIC/ECIC, likely due to somas severed from their axons during the slicing process or slightly different cutting angles. In these cases, the grid (either an 8  $\times$  8 grid, 175  $\mu$ m spacing or a 4  $\times$  4 grid, 200  $\mu$ m spacing) was moved dorsomedially to map the axons of the nBIC/ECIC neurons running into the SGP. Thus, in these recordings, the closest stimulation point in some cases was less than 100  $\mu$ m from the recorded SGP neuron ( $n = 15$  SGP neurons). Data from these experiments was added to the 10 SGP neurons and together were used for IPSC peak analysis and for calculating the strength of direct inhibition on cell type clusters (in total 25 SGP neurons). To distinguish polysynaptic from monosynaptic IPSCs, the peaks of the three individual recording traces were compared between control and drug wash-in conditions using Kruskal–Wallis tests, and this was performed for every nonzero grid position for all recordings regardless of grid location. If a single position within the grid map showed a significant decrease ( $p < 0.05$ ) in IPSC peak value after drugs wash-in, the SGP neuron was considered to have a polysynaptic inhibitory component. Otherwise, the SGP neuron was considered to have predominantly monosynaptic inhibitory connections.

## 2.11 ANALYSIS OF INTRINSIC ELECTROPHYSIOLOGICAL PROPERTIES

Five electrophysiological parameters were calculated from membrane responses to the hyperpolarizing and depolarizing current steps. Hyperpolarizing steps producing a small hyperpolarization (−10 to −5 mV) from the resting membrane potential were used to determine the input resistance ( $R_m$ ). Maximum firing frequency was calculated in Hz from the 700 pA depolarizing current step. Some neurons exhibited a ‘late-spiking’ property, which was calculated as the ratio of the inter-spike interval (ISI) between the first and second AP ( $ISI_1$ ) to the ISI between the second and the third AP ( $ISI_2$ ). The time (in ms) from the current step onset to the first AP (Time to spike) and AP width at half-amplitude (Spike half-width) were measured at the AP threshold depolarizing current step. Data are presented as mean  $\pm$  SD. For cluster analysis, Euclidean distance and shortest distance linkage criteria for hierarchical clustering were used. Here, each data parameter was normalized between 0 (population minimum) and 1 (population maximum). An alternative clustering algorithm, *k*-means, was also performed to compare with the hierarchical clustering results. With three predefined number of clusters, the clusters were well separated (silhouette value  $> 0.5$  included 21/23 neurons), while with four predefined number of clusters, one neuron had a negative silhouette value (silhouette value  $> 0.5$  included 17/23 neurons). This indicates poor cluster separation when more than three clusters were tested, corroborating the linkage-distance criterion. From the 25 SGP neurons recorded with presynaptic ChR2 stimulation, intrinsic electrophysiological characterization was obtained for 23. These neurons were separately classified into the three clusters using the same clustering method as described above.

## **2.12 ANALYSIS OF THE STRENGTH OF DIRECT INHIBITION ON SGP CELL CLUSTERS**

For the analysis of the strength of direct inhibition on SGP cell clusters, 19 SGP neurons and their corresponding inhibitory input maps in the NMDA/AMPA blocked condition were analysed. Here, the IPSC amplitudes either cell type-wise or stimulation position-wise were analysed. In the cell type-wise analysis, the mean IPSC value of an inhibitory input map of each cell was calculated. The mean values were then separated into three clusters, according to the cell type cluster to which the cells were allocated to by hierarchical clustering. In the stimulation position-wise analysis, all IPSC amplitudes evoked by multiple stimulation positions for each cell were calculated, and these were then segregated according to the cluster to which the cells were allocated to by hierarchical clustering. To test for statistical differences between cell clusters on either the cell type-wise or stimulation position-wise IPSC amplitudes two-sample Kolmogorov–Smirnov test was used.

## **2.13 ANALYSIS OF SOMATODENDRITIC MORPHOLOGY**

After the recordings (10 min minimum time of dye diffusion), dendritic arbours of 20 SGP neurons filled with Alexa Fluor 594 (50  $\mu$ M in the recording pipette) were imaged using an Acera resonant-galvanometer 2-photon scanhead (Thorlabs) driven by a Mai Tai eHPDS ti:sapphire laser (Spectra-Physics). The Alexa Fluor 594 was excited by two-photon laser at 810 nm wavelength. Tracing was performed on z-stacks (30 frames averaged, 1  $\mu$ m step size) and the 3-dimensions of the dendrites were measured. To calculate the arbour orientation index (AOI) (Gale & Murphy, 2014), the vertical axis of the neuron was determined as the angle of the vector producing the shortest distance from the neuron soma to the dorsal surface of the SC. Two lines intersecting at the soma

with a  $\pm 45^\circ$  angle from the vertical axis were then drawn, dividing the dendritic arbour into four quadrants: dorsal, ventral, lateral, and medial. Sholl analysis (Sholl, 1953) was then used to measure the number and locations of dendrite intersections with circles of increasing radii ( $25 \mu\text{m}/\text{circle}$ ) from the centre of the soma. The AOI was then calculated according to Equation 1,

$$\text{AOI} = \frac{\text{Sholl V} - \text{Sholl H}}{\text{Sholl V} + \text{Sholl H}} \quad (1)$$

where the number of Sholl points in the dorsal and ventral quadrant were added together to make the number of points in the vertical axis (Sholl V), and the lateral and medial were added to make the horizontal axis (Sholl H). Indices near 1 indicate a dorsoventral orientation along the vertical axis, and indices close to 0 indicate branches oriented equally in all directions. AOI data are presented as mean  $\pm$  SD. The same Sholl analysis was used to determine the number of primary dendrite branches from the soma and the data are presented as mean  $\pm$  SD.

## 2.14 IMMUNOHISTOCHEMISTRY

To trace the inputs of the SGP layer of the mouse SC, retrograde tracing experiments were performed. Three mice received a monolateral injection of the retrograde tracer Fluoro-Gold into their SGP layer of the SC. To trace the projections of the nBIC/ECIC to the SC, bidirectional tracing experiments were performed. One mouse received a bilateral injection of the bidirectional tracer Tetramethylrhodamine (TRITC) into the SGP layer of the SC. Details on specific injection coordinates is provided in Table 1. Four days after Fluoro-Gold injection (five days for TRITC), the mice were anaesthetized and decapitated using the same isoflurane anaesthesia procedure for acute electrophysiology experiments. The dissected brain was placed into paraformaldehyde (PFA 4% in phosphate-

buffered saline (PBS)) for 3 hours at room temperature and then overnight at 4 °C. Before slicing, the brain was washed 3 times in 0.02 M PBS and embedded in 4% agar (in H<sub>2</sub>O). Then, coronal brain sections of 50 µm were collected on a VT 1200S vibratome. After rinsing in 0.02 M PBS, the sections were placed into a blocking solution containing 1% bovine serum albumin, 0.5% Triton X-100, and 0.1% saponin in PBS. The slices were incubated overnight at 4 °C with primary antibodies and for 3 hours at RT with secondary antibodies. Antibody specifications are listed in Table 2. Slices from all three brains were used for GAD67, calretinin, and PV staining. For calbindin and somatostatin staining, slices from two brains were used, and one of the mice was used for choline acetyltransferase (ChAT) staining. After antibody incubation, sections were rinsed 3 times for 10 min in 0.02 M PBS and cover slipped with Vectashield mounting medium (Vector Laboratories).

Table 2 | List of main reagents used for immunochemistry

	Host	Working dilution	Source	Catalog number
<b>Primary antibodies</b>				
anti-GAD67	mouse	1:200	Abcam	Ab26116
anti-Parvalbumin	rabbit	1:500	SWANT	SV28
anti-Calretinin	rabbit	1:500	SWANT	7699/3H
anti-Somatostatin	rat	1:100	Millipore	MAB354
anti-Calbindin	rabbit	1:500	SWANT	CB38a
anti-ChAT	goat	1:500	Millipore	AB144P
<b>Secondary antibodies</b>				
	Conjugated to			
anti-mouse	Alexa488	1:200	DIANOVA	715-545-150
anti-rabbit	Alexa488	1:300	DIANOVA	711-545-152
anti-rabbit	CY3	1:400	DIANOVA	711-165-152
anti-rat	CY3	1:200	DIANOVA	712-165-153
anti-goat	CY3	1:300	DIANOVA	705-165-147
anti-rabbit	Alexa647	1:300	DIANOVA	711-606-152
Deep-Red Nissl stain	-	1:100	Invitrogen	N21483
Green Nissl stain	-	1:100	Invitrogen	N21480

## 2.15 CONFOCAL MICROSCOPY

Confocal optical images were acquired with a TCS SP8 confocal microscope (Leica) equipped with HC PL APO CS2 20×/0.75 N.A. glycerol immersion objective. Fluorochromes were visualized with excitation wavelengths of 405 nm for Fluoro-Gold (emission: 530–600 nm), 488 nm for Alexa Fluor 488 (emission: 496–554 nm), 496 nm for Green Nissl stain (emission: 510–556 nm), 514 nm for CY3 and eYFP (emission: 520–550 nm), 561 nm for TRITC and tdTomato (emission: 566–650 nm), and 633 nm for Nissl Deep-Red and Alexa Fluor 647 (emission: 639–734 nm). Images were acquired as tiles of 738.1 × 738.1 μm (0.72 μm/pixel) and automatically stitched by LAS X software (Leica). All images were Kalman-averaged from two to four successive scans.

## 2.16 ANALYSIS OF CONFOCAL IMAGES AND CELL COUNTING

Retrogradely-labelled neurons were counted in two separate images, one corresponding to the nBIC and the other to the ECIC. Because Fluoro-Gold fluoresced as puncta in the cytoplasm, the retrogradely-labelled neurons were distinguished from tissue debris by Nissl counterstaining. The percentages were then calculated according to Equation 2,

$$\% \text{ Retro marker} = \frac{\text{Retro marker}}{\text{Retro only} - \text{Retro marker}} \cdot 100 \quad (2)$$

where the number of counted neurons was labelled as ‘Retro only’ and the number of those neurons positive for GAD67 or calretinin was labelled as ‘Retro GAD67’ and ‘Retro calretinin’, respectively, and the marker was GAD67 or calretinin.



---

## RESULTS

---

### 3.1 ELECTROPHYSIOLOGICAL AND MORPHOLOGICAL CHARACTERIZATION OF CELL TYPES IN THE SGP LAYER OF THE MOUSE SC

#### 3.1.1 THREE ELECTROPHYSIOLOGICALLY-DEFINED CELL TYPES POPULATE THE SGP OF THE MOUSE SC

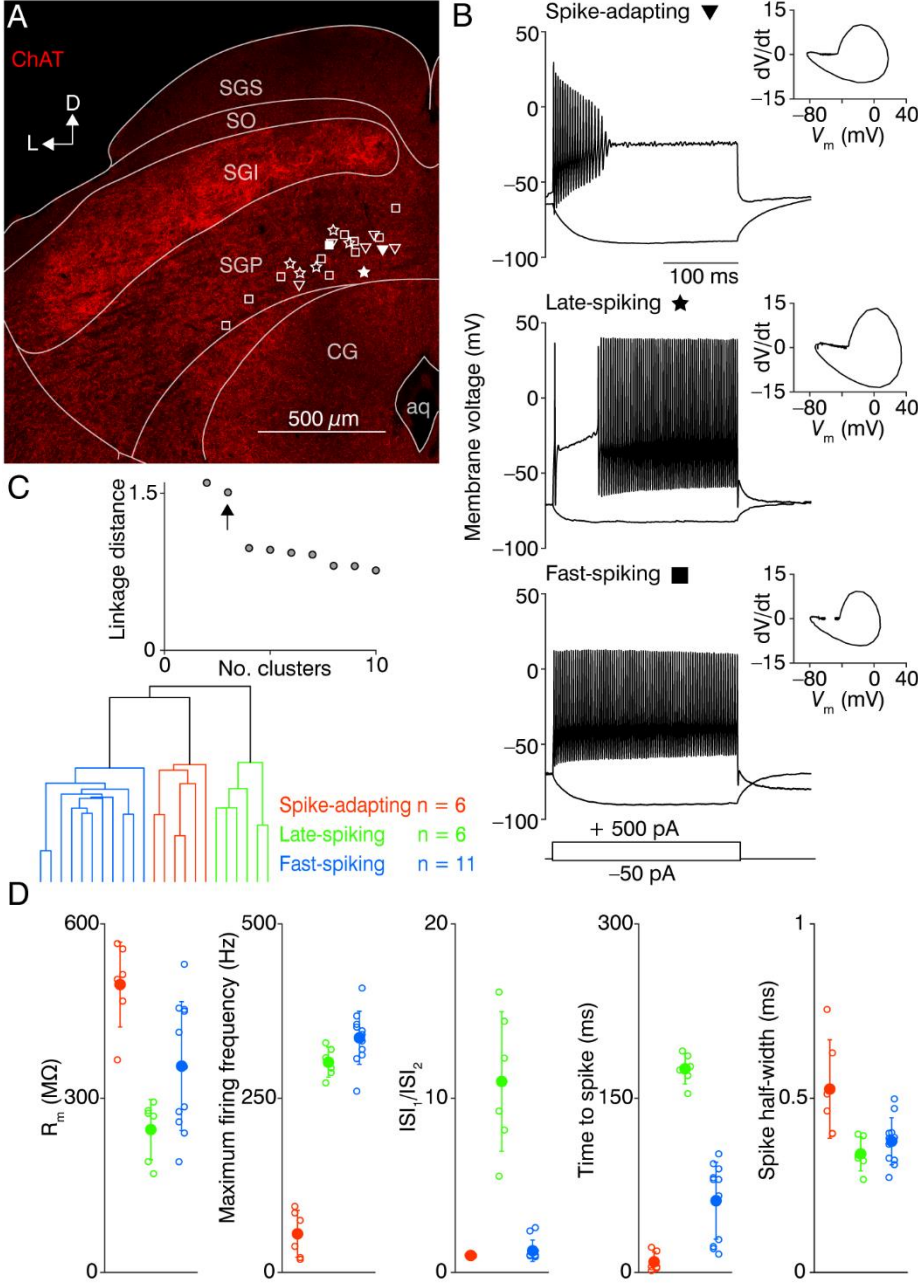
Wild-type C57BL/6 mice (N = 10) were used to obtain whole-cell current-clamp recordings of 23 SGP neurons. The SGP layer is readily distinguishable from the intermediate layers by markedly lower expression of ChAT (Fig. 3.1A) (Chevalier & Mana, 2000), from which the SGP layer spread up to 200  $\mu\text{m}$  dorsally from the CG. Thus, the whole-cell recordings were performed exclusively within this region. Neuronal intrinsic electrophysiological properties were obtained by recording the membrane responses to hyperpolarizing and depolarizing current steps (see Methods). Visual inspection of raw traces from these recordings already pointed to at least three distinct electrophysiological types of neurons: spike-adapting (Fig. 3.1B, top), late-spiking (Fig. 3.1B, middle), and fast-spiking (Fig. 3.1B, bottom). To gain further quantitative insight into the electrophysiological diversity of the SGP neurons, I performed hierarchical clustering on the following five parameters: the input resistance, the maximum firing rate (at 700 pA current injections), the ratio of the first to second inter-spike intervals ( $\text{ISI}_1/\text{ISI}_2$ ), the time from the current step onset to the first AP (measured at the AP current threshold), and the Spike half-widths. The separation between the first three clusters was large (linkage distance: 1.51) relative to the separation between additional clusters (linkage distance 0.98 for four clusters, Fig. 3.1C, top), providing quantitative evidence for at least three distinct SGP neuron types. The cluster separation is visually apparent when plotting each parameter cluster-wise (Fig. 3.1D). Spike-adapting neurons (n = 6) had relatively high input resistances ( $495.7 \pm 73.1 \text{ M}\Omega$ ), could not sustain high firing rates ( $55.3 \pm 33.6 \text{ Hz}$ ), and

exhibited relatively broad Spike half-widths ( $0.53 \pm 0.14$  ms). Late-spiking neurons ( $n = 6$ ) had relatively low input resistances ( $245.9 \pm 51.9$  M $\Omega$ ), large  $ISI_1/ISI_2$  ratios ( $11.0 \pm 4.0$ ), and long latencies to their first AP ( $175.3 \pm 13.1$  ms). Fast-spiking neurons ( $n = 11$ ) were able to spike at very high frequencies ( $336.6 \pm 38.1$  Hz), exhibited relatively regular ISIs ( $ISI_1/ISI_2$  ratio  $1.2 \pm 0.61$ ), and had intermediate input resistances ( $355.2 \pm 111.0$  M $\Omega$ ). There was no spatial organization of any cluster type within the area of the SGP, from which the recordings were obtained (Fig. 3.1A).

---

### Figure 3.1 Identification of three SGP neuron types on the basis of their electrophysiological properties

**A**, Confocal image of a brain slice stained for ChAT showing the major divisions of the SC. The locations of all recorded SGP neurons are displayed by open symbols, where triangles correspond to the spike-adapting neurons, stars to the late-spiking neurons, and squares to the fast-spiking neurons. The filled symbols are the locations of the representative three SGP neurons shown in (B). SGS, stratum griseum superficiale; SO, stratum opticum; SGI, stratum griseum intermediale; SGP, stratum griseum profundum; aq, aqueduct; CG, central grey; L, lateral; D, dorsal. **B**, Example traces for representative SGP neurons in response to a 250 ms depolarizing (+500 pA) and a hyperpolarizing (-50 pA) current step. Insets show phase-plane plots of the first fired AP. **C**, Linkage distance of the hierarchical clustering as a function of the increasing cluster number (top). Arrow indicates the linkage distance for three clusters. Dendrogram plot of hierarchical binary cluster tree (bottom). Colour code in (C) applies to (D). **D**, Cluster-wise plots of the following intrinsic parameters (from left to right): input resistance ( $R_m$ ), maximum firing frequency at the current step of +700 pA, ratio of the first to second inter-spike intervals in a train of APs ( $ISI_1/ISI_2$ ), time to first spike from the current onset at threshold traces, the half-width of the first fired AP. Empty circles represent individual neurons and filled circles represent the cluster mean  $\pm$  SD. SGS, stratum griseum superficiale; SO, stratum opticum; SGI, stratum griseum intermediale; SGP, stratum griseum profundum; CG, central grey; aq, aqueduct. Modified from Bednárová *et al.* (2018).



### 3.1.2 SGP CELL TYPES EXHIBIT DISTINCT ORIENTATION OF DENDRITES

Next, I investigated whether the three neuron clusters also exhibited distinct morphology. To this end, I obtained 2-photon z-stacks of a subset of recorded neurons (20/23, filled with Alexa Fluor 594 via the patch pipette). Dendritic size was  $235 \pm 81 \mu\text{m}$  (mean  $\pm$  SD),  $300 \pm 47 \mu\text{m}$ , and  $67 \pm 23 \mu\text{m}$  in the *x*, *y*, and *z* dimensions, respectively. As the dendritic arbours of all imaged neurons were rather planar and parallel to the coronal slices (20–28% *z*-axis deviation in either the *x* or *y* dimension), further analysis was performed on the *z*-projected micrographs. The fact that the surface of the SC is curved (along with the individual SC layers) was considered and thus I defined the vertical axis for each traced neuron as the angle of the shortest vector that can be drawn between the soma and dorsal surface of the SC, as has been done previously for the superficial SC (Gale & Murphy, 2014). After vertical alignment, the dendritic arbours were segmented into four quadrants representing the dorsoventral and the mediolateral axes. By performing Sholl analysis on each quadrant, an arbour orientation index (AOI) for each traced neuron was calculated, which describes the extent to which dendritic arbours are vertically oriented (Gale & Murphy (2014), see Materials and Methods). Example neurons from each cluster already suggested distinct morphology between the clusters (Fig. 3.2A), where spike-adapting neurons tended to have a vertical orientation, while the late-spiking neurons had typically two dendrites oriented towards the SC surface. In contrast, fast-spiking neurons seemed to have branches in both vertical and horizontal directions in a cross-like manner. Plotting the calculated AOIs for all neurons (Fig. 3.2B) indeed revealed a higher average value for spike-adapting neurons ( $0.78 \pm 0.28$ ,  $n = 6$ ), compared to late-spikers ( $0.44 \pm 0.20$ ,  $n = 6$ ) and fast-spikers ( $0.38 \pm 0.26$ ,  $n = 8$ ). The difference between spike-adapting neurons and fast-spikers was also statistically significant ( $p = 0.02$ , Kruskal–Wallis test). Adding the AOIs into the hierarchical clustering analysis as a sixth parameter did not change the

resulting neuron allocation to a specific cluster, but shortened the distance between the late- and fast-spiker clusters (also reflected by the non-significant result for the AOI between late- and fast-spikers,  $p = 0.37$ , Kruskal–Wallis test). In addition to analysing AOIs, I also counted the number of primary dendritic branches for each cluster (spike-adapting  $3.33 \pm 1.03$ ,  $n = 6$ , late-spiking  $3.67 \pm 0.82$ ,  $n = 6$ , fast-spiking  $4.00 \pm 0.76$ ,  $n = 8$ , Fig. 3.2C). In contrast to the AOIs, all clusters had a number of main dendrites statistically indistinguishable from one another (adapting- vs late-spiking  $p = 0.72$ , late- vs fast-spiking  $p = 0.41$ , adapting- vs fast-spiking  $p = 0.23$ , Kruskal–Wallis test). Thus, the SGP of the mouse SC is largely populated by three electrophysiologically distinguishable neuronal types that tend to have a characteristic dendritic orientation.

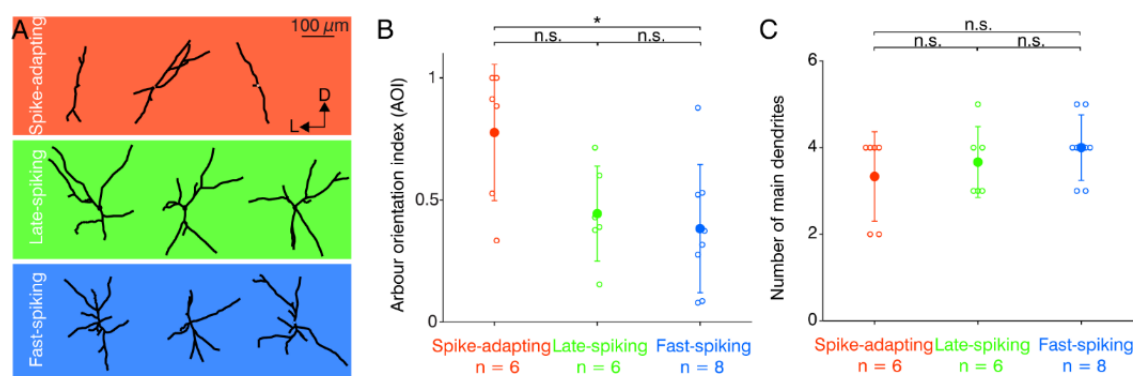


**Figure 3.2 Identification of three SGP neuron types on the basis of their morphological properties**

**A**, Traced dendrites of three example neurons for each electrophysiologically defined cluster. Orientation axes (L, lateral; D, dorsal) are relative to the dorsal SC surface. **B**, AOI of the defined clusters. Empty circles represent individual neurons and filled circles represent the cluster mean  $\pm$  SD. \*,  $p < 0.05$ ; n.s., not significant (Kruskal–Wallis test). **C**, Number of main dendrites of the defined clusters. Empty circles represent individual neurons and filled circles represent the cluster mean  $\pm$  SD. n.s., not significant (Kruskal–Wallis test). Modified from Bednárová *et al.* (2018).

### 3.1.3 CONCLUSION

In the first part of the results I presented data on electrophysiological and morphological characterization of cell types residing in an intricate SGP layer of the mouse SC. The results of hierarchical clustering show at least three types of neurons. The characteristics of spike-adapting neurons were large input resistances and vertically-oriented dendrites. The fast-spiking neurons could spike at high frequencies and extended their dendrites in all orientations equally. The late-spiking neurons had low input resistances with dendrites oriented dorso-ventrally to some extent.

## 3.2 ANATOMICAL AND FUNCTIONAL CONNECTIVITY OF THE nBIC/ECIC AND THE SGP OF THE MOUSE SC

### 3.2.1 ANATOMICAL PROJECTION OF THE nBIC/ECIC TO THE SGP IN THE MOUSE CONFIRMED BY TRACER INJECTION

The auditory projections from the nBIC and the ECIC to the SC have been anatomically studied in a number of animal species (Edwards *et al.*, 1979; Druga & Syka, 1984; Covey *et al.*, 1987; Jiang *et al.*, 1997; King *et al.*, 1998; Mellott *et al.*, 2018)(Edwards & Stein, 1979; Druga and Syka, 1984; Covey and Kobler, 1987; Jiang & King, 1997; King & Moore, 1998; Mellott & Schofield, 2018). Because the mouse was the model organism used in this study, a confirmation of the anatomical existence of the nBIC/ECIC - SGP projection under our experimental conditions was performed. Therefore, I injected TRITC bilaterally into the nBIC/ECIC and then visualized the tracer in fixed brain slices (N = 1 mouse, CBA/Caj strain). The rostrocaudal extent of the injection into one hemisphere is shown in Figure 3.3. In a slightly more caudal section (Fig. 3.3B), the emerging nBIC appears as the shoulder of the ECIC. The bulk of the injection is visible in the nBIC at the level of the SC (Fig. 3.3C), where axonal projections from the nBIC towards the SC are clearly visible. The tracer also spread into the medially located ECIC from which axonal projections into the SC could also be followed. The axonal projections of both the nBIC and ECIC could be followed as they course toward the SC. It is interesting to compare patterns of axonal projections between slices to gain insight into their trajectories in the slicing plane. For example, at the border of the ECIC with the SC, the axons seem to disappear, while more medially towards the SC they emerge again and enter the SC (Fig. 3.3B). In the rostral sections (Fig. 3.3D–F), cell bodies in the nBIC/ECIC were gradually less labelled, while the axonal projections into the SC were still clearly visible although they became sparser. Thus, a distinct anatomical projection from both



nBIC and the ECIC exists in the mouse SC and the nBIC and ECIC axons do not run parallel to the slicing plane.

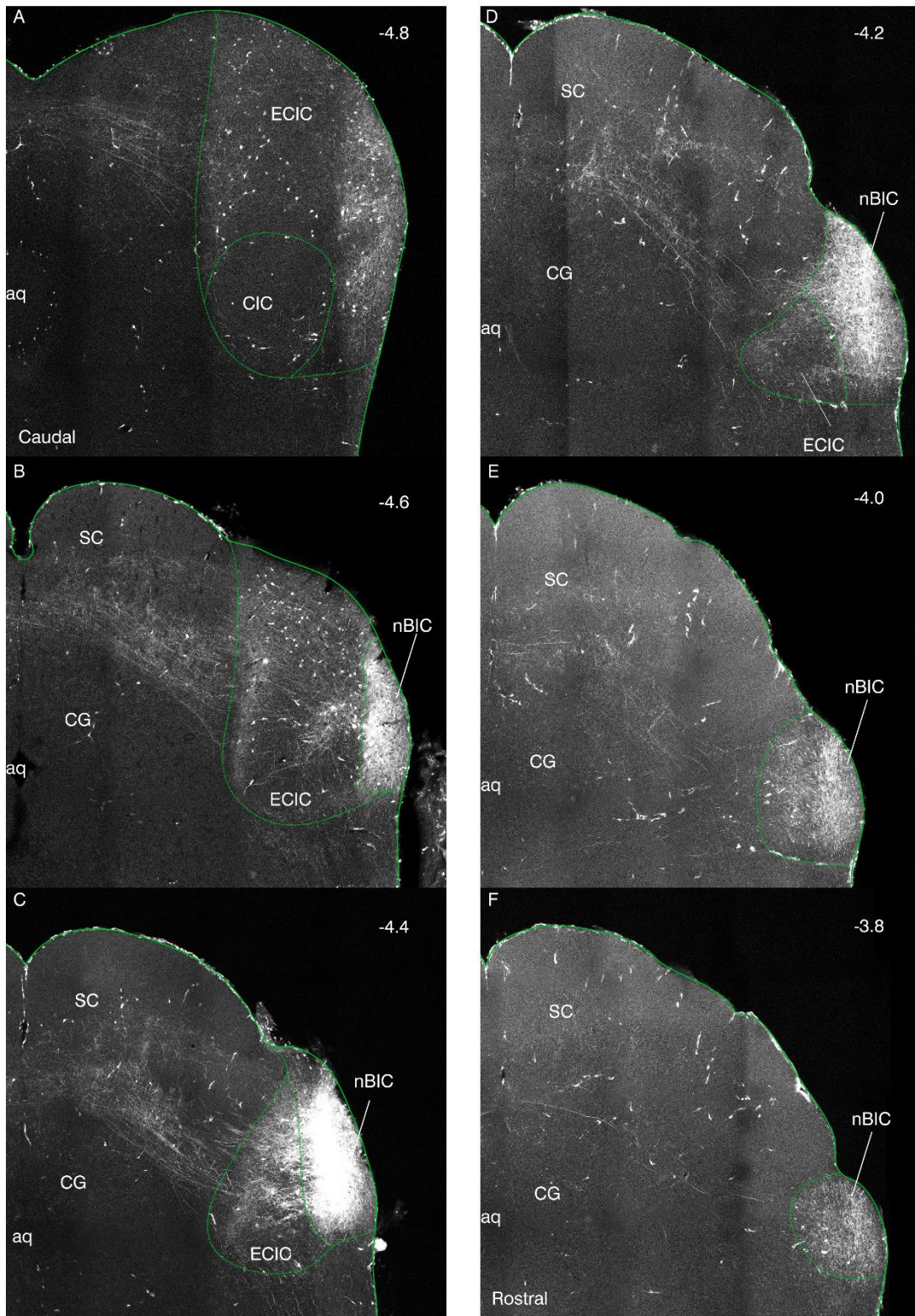




### Figure 3.3 Anatomical tracing of the nBIC/ECIC connections with the SGP layer in the SC

A–F, Confocal images of the rostrocaudal extent after TRITC injection into nBIC/ECIC. The number in the right corner of each image is anteroposterior coordinate relative to bregma (in mm), and images are ordered from caudal to rostral. Note that TRITC has also spread into the capillaries. CG, central grey; aq, aqueduct; ECIC, external cortex of the inferior colliculus; nBIC, nucleus of the brachium of the inferior colliculus; CIC, central nucleus of the inferior colliculus; SC, superior colliculus.

### 3.2.2 AAV-BASED ChR2 VECTORS EFFECTIVELY TRANSDUCE nBIC/ECIC NEURONS

In order to test whether AAV-based vector delivery can be used in the nBIC/ECIC-SGP circuit, an AAV2/1.hSyn.ChR2.eYFP.WPRE.hGH was injected unilaterally into the nBIC/ECIC of P24 old anaesthetized C57BL/6 mouse (N = 1). Two weeks after the *in vivo* injection, the animal was sacrificed and slices of 50  $\mu\text{m}$  thickness were mounted onto glass slides and cover-slipped for imaging of enhanced yellow fluorescent proteins (eYFP) expression. Successful injection could be observed after the visualization of eYFP in the fixed brain tissue (Fig. 3.4). The bulk of the injection was detected in both the nBIC and the ECIC (Fig. 3.4A). In a magnified image of the SGP, eYFP-positive axonal projections of the nBIC/ECIC were visible (Fig. 3.4B). The injection site in the nBIC/ECIC exhibited a substantial amount of eYFP positive axons and tissue debris, consistent with previous reports (Miyashita *et al.*, 2013). The eYFP positive neuronal cell bodies could not be identified (Fig. 3.4C) because the ChR2.eYFP was diverted into the membranes of the neurons rather than their cytoplasm as would be expected. Thus, in this midbrain region, the AAV2/1 did indeed infect neurons within the injection site and the vector it carried integrated into the genome of the nBIC/ECIC neurons to produce the eYFP protein.

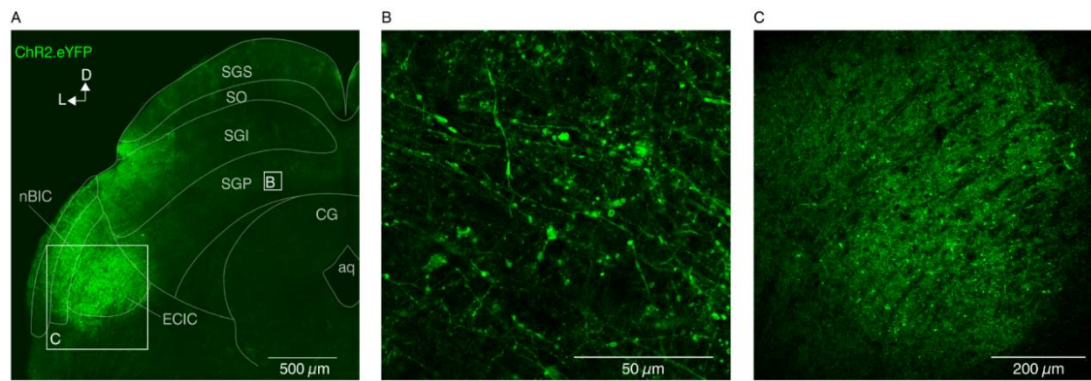


**Figure 3.4 AAV-based eYFP.ChR2 expresses in the nBIC/ECIC and their axons in the SGP**

**A–C**, Confocal images of fixed brain slices after the injection of AAV2/1.hSyn.ChR2.eYFP.WPRE.hGH into the nBIC/ECIC. Insets in (A) are magnified in (B) and (C). SGS, stratum griseum superficiale; SO, stratum opticum; SGI, stratum griseum intermediale; SGP, stratum griseum profundum; CG, central grey; aq, aqueduct; ECIC, external cortex of the inferior colliculus; nBIC, nucleus of the brachium of the inferior colliculus. Modified from Bednárová *et al.* (2018).

### 3.2.3 PHOTOACTIVATABLE nBIC/ECIC NEURONS AFTER THE AAV.eYFP.ChR2 INJECTION

While histologically the eYFP positivity at the injection site in the nBIC/ECIC and also in the axons projecting into the SGP layer of the mouse SC was visible, a confirmation that the ChR2 was functionally inserted into the membranes of the nBIC/ECIC neurons was necessary. In order to test this, the same injection as in Subsection 3.2.2 was performed in C57BL/6 mice (N = 4). Two weeks after the injection the animals were sacrificed and brain slices of 300 μm thickness were prepared to record from both the nBIC and ECIC neurons and to optically stimulate locally over their somas and proximal dendrites (Fig. 3.5A). At lower intensities (Fig. 3.5B, top), I was able to induce inward currents in voltage-clamp (Fig. 3.5B, left) as well as depolarizing potentials in current-clamp (Fig. 3.5B, right) with nearly no latency, and at higher intensities larger currents were able to reliably evoke an AP (Fig. 3.5B, right bottom). The laser intensity

that evoked spikes in nBIC/ECIC neurons was  $35 \pm 14 \mu\text{W}$  (mean  $\pm$  SEM,  $n = 10$  nBIC/ECIC neurons). There were no differences in the laser intensity evoking spikes in nBIC or in ECIC neurons (nBIC  $19 \pm 8 \mu\text{W}$ ,  $n = 5$ , ECIC  $50 \pm 27 \mu\text{W}$ ,  $n = 5$ ,  $p = 0.83$ , Kruskal–Wallis test). While single-cell eYFP.ChR2 positivity is difficult to see in the confocal overview image (Fig. 3.5A and Fig. 3.4C), the somatic eYFP expression is easily detected under the two-photon microscope (Fig. 3.5C). Altogether, these data strongly suggest that the ChR2 was indeed functionally inserted into the membranes of neurons at the injection site in the nBIC/ECIC.

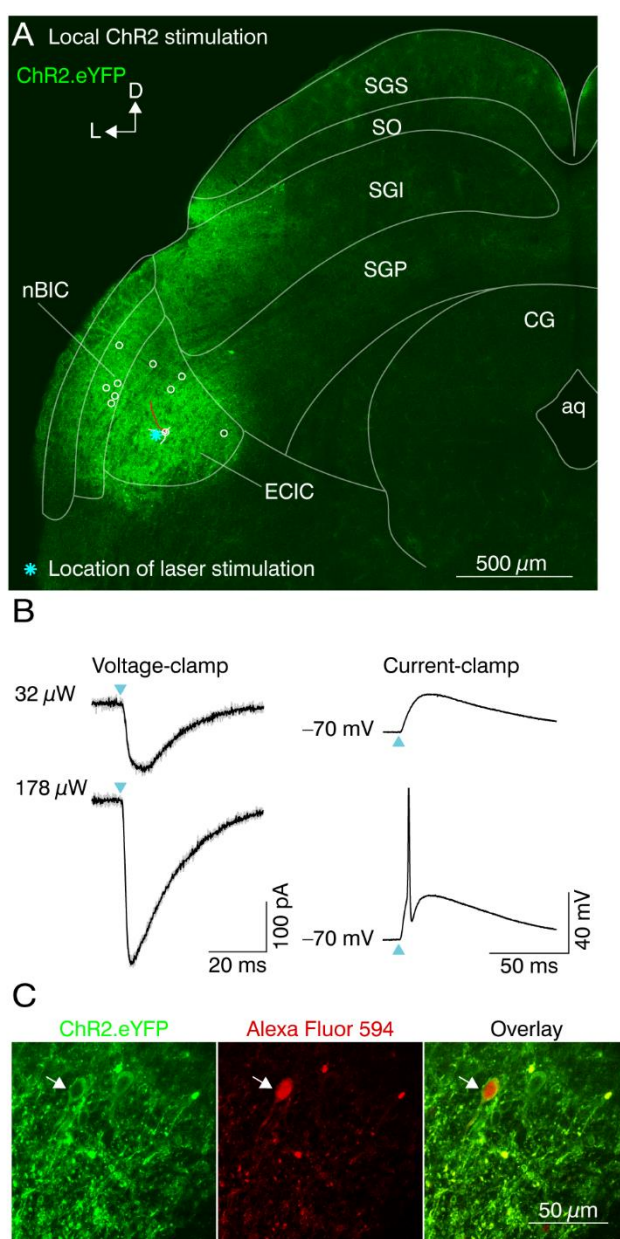


### Figure 3.5 Optical activation of ChR2 positive neurons in the nBIC/ECIC

**A**, Confocal image of a brain slice showing eYFP fluorescence in the nBIC/ECIC. An example ECIC neuron was partially traced (white lines, dendrites and soma; red line, axon). Locations of all nBIC ( $n = 5$ ) and ECIC ( $n = 5$ ) neurons are shown with open circles. Cyan asterisk shows the laser position for an example ECIC recording shown in (B). **B**, Example recording of a local ChR2 stimulation. Voltage-clamp (left,  $V_{\text{holding}} = -70$  mV) and current-clamp (right) recordings of an ECIC neuron at low (top) and high (bottom) laser intensities. Cyan triangles indicate the laser onset. Grey and black traces represent individual trials and the average, respectively. **C**, Two-photon images of a recorded neuron located in the ECIC (white arrow) showing ChR2.eYFP fluorescence (left), Alexa Fluor 594 fluorescence (middle) filled via the patch pipette, and their overlay (right). SGS, stratum griseum superficiale; SO, stratum opticum; SGI, stratum griseum intermediale; SGP, stratum griseum profundum; CG, central grey; aq, aqueduct; ECIC, external cortex of the inferior colliculus; nBIC, nucleus of the brachium of the inferior colliculus. Modified from Bednárová *et al.* (2018).

#### 3.2.4 OPTICALLY-INDUCED POSTSYNAPTIC CURRENTS IN THE SGP NEURONS REVEAL DIVERSE INHIBITORY CONNECTIONS FROM THE nBIC/ECIC

In order to study the physiological connectivity of the nBIC/ECIC with the SGP layer of the mouse SC, the same injection as in Subsection 3.2.2 was performed in C57BL/6 mice ( $N = 14$ ). Two weeks after the injection the animals were sacrificed and brain slices of 300  $\mu\text{m}$  thickness were prepared to record from SGP neurons. To study the types of connections between the nBIC/ECIC and the SGP of the mouse SC, I presynaptically activated ChR2.eYFP positive axons within the pathway towards the SGP and recorded the postsynaptic currents of their putative SGP-residing postsynaptic neurons. Figure 3.6A shows a recording and optical stimulation configuration for an example SGP neuron. SGP neurons were voltage-clamped at  $-70$  mV and  $0$  mV to be able to distinguish excitation and inhibition, respectively. At a holding potential of  $-70$  mV, near the reversal potential for chloride, an EPSC with a latency of  $3.6 \pm 0.1$  ms (mean  $\pm$  SD, Fig. 3.6B top left, green traces) was recorded, consistent with the previously reported

direct excitatory projection (Skaliora *et al.*, 2004). At 0 mV, the approximate reversal potential for glutamate, I observed a small residual inward current followed by an IPSC with latency of  $4.6 \pm 0.38$  ms, indicative of a polysynaptic inhibition (Fig. 3.6B top left, red traces). To further investigate this possibility, antagonists of NMDA and AMPA receptors [NBQX and (*R*)-CPP] were added into the bath to block any polysynaptically-induced inhibition (Fig. 3.6B, middle left). Under these conditions, the EPSC was effectively abolished, but surprisingly, the IPSC (latency  $4.5 \pm 0.15$  ms) remained, albeit with a slightly lower amplitude. In two further experiments picrotoxin (the blocker of GABA<sub>A</sub> receptors) was also added in addition to the blockers of excitation, one of which is shown in Figure 3.6B, right. All remaining currents were abolished (Fig. 3.6B, bottom right), thus confirming that the direct inhibition is indeed GABAergic. Importantly, this direct IPSC, to varying extents, was observed in 100% of SGP neurons recorded ( $n = 25$ ). Thus, in addition to the previously described excitatory pathway, more than one inhibitory connection comprises the nBIC/ECIC-SGP input circuitry.

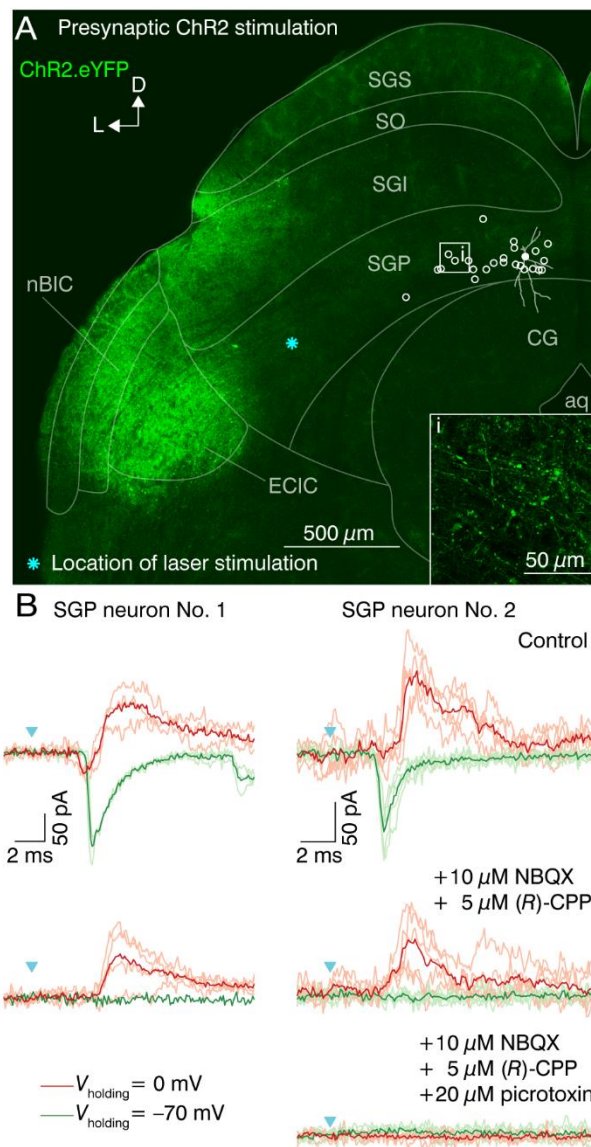


**Figure 3.6 Optical activation of ChR2 positive axons in the nBIC/ECIC-SGP circuit**

A, Confocal image of a brain slice showing ChR2.eYFP fluorescence in the nBIC/ECIC. Higher magnification reveals eYFP positive axons projecting into the SGP (i). In presynaptic ChR2 stimulation, the locations of all recorded SGP neurons are shown by open circles. The filled circle denotes an SGP neuron whose voltage-clamp recordings are presented in (B, left). Cyan asterisk shows the laser position. B, Voltage-clamp recordings of two SGP neurons and presynaptic ChR2 stimulation. An EPSC (green trace,  $V_{\text{holding}} = -70$  mV) and an IPSC (red trace,  $V_{\text{holding}} = 0$  mV) were recorded in control conditions (top), after NBQX and (R)-CPP wash-in (middle), and after picrotoxin wash-in (bottom, right). Lighter and darker traces represent individual trials and averages, respectively. Cyan triangles indicate the laser onset. SGS, stratum griseum superficiale; SO, stratum opticum; SGI, stratum griseum intermediale; SGP, stratum griseum profundum; CG, central grey; aq, aqueduct; ECIC, external

cortex of the inferior colliculus; nBIC, nucleus of the brachium of the inferior colliculus. Modified from Bednárová *et al.* (2018).

While the presence of a direct inhibitory input to the SGP is irrefutable under conditions where excitation is blocked, the precise contribution of the polysynaptic inputs was less trivial to calculate (Fig. 3.7A). This is because trial-by-trial amplitude fluctuations were too large to accurately quantify differences in IPSC amplitudes between the mixed (control) and direct-only (excitatory block) conditions. To obtain a rough picture of the prominence of polysynaptic inputs in the SGP neuronal population, Kruskal–Wallis tests comparing IPSC amplitudes before and after blocking the excitation were performed and this was done for all laser stimulation positions in which the IPSCs in the control condition exceeded 7 times the SD of the baseline. An example of 16 laser stimulation positions (Fig. 3.7B) and the recordings (Fig. 3.7C) for one SGP neuron illustrates how the analysis was performed. In this neuron, six laser stimulation positions induced currents that exceeded the threshold – two of those positions are enlarged in Figure 3.7D, E. In Figure 3.7D, the application of drugs decreased IPSC amplitude significantly (mean  $\pm$  SD IPSC peak difference  $119.7 \pm 12.6$  pA,  $p < 0.05$ , Kruskal–Wallis test). Interestingly, in Figure 3.7E the double-peaked IPSC disappeared in the drugs condition, while the IPSC amplitude simultaneously decreased (mean  $\pm$  SD IPSC peak difference  $145.7 \pm 50.3$  pA,  $p < 0.05$ , Kruskal–Wallis test). Thus, for this particular SGP neuron, there was a significant contribution of polysynaptically-mediated inhibition in 5/6 laser stimulation positions. In SGP population data, the recordings where blocking excitation significantly decreased the IPSC amplitude ( $p < 0.05$ , Kruskal–Wallis test) were regarded as polysynaptic containing connections (30/346 positions) and the number of neurons in which at least one such a connection was calculated was 15 out of 25 SGP neurons. On the other hand, the IPSCs where blocking excitation did not decrease IPSC amplitude were considered direct inhibition-dominated

(316/346 positions). Thus, under these experimental conditions, the magnitude of the polysynaptic inhibition was small (9% out of all positions) in comparison to the striking direct inhibition (91% out of all positions). Because of its presence in all SGP neurons recorded, I focused the rest of the study on the functional and anatomical organization of the direct inhibitory connection.



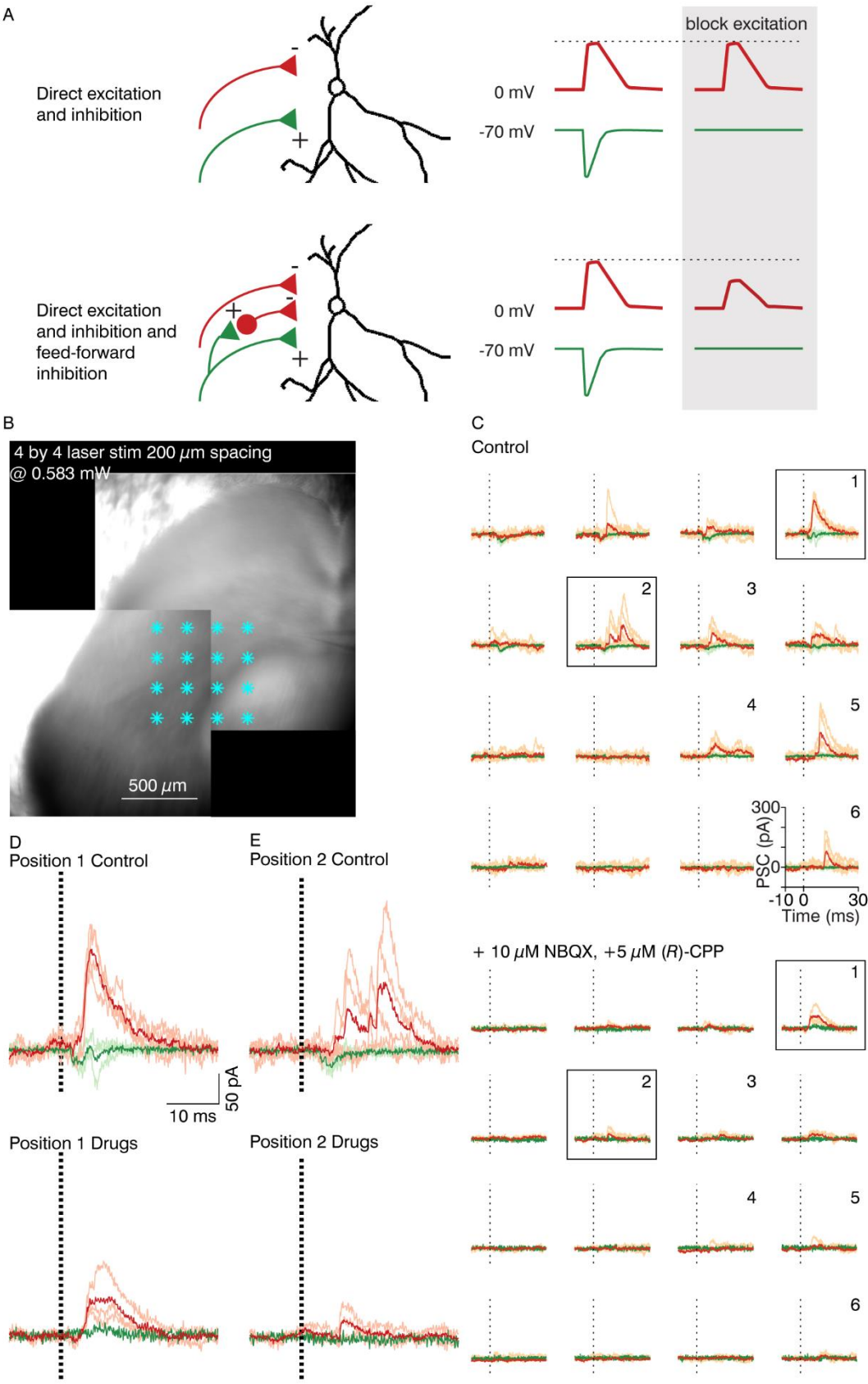


Figure 3.7 Comparison of IPSC amplitudes to distinguish polysynaptically from monosynaptically-induced inhibitions in SGP neurons

**A**, Scheme of the types of nBIC/ECIC inputs that the SGP neurons could receive. In direct excitation and inhibition (top), pharmacological excitatory block should not produce accompanying decreases in IPSC amplitude. If feed-forward inhibition was present (bottom), the excitatory block should not activate the inhibitory interneuron, thereby decreasing overall inhibitory input onto the SGP neuron. **B**, Montage of two Dodt gradient images that shows the recording electrode location in the SGP and the presynaptic laser stimulation locations (cyan asterisks). The same laser power was used to perform all the recordings for this neuron. **C**, Voltage-clamp recording at  $-70$  mV (green traces) and  $0$  mV (red traces) from a neuron recorded in the configuration shown in (A), either in the control condition (top) or in the drugs wash-in condition (bottom). Stimulation positions which induced currents that passed the threshold are marked with a number. Individual traces within the rectangles labelled 1 and 2 are enlarged in (C) and (D), respectively. **D–E** Voltage-clamp recordings of two laser positions: Position 1 in (C) and Position 2 in (D). Individual repetitions are shown as lighter traces and darker traces are the averages. Two holding commands,  $-70$  mV (green) to record EPSCs and  $0$  mV (red) to record IPSCs, were used. Top traces are in the control condition, bottom traces are in the drugs wash-in condition. The scale bar applies to both C and D.

### 3.2.5 DIRECT INHIBITION FROM THE nBIC/ECIC REACHES ALL THREE TYPES OF SGP NEURONS

For 23 out of the 25 recordings using Chr2 stimulation (Subsection 3.2.4), I was able to obtain intrinsic electrophysiological recordings and thus could classify neurons according to their electrophysiological profile as was done in Results 3.1. The intrinsic electrophysiology data from these neurons were then used for subsequent clustering analysis (Fig. 3.8). As was performed in Results 3.1, five parameters were extracted from the recorded traces: the input resistance, the maximum firing rate (at  $700$  pA current injections), the ratio of the first to second inter-spike intervals ( $ISI_1/ISI_2$ ), the time from the current step onset to the first AP (measured at the AP current threshold), and the Spike half-widths. These parameters were then ran in a hierarchical clustering algorithm (Fig. 3.8A). Although the algorithm separated the late-spiking cluster very well from the rest of the neurons (Linkage distance: 2.21), the separation into three clusters (Linkage

distance: 1.60, arrow in Fig. 3.8A, right) was close to 4-5 clusters (Linkage distance: 1.24). Thus, although the algorithm produced hierarchical tree with visually apparent three-cluster separation, the linkage distance between spike-adapting and fast-spiking neurons was not as clear. Here, a couple of interesting observations must be addressed.

Within the fast-spiking cluster of neurons, there seemed to be large linkage distances of a couple of neurons to the rest of the cluster. For example, the neurons with numbers 11 and 14 were clearly clustered together but their distance to the rest of the fast-spiking cluster was quite long. Interestingly, plotting the parameters cluster-wise revealed that these two neurons had extraordinarily large input resistances (663.2 M $\Omega$  for neuron number 11, 627.1 M $\Omega$  for neuron number 14, Fig. 3.8B,  $R_m$ ) compared to the mean and SD values of the fast-spiking cluster ( $359 \pm 149.8$  M $\Omega$ ). While in the rest of the parameters these two neurons fall within the cluster mean and SD, the stark difference in input resistance could explain the larger linkage distance value. Thus, it is tempting to speculate that these two neurons could be a subtype of the fast-spiking neurons.

In addition, the neurons 6 and 16 were also clustered together as compared to the rest of the fast-spiking cluster. Clearly, these two neurons nearly seemed like outliers in the cluster-wise parameters plot (Fig. 3.8B): their input resistance was  $\sim 200$  M $\Omega$  (199.9 M $\Omega$  for neuron number 6, 188.8 M $\Omega$  for neuron number 16), and they could sustain larger firing rates than the mean  $\pm$  SD of the fast-spiking cluster (324.0 Hz for neuron number 6, 281.3 Hz for neuron number 16, cluster mean  $\pm$  SD  $225.6 \pm 44.46$  Hz), which could also be explained by their very brief action potential widths as compared to the cluster mean and SD (0.24 ms for neuron number 6, 0.34 ms for neuron number 16, cluster mean  $\pm$  SD  $0.45 \pm 0.1$  ms). Because of these differences, it is tempting to speculate that there is an additional neuronal cluster for which there either was not enough neurons, or

the differences in the collected parameters between these two neurons and the rest of the fast-spiking cluster were too subtle.

As these four neurons could seem as outliers ( $R_m$  outside of the SD range), I re-ran the clustering algorithm without them, and it created three very well separated clusters (Linkage distance 1.92 for three clusters, Linkage distance 1.19 for four clusters), suggesting that these four SGP neurons could have been responsible for the shortened distances of the adapting and fast-spiking clusters. The 19 SGP neurons were then used for analysis of the strength of the direct inhibition on each of the three electrophysiological clusters (below).

Lastly, although there were only four SGP neurons within the late-spiking cluster, their within-cluster linkage distance was fairly large, leaving the two pairs of neurons well separated (Fig. 3.8A, left, green parts of the cluster tree). It has been previously reported that the late-spiking property is dependent on the resting membrane potential of the neuron (Saito & Isa, 1999), and this could be reflected in the ratio of  $ISI_1$  to  $ISI_2$ . This parameter, when plotted cluster-wise (Fig. 3.8B,  $ISI_1/ISI_2$  ratio) had a large distribution spread for the four SGP neurons, possibly reflecting the resting membrane potential of the SGP neurons. SGP neurons with late-spiking property dependent on the resting membrane potential were encountered during the recordings, but the clustering algorithm nevertheless grouped the late-spiking neurons together.

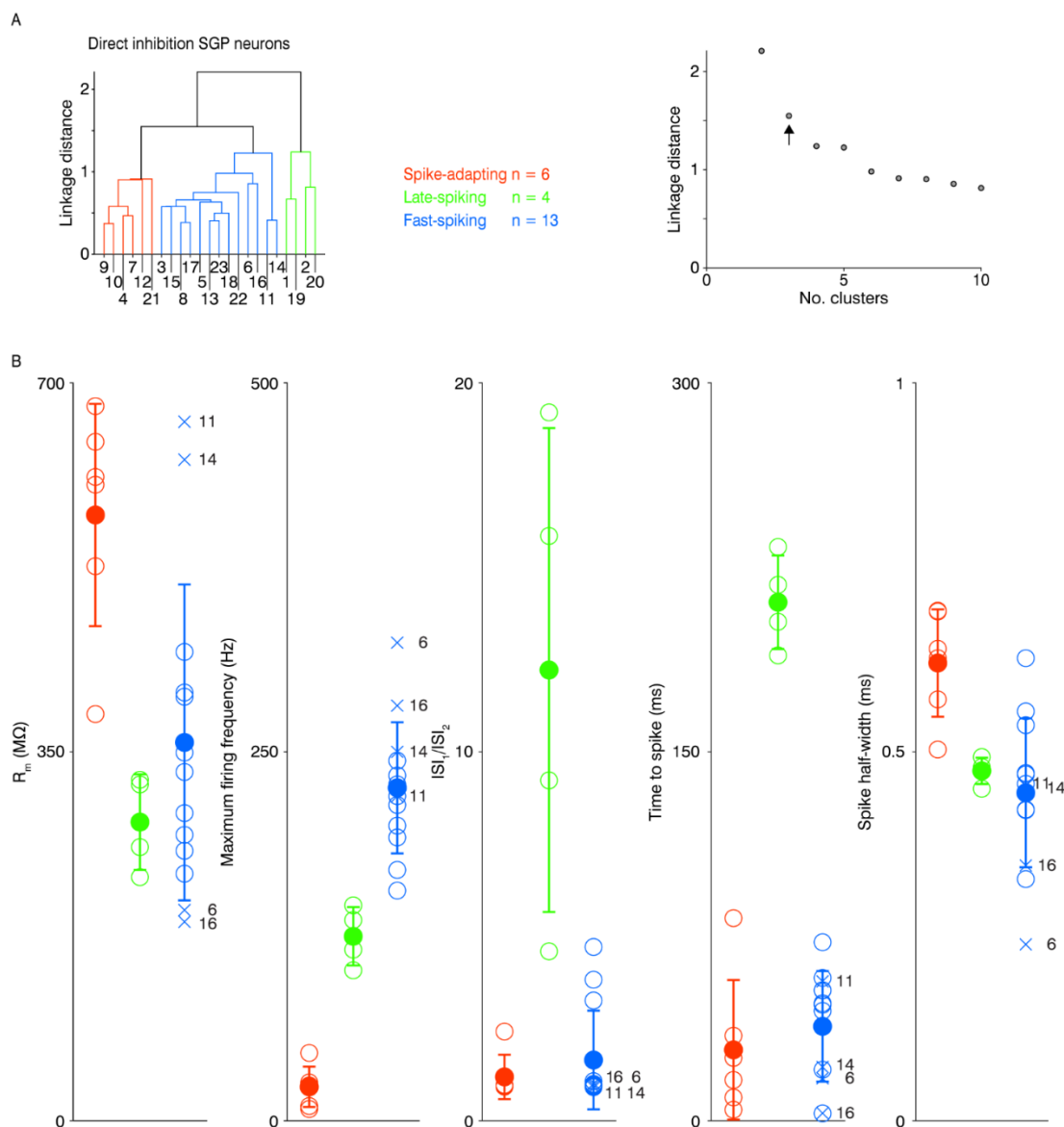


**Figure 3.8 Hierarchical clustering analysis of SGP neurons with direct inhibition**

**A**, Dendrogram plot of hierarchical binary cluster tree (left) of SGP neurons with direct presynaptic inhibition from the nBIC/ECIC. Numbers on the bottom are arbitrary number identifications for each SGP neuron. Linkage distance of the hierarchical clustering is shown as a function of the increasing cluster number (right). The arrow indicates the linkage distance for three clusters. **B**, Cluster-wise plots of the following intrinsic parameters (from left to right): input resistance ( $R_m$ ), maximum firing frequency at the current step of +700 pA, ratio of the first to second inter-spike intervals in a train of APs ( $ISI_1/ISI_2$ ), time to first spike from the current onset at threshold traces, the half-width of the first fired AP. Empty circles represent individual neurons and filled circles represent the cluster mean  $\pm$  SD. Neurons symbolized with x and a number are discussed in the text.

This data clearly shows that direct inhibition from nBIC/ECIC was delivered to all three SGP neuron types. To evaluate the strength of the direct inhibition on each of the three electrophysiological clusters, the direct inhibitory peak values for all 19 SGP neurons were plotted cell type-wise and stimulation position-wise (Fig. 3.9). In the cell type-wise plots (Fig. 3.9, left), the spike-adapting neurons had on average (mean  $\pm$  SD)  $146.4 \pm 77.1$  pA ( $n = 6$ ), the late-spiking  $93.5 \pm 24.3$  pA, and fast-spiking  $117.7 \pm 83.9$  pA IPSC peak amplitudes and their distributions were not different from each other (spike-adapting v. late-spiking  $p = 0.14$ , late-spiking v. fast-spiking  $p = 0.53$ , spike-adapting- v. fast-spiking  $p = 0.51$ , two-sample Kolmogorov–Smirnov test). Analysis of the IPSC amplitudes stimulation position-wise (Fig. 3.9, right) revealed significant differences in the distributions of late-spiking ( $91.0 \pm 51.7$  pA,  $n = 101$ ) to spike-adapting ( $150.8 \pm 96.5$  pA,  $n = 48$ ,  $p = 0.0003$ , two-sample Kolmogorov–Smirnov test) and fast-spiking neurons ( $180.9 \pm 177.3$  pA,  $n = 119$ ,  $p = 0.003$ , two-sample Kolmogorov–Smirnov test), but not between spike-adapting and fast-spiking neurons ( $p = 0.23$ , two-sample Kolmogorov–Smirnov test). Thus, the position-wise analysis indicates that late-spiking neurons receive weaker direct inhibition compared to their spike-adapting and fast-spiking counterparts. However, the fact that the cell-wise analysis, though exhibiting the same trends, returned no statistical significance between cell types, it can be concluded that all cell types receive similar levels of direct inhibition. Nevertheless, because of the presence of the direct inhibition in all SGP neurons recorded, the rest of the study was therefore focused on the functional and anatomical organization of this ubiquitous connection.

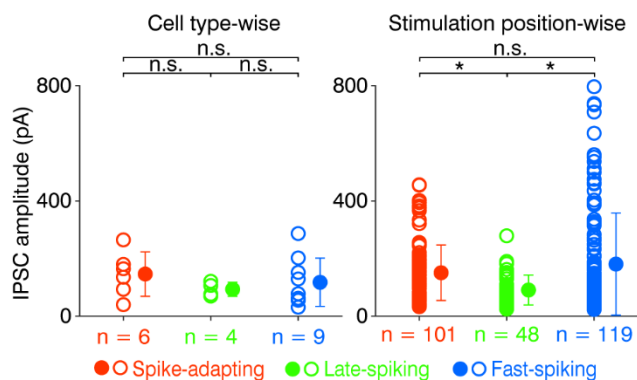


**Figure 3.9 Strength of direct inhibition on SGP neurons cell type-wise and stimulation position-wise**

The open circles in the cell type-wise plot (left) show average IPSC amplitude of a given SGP neuron and the closed circles show the cell cluster mean  $\pm$  SD. In the stimulation position-wise plots (right), the open and closed circles denote the IPSC amplitude of a given stimulation position and their mean  $\pm$  SD, respectively. \*,  $p < 0.05$ ; n.s., not significant (two-sample Kolmogorov–Smirnov test). Modified from Bednárová *et al.* (2018).

### 3.2.6 DIFFERENCE IN THE DISTRIBUTION OF DIRECT EXCITATORY AND INHIBITORY nBIC/ECIC AXONS

In the previous Subsection 3.2.5, I showed that a monosynaptic inhibitory projection exists between the nBIC/ECIC and the SGP of the mouse SC and this direct inhibition reaches all types of neurons found in the SGP. In subsequent parts of the Results, I concentrated on characterizing this unique connection. First, I wondered whether the excitatory and inhibitory axons originate from the same areas and whether they fasciculate tightly with one another within the nBIC/ECIC. To test this, Chr2-assisted circuit mapping (Petreanu *et al.*, 2007) was used to locate the excitatory and the inhibitory axons in the nBIC/ECIC. For this purpose, a grid of  $8 \times 8$  laser stimulation sites with  $175 \mu\text{m}$  spacing was created. The stimulation grid covered both the nBIC and the ECIC, spanning a  $1.2 \times 1.2 \text{ mm}^2$  large region from the lateral slice edge to the CG (Fig. 3.10A). To be sure that the laser stimulated distal nBIC/ECIC inputs of the SGP neurons, the SGP neurons recorded from were located at least  $400 \mu\text{m}$  from the medial edge of the

grid ( $n = 10/25$  SGP neurons, SGP neurons were located outside of the area shown in Fig. 3.10A). Recordings of three representative neurons (out of ten SGP neurons) were analysed and are shown as input heat maps in Figure 3.10B–D. Here, the EPSCs and IPSCs evoked by laser stimulation at individual grid locations were used to construct excitatory ( $V_{\text{holding}} = -70$  mV, Fig. 3.10B–D, top) and inhibitory ( $V_{\text{holding}} = 0$  mV, Fig. 3.10B–D, bottom) input maps in control conditions (Fig. 3.10B–D, left). In each input map, individual squares represent an average (from 3 repetitions) of the peak PSC for that particular position. In order to differentiate the locations of the direct inhibitory inputs from the trajectories of the excitatory inputs, the maps were repeated in the presence of NBQX and (*R*)-CPP (Fig. 3.10B–D, right), thereby eliminating the polysynaptic inhibitory components. Each map was then normalized to the maximum peak value of the control condition. For excitation, all maps in the drugs condition became zero by design. Responses in the inhibitory maps persisted, reflecting the direct, monosynaptic inhibitory projections, although slightly more broadly distributed compared to control conditions that contain both mixed and direct inhibition. This subtle difference is likely due to a threshold artefact, whereby the blockers of excitatory transmission increased the input resistance during the IPSC thereby pushing small subthreshold events above the detection threshold. Non-normalized input map current mean and maximum (max) values (mean  $\pm$  SEM) were as follows: Figure 3.10B, control excitation  $41.1 \pm 17.7$  pA, max 72.1 pA; control inhibition  $83.0 \pm 52.8$  pA, max 244.2 pA; drugs inhibition  $61.8 \pm 23.7$  pA, max 132.9 pA; Figure 3.10C, control excitation  $48.0 \pm 22.8$  pA, max 143.7 pA; control inhibition  $43.5 \pm 12.0$  pA, max 68.7 pA; drugs inhibition  $39.1 \pm 14.8$  pA, max 83.6 pA; Figure 3.10D, control excitation  $118.0 \pm 93.6$  pA, max 283.8 pA; control inhibition  $90.0 \pm 29.3$  pA, max 135.8 pA; drugs inhibition  $81.6 \pm 45.6$  pA, max 164.2 pA. Already from these basic analyses, it is visually apparent that while the excitation was more broadly distributed, the direct inhibition seemed confined to the dorsomedial location within the stimulus grid.



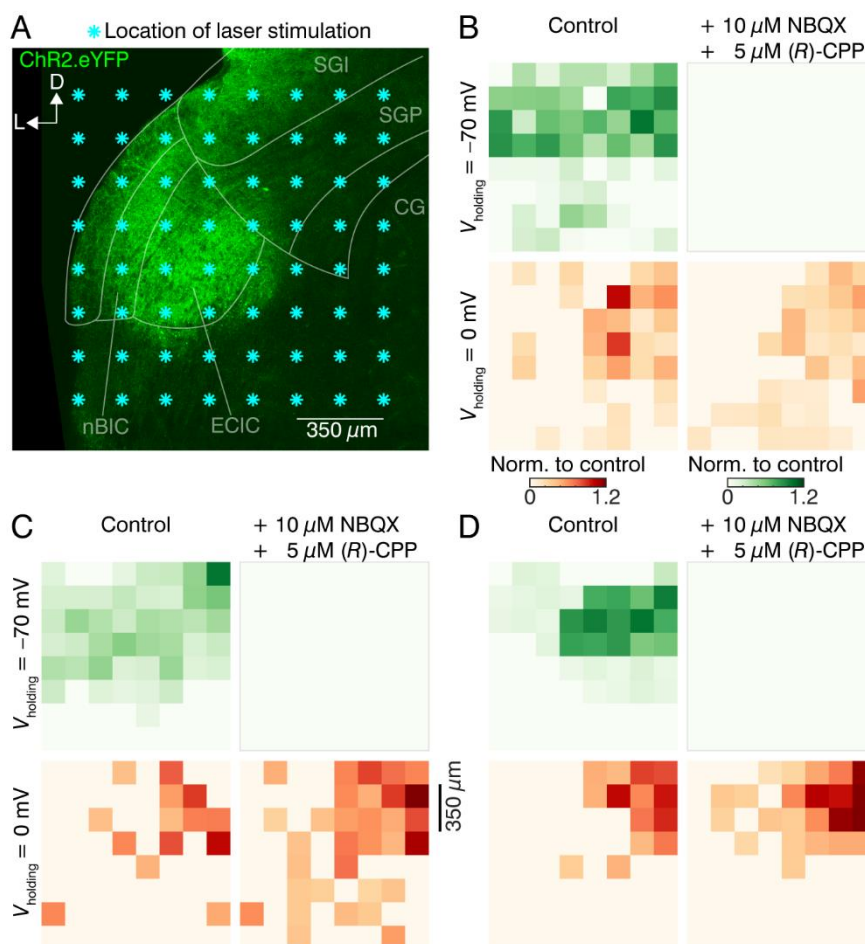


**Figure 3.10 ChR2-assisted circuit mapping of the nBIC/ECIC - SGP circuit**

**A**, Confocal eYFP image of a brain slice with the mapped area covering the nBIC/ECIC for the example SGP neuron recording in (**B**). Each asterisk indicates a location of the laser stimulation grid. Recorded neurons were located at least  $400\ \mu\text{m}$  dorsomedially from the nearest stimulation point. **B–D**, Excitatory ( $V_{\text{holding}} = -70\ \text{mV}$ , top) and inhibitory ( $V_{\text{holding}} = 0\ \text{mV}$ , bottom) input maps created from voltage-clamp recordings for three example SGP neurons. Left and right maps were recorded in control conditions and in the presence of the drugs, respectively. All values are normalized to the maximum value of their respective control condition maps. Note that the post-drugs excitatory maps (upper right map) are by definition zero as excitation was pharmacologically blocked. SGI, stratum griseum intermediale; SGP, stratum griseum profundum; CG, central grey; ECIC, external cortex of the inferior colliculus; nBIC, nucleus of the brachium of the inferior colliculus. With permission from Bednárová *et al.* (2018).

To generalize these findings, the data from excitatory input maps in the control condition and the inhibitory input maps in the drugs condition for ten SGP neurons were averaged (Fig. 3.11A). In general, the strongest responses were observed at positions closer to the recorded neuron. This is to be expected as fibres are less likely to be cut in areas closer to their targets. However, when comparing the direct excitatory and inhibitory distributions, the IPSCs were nearly exclusively induced from the medial extent of the dorsal part of the grid (red colour-scaled circles, Fig. 3.11A, left). In contrast, the EPSCs could be detected in SGP neurons by stimulation across the mediolateral extent of the dorsal part of the grid (green colour-scaled circles, Fig. 3.11A, right).

To quantify these differences, two approaches were taken. In the first approach, Kruskal–Wallis tests were performed on the excitatory and inhibitory responses for each stimulation grid position and the resulting *p*-values were plotted as a heat map (Fig. 3.11B, *n* = 10 SGP neurons). Multiple positions in the dorsolateral part of the grid were found to be statistically different between excitation and inhibition in these regions.

In the second approach, I calculated the input distributions for all ten SGP neurons along the dorsoventral or mediolateral axes (Fig. 3.11C). In the dorsoventral distribution (Fig. 3.11C, left), both the direct and mixed inhibitory as well as excitatory distributions were similar, with most inputs located in the dorsal parts of the nBIC/ECIC. In the mediolateral distribution however, there was a clear medial bias of the direct inhibitory connections compared to their excitatory counterparts (Fig. 3.11C, right). Then, cumulative histograms of the data along each axis were generated and non-parametric statistical analysis on the distribution of their half-maximal positions was performed. Indeed, half-maximal positions from the dorsal slice edge in the dorsoventral axis between direct excitation (control excitation,  $294.2 \pm 56.7 \mu\text{m}$ ) and mixed inhibition (control inhibition,  $309.1 \pm 100.5 \mu\text{m}$ ) as well as direct inhibition (drugs inhibition,

209.9 ± 50.5 μm) were not significant ( $p = 0.706$  and  $p = 0.326$ , respectively, Kruskal–Wallis test), reflecting the fact that in all cases the strongest input came from the dorsal region of the stimulus grid (to be expected as slicing generally preserves axons closer to their targets). In contrast, in the mediolateral axis both mixed and direct inhibition exhibited half-maximal positions significantly more medial (909.7 ± 55.1 and 926.2 ± 43.6 μm from the lateral slice edge, respectively) compared to direct excitation (749.2 ± 40.1 μm,  $p = 0.041$  and  $p = 0.013$ , respectively, Kruskal–Wallis test), reflecting the fact that in the dorsolateral region of the grid the excitation was substantially stronger. Importantly, there were no statistically significant differences in the half-maximal positions along the dorsoventral ( $p = 0.545$ , Kruskal–Wallis test) as well as the mediolateral ( $p = 0.791$ , Kruskal–Wallis test) axes between mixed inhibition and direct inhibition. Thus, broadening of input maps after the application of excitatory blockers as observed in Figure 3.10B–D did not change the spatial distribution of inhibitory inputs on average.

Given such a robust spatial separation between excitatory and inhibitory inputs to the SGP, it would be interesting to see whether such trajectory differences would be reflected in the synaptic latency. Therefore, I calculated mean latency of the control excitatory and the drugs inhibitory maps for grid positions within the nBIC/ECIC in which both IPSCs and EPSCs were evoked (control excitation mean ± SEM, 5.78 ± 1.15 ms, drugs inhibition 4.56 ± 0.60 ms,  $n = 5$  out of 10 SGP neurons which met the criteria,  $p = 0.451$ , paired two-tailed  $t$ -test). Thus, despite the more medially located direct inhibitory inputs, their position-matched latencies were comparable to the direct excitatory inputs, at least at the level of the nBIC/ECIC, which suggests that excitatory and inhibitory inputs take functionally equivalent path lengths to their target neurons in the SGP.

Although the results from the ChR2-assisted circuit mapping experiments clearly show a trajectory bias of the inhibitory inputs toward the medial side, it is difficult to conclude whether the projection cell bodies are also differentially distributed within the nBIC/ECIC because ChR2 activation in both the axons and cell bodies can generate APs. I therefore used two methodological approaches to provide evidence for the existence of SGP-projecting inhibitory cells in the nBIC/ECIC.

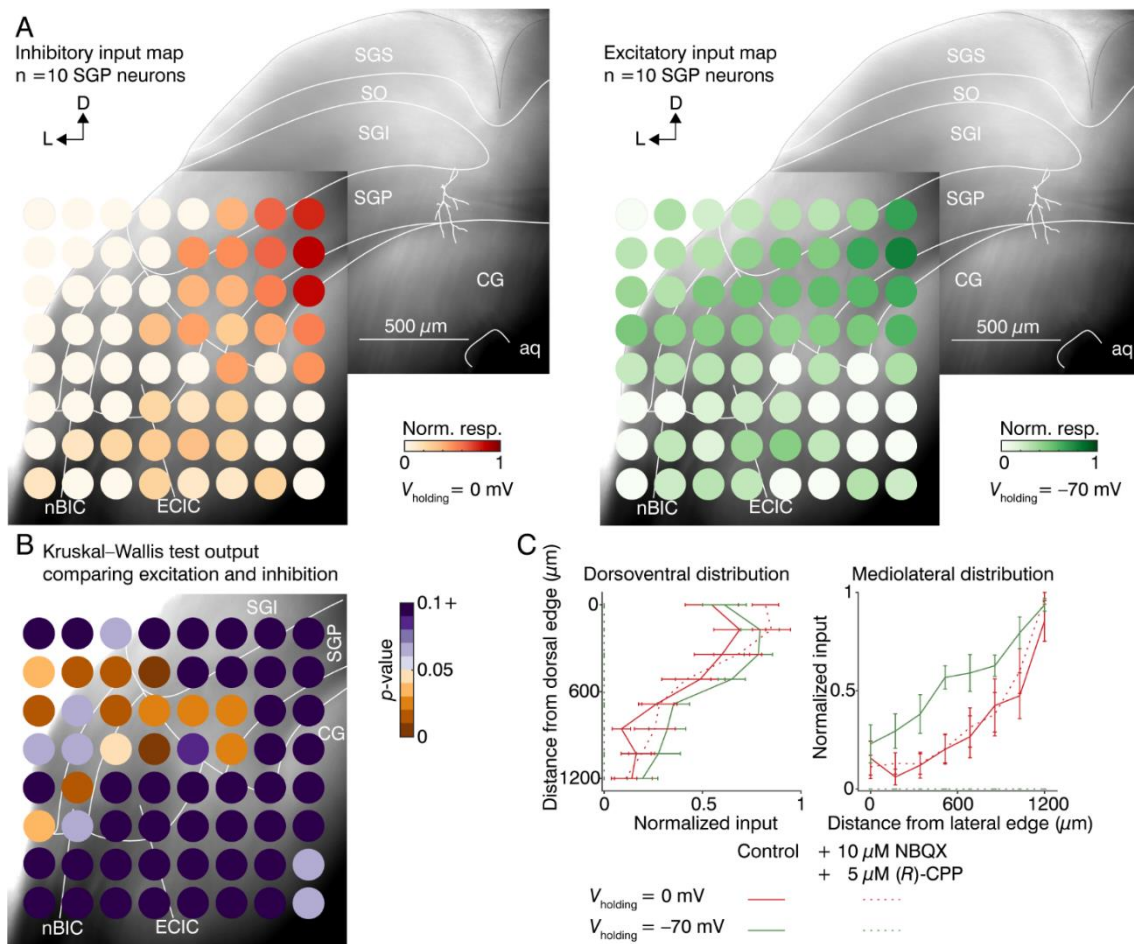


**Figure 3.11 Mapping the locations of the excitatory and the inhibitory nBIC/ECIC inputs to SGP neurons**

**A**, Montage of two Dodt gradient contrast images with direct inhibitory (left) and excitatory (right) input maps averaged for ten SGP neurons. Each circle represents the mean ( $n = 10$  neurons) of the nonzero post-drugs inhibitory responses (left, red colour scale) and control excitatory responses (right, green colour scale). An example traced neuron (white lines) in the SGP is shown for orientation. Note that in this case, the inhibition was normalized to the drugs

(Fig. 3.11 cont.) condition. **B**, Dot gradient contrast image with heat map of  $p$ -values calculated by performing position-wise Kruskal–Wallis tests on the direct inhibitory and excitatory values of data shown in (A). **C**, Quantification of the input distributions in the dorsoventral (left) and mediolateral (right) axes, averaged across ten SGP neurons. Each point along the line is the mean  $\pm$  SEM of the maximal response for one of the eight dorsoventral and mediolateral positions relative to the edge of the slice. SGS, stratum griseum superficiale; SO, stratum opticum; SGI, stratum griseum intermediale; SGP, stratum griseum profundum; CG, central grey; aq, aqueduct; ECIC, external cortex of the inferior colliculus; nBIC, nucleus of the brachium of the inferior colliculus. With permission from Bednárová *et al.* (2018).

### 3.2.7 PHYSIOLOGICAL APPROACH TO FINDING DIFFERENCES IN SPATIAL DISTRIBUTION BETWEEN EXCITATORY AND INHIBITORY NEURON BODIES IN THE nBIC/ECIC

In the first approach, I used a soma-targeted ChR2.eYFP variant (Baker *et al.*, 2016) in order to test whether the direct inhibition could also be evoked by stimulating ChR2 in the somas that reside in the nBIC/ECIC. In comparison to the initially used AAV.ChR2.eYFP, an AAV with a modified ChR2-eYFP.Kv2.1 vector was injected into the nBIC/ECIC region (N = 4 C57BL/6 mice). This vector was previously shown to direct ChR2.eYFP insertion predominantly into the membranes of the somas and proximal dendrites, while it was absent from the axons (Baker *et al.*, 2016). Thus, any optically-induced postsynaptic currents should result from the activation of the nBIC/ECIC somas and not axons using this construct. As is clearly visible from the confocal images, using the previous ChR2.eYFP construct it is difficult to identify eYFP positive cell bodies in the nBIC/ECIC (Fig. 3.12A, left inset), while using the modified construct, the eYFP signal is present in the somas of the nBIC/ECIC neurons (Fig. 3.12A, right inset). I then performed ChR2-assisted circuit mapping experiments as previously described, but with the modified vector. In an example recording of a single SGP neuron (Fig 3.12B), laser stimulation grid was placed over the nBIC/ECIC, and inhibitory maps in control and drugs condition were acquired. Interestingly, in

the control condition a small area in the centre of the grid produced largest IPSCs, and this localized IPSCs withstood the drugs condition, albeit with a slightly lower amplitude. Thus, it looked like this inhibitory island corresponded with an inhibitory neuron soma and its proximal dendrites located in the nBIC/ECIC. Although the IPSCs were largest within this location in both conditions, there were also multiple locations in the medio-dorsal edge of the stimulation grid, which could correspond to the axonal projections of the nBIC/ECIC neurons.

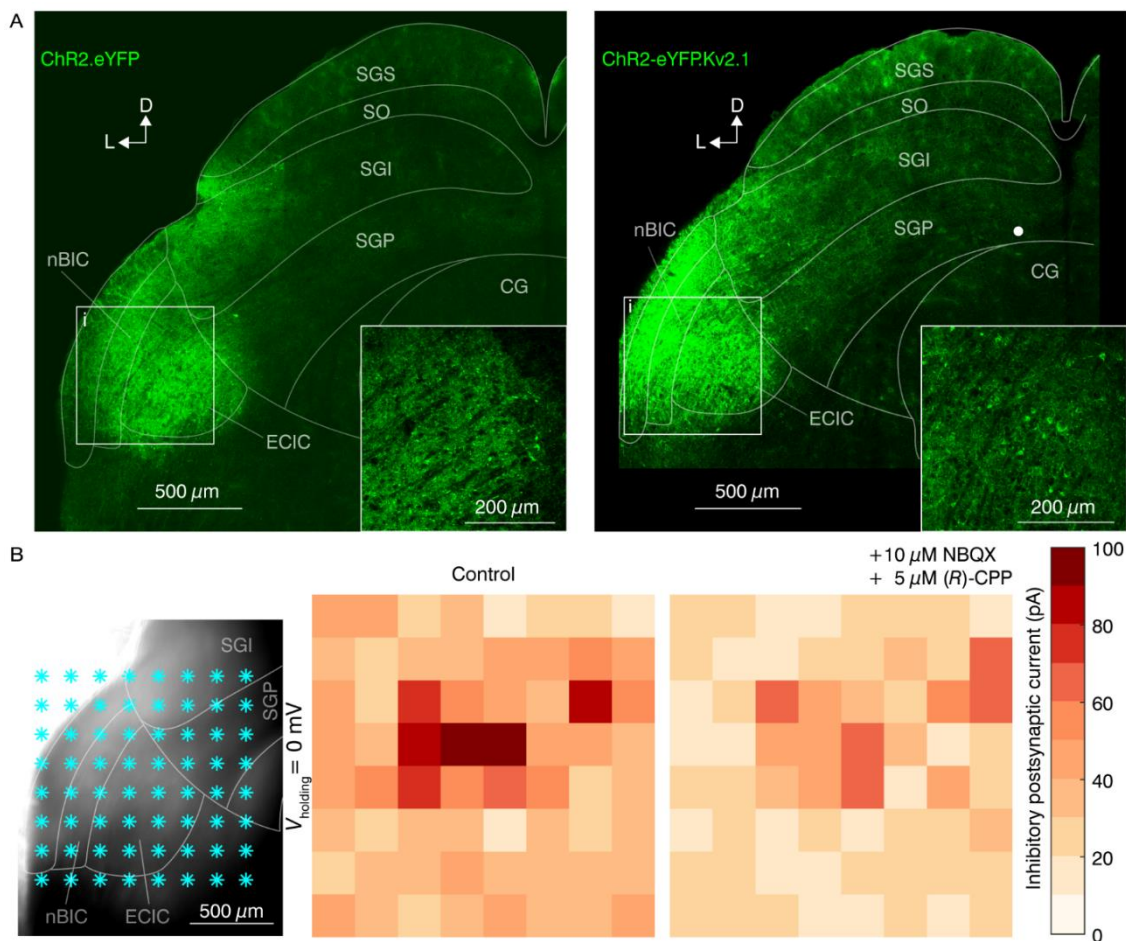


**Figure 3.12 ChR2-assisted circuit mapping of SGP-projecting cell bodies located in the nBIC/ECIC using ChR2-eYFP.Kv2.1**

**A**, Confocal images of fixed brain slices after the injection of AAV2/1.hSyn.ChR2.eYFP.WPRE.hGH (left) or AAV1.hSyn.ChR2-eYFP.Kv2.1.WPRE.hGH (right) into the nBIC/ECIC. Insets (i) are magnified images of the injection sites. The filled circle denotes the location of SGP neuron whose recordings are presented in (B). **B**, ChR2-assisted circuit mapping of a single SGP neuron located outside the field of view in the Dodt contrast image.

(Fig. 3.12 cont.) The locations of laser stimulation positions are shown in the DotD contrast image (left), where each cyan asterisk denotes a single position. The spacing between two neighbouring positions was 175  $\mu\text{m}$ . Colour bar applies to both inhibitory input maps of this SGP neuron in the control (middle) and drugs condition (right). SGS, stratum griseum superficiale; SO, stratum opticum; SGI, stratum griseum intermediale; SGP, stratum griseum profundum; CG, central grey; aq, aqueduct; ECIC, external cortex of the inferior colliculus; nBIC, nucleus of the brachium of the inferior colliculus.

In addition, in other example neurons, such localized islands in the nBIC/ECIC were not present (Fig. 3.13). Rather, I observed strong monosynaptic inhibitory inputs from laser positions that corresponded with the nBIC/ECIC axons running towards the SGP (Fig. 3.13, SGP neuron numbers 2 and 3, compare with Figures 3.10 and 3.11). Moreover, for a number of SGP neurons, monosynaptic IPSCs were recorded by laser stimulating closer to the SGP neuron (Fig. 3.13, SGP neuron number 4), where histologically no eYFP positive cell bodies were present. Thus, it must be that the modified ChR2-eYFP.Kv2.1 was not only soma-targeted in the nBIC/ECIC, but that it was also diverted to the axons of the nBIC/ECIC neurons. Therefore, the optically-induced postsynaptic currents could result from the activation of nBIC/ECIC somas but also axons using this construct, thereby not solving the issue of the somatic vs. axonal ChR2 activation mentioned in the Subsection 3.2.6. Thus, I was not able to address the question about the location of SGP-projecting inhibitory neurons in the nBIC/ECIC using this method.



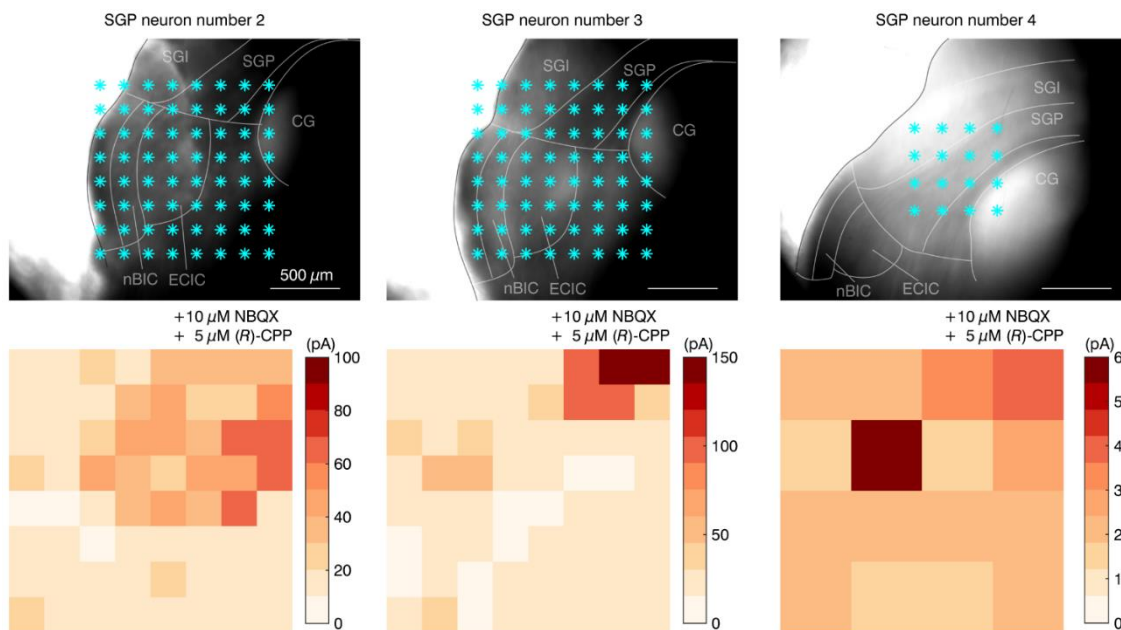


**Figure 3.13 More examples of Chr2-assisted circuit mapping of SGP-projecting cell bodies located in the nBIC/ECIC using Chr2-eYFP.Kv2.1**

Mapped regions (top) and the corresponding inhibitory input maps in drugs conditions (bottom,  $V_{\text{holding}} = 0$  mV) for three example SGP neurons. Spacing between laser positions for neuron numbers 2 and 3 was  $175 \mu\text{m}$  and for neuron number 4 it was  $200 \mu\text{m}$ . Scale bar in Dotd contrast images is the same for all three images. SGI, stratum griseum intermediale; SGP, stratum griseum profundum; CG, central grey; ECIC, external cortex of the inferior colliculus; nBIC, nucleus of the brachium of the inferior colliculus.

### 3.2.8 ANATOMICAL APPROACH TO FINDING DISTRIBUTION DIFFERENCES BETWEEN EXCITATORY AND INHIBITORY NEURON BODIES IN THE nBIC/ECIC

In the second approach, I used tracing and histological methods to characterize the spatial distribution of SGP-projecting neuron somas within the nBIC/ECIC. Here, the retrograde tracer Fluoro-Gold was injected into the SGP of the mouse SC ( $N = 3$  mice), and an immunohistochemical analysis of the tracer-filled neurons in the nBIC/ECIC was performed in order to gain insight into their neurochemical profiles (Fig. 3.14A). Examples of double-labelled neurons are presented in Figure 3.14B, C. Although the total number of neurons retrogradely



labelled in the nBIC was higher than in the ECIC (1389 in nBIC vs. 1112 in ECIC, Table 3), the percentage of those neurons positive for the GAD67 was larger in the ECIC when compared to the nBIC (27% in ECIC vs. 7% in nBIC, 15% overall, Table 3) (Dillingham *et al.*, 2017), providing evidence that cell bodies of SGP-projecting inhibitory neurons match the mediolateral axon trajectories (Fig. 3.11). Moreover, retrogradely labelled neurons also positive for calretinin (although never also positive for GAD67) (Dillingham *et al.*, 2017) were distributed more equally throughout the nBIC and the ECIC regions (22% in ECIC vs. 30% in nBIC, Table 4), a finding also consistent with the more even distribution of the excitatory axon trajectories (Fig. 3.11). Thus, the histological analysis corroborated the electrophysiological experiments, showing a distinct mediolateral distribution of SGP-projecting subpopulation of inhibitory neurons from their excitatory counterparts.

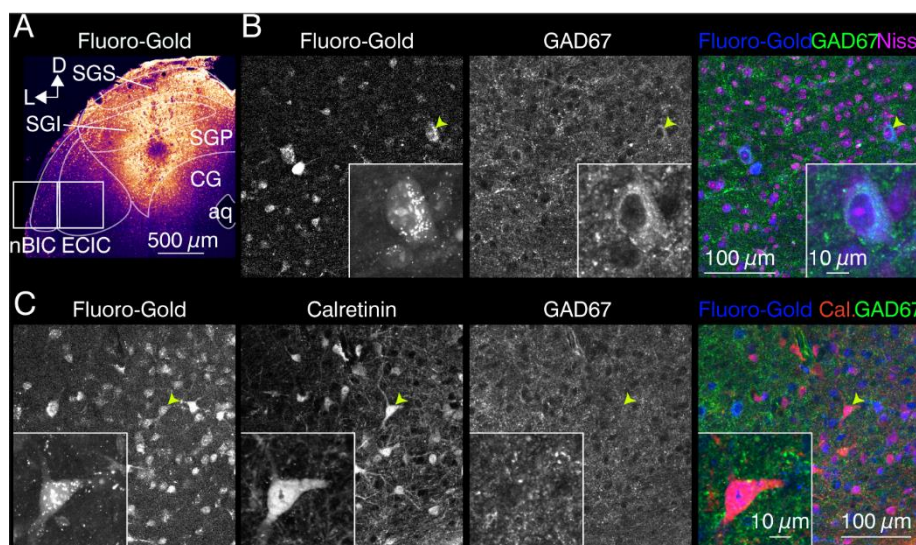


**Figure 3.14 Retrogradely traced nBIC/ECIC neurons and their immunoreactivity for GAD67 and calretinin**

**A**, Confocal image of the Fluoro-Gold injection site in the SGP of the mouse SC. Retrogradely filled neurons were counted in the example highlighted tiles roughly corresponding to the nBIC and the ECIC. **B**, Higher magnification images of a region within the ECIC with Fluoro-Gold filled neurons and their immunoreactivity for GAD67. Neuron highlighted by the arrow is shown in the inset. Data are summarized in Table 3. **C**, Higher magnification images of a

(Fig. 3.14 cont.) region within the nBIC with Fluoro-Gold filled neurons and their immunoreactivity for calretinin and GAD67. Neuron highlighted by the arrow (positive for calretinin, negative for GAD67) is shown in the inset. Data are summarized in Table 4. SGS, stratum griseum superficiale; SGI, stratum griseum intermediale; SGP, stratum griseum profundum; CG, central grey; aq, aqueduct; ECIC, external cortex of the inferior colliculus; nBIC, nucleus of the brachium of the inferior colliculus. With permission from Bednárová *et al.* (2018).

**Table 3 | Numbers and percentage of retrogradely labelled neurons GAD67+**

	nBIC	ECIC
Retro only	1389	1112
Retro GAD67	95	235
% Retro GAD67	7%	27%

N = 3 mice

n = 33 nBIC/ECIC tiles

**Table 4 | Numbers and percentage of retrogradely labelled neurons calretinin +**

	nBIC	ECIC
Retro only	427	411
Retro calretinin	98	74
% Retro calretinin	30%	22%
Retro calretinin GAD67	0	0

N = 3 mice

n = 11 nBIC/ECIC tiles

### 3.2.9 THE MAJORITY OF INHIBITORY nBIC/ECIC SGP-PROJECTING NEURONS ARE PV POSITIVE

The identity of the direct inhibitory projection neurons in the nBIC/ECIC by co-staining for somatostatin, calbindin and PV with GAD67 was investigated. Although there were no cells positive for somatostatin, a small proportion of SC-projecting inhibitory cells in nBIC/ECIC positive for calbindin was found (nBIC 2 out of 15 cells, 13%; ECIC 2 out of 30 cells, 6%, Table 5). The majority of inhibitory cells in the nBIC/ECIC that projected to the SC were PV positive (nBIC 17 out of 20 cells, 85%; ECIC 44 out of 61 cells, 72%, Table 6), although there was

a small proportion of GAD67-negative SC-projecting PV-positive neurons in both the nBIC and ECIC (nBIC 9 out of 434 Retro GAD67-negative cells, 2%; ECIC 3 out of 200 Retro GAD67-negative cells, 1.5%, Table 6). Thus while the majority of SGP-projecting nBIC/ECIC inhibitory neurons are PV positive (with some calbindin exceptions), the identity of the remaining 16% of inhibitory neurons is yet to be determined.

**Table 5 | Numbers of retrogradely labelled cells calbindin immunopositive**

	nBIC	ECIC
Retro only	140	118
Retro GAD67	15	30
Retro calbindin GAD67	2	2
Retro GAD67-	125	88
Retro calbindin GAD67-	31	14

N = 2 mice

n = 4 nBIC/ECIC tiles

**Table 6 | Numbers of retrogradely labelled neurons PV immunopositive**

	nBIC	ECIC
Retro only	454	261
Retro GAD67	20	61
Retro PV GAD67	17	44
Retro GAD67-	434	200
Retro PV GAD67-	9	3

N = 3 mice

n = 11 nBIC/ECIC tiles

### 3.2.10 CONCLUSION

In this this part of the thesis, I investigated the types of connectivity between the nBIC/ECIC and neurons in the SGP layer of the mouse SC using a combination of optogenetic, electrophysiological, and anatomical techniques. The circuitry consists of a monosynaptic excitatory projection which drives a feed-forward inhibition via circuits intrinsic to the SC. All SGP neurons recorded also receive a profound monosynaptic inhibitory connection. The direct

inhibition targets all three types of neurons found in the SGP. The data also showed that the direct inhibitory axons of the nBIC/ECIC are located more medially as compared to their excitatory counterparts, a finding which was also corroborated by a higher percentage of inhibitory neurons projecting to the SGP located more medially than the excitatory SGP-projecting neurons. Finally, the majority of the direct inhibitory neurons in the nBIC/ECIC is of PV nature with some calbindin exceptions.

### **3.3 ANATOMICAL AND FUNCTIONAL CONNECTIVITY OF PV nBIC/ECIC NEURONS WITH THE SGP OF THE MOUSE SC**

The majority of inhibitory neurons in the nBIC/ECIC projecting into the SGP of the mouse SC was PV positive (Subsection 3.2.9). To investigate PV in the long-range projecting inhibitory connections described in Results 3.2, the anatomical and physiological connection of specifically the PV neurons in the nBIC/ECIC with the SGP layer of the mouse SC was probed.

#### **3.3.1 PV IS EXPRESSED IN SOMAS AND AXONS OF THE MOUSE nBIC/ECIC NEURONS**

In preliminary experiments, an immunohistochemical analysis for PV positivity was performed in brain slices obtained from a CBA/Caj mouse (N = 1). In coronal slices (Fig. 3.15), PV was abundant, especially at the level of the inferior colliculus (Fig. 3.15, Caudal). More rostrally, at the level of the SC, PV-positive cell bodies could be found concentrated in the ECIC (Fig. 3.15, Middle top). In the same section, fairly prominent PV positive axonal projections could be observed in the SGP (Fig. 3.15, Middle bottom). In the rostral brain section, while the accumulation of PV neurons in the ECIC was more concentrated to a smaller region (Fig. 3.15, Rostral top), the axons in the SGP layer were still present (Fig. 3.15, Rostral bottom). The lower expression of PV in the ECIC somas in the more rostral section suggests that PV inferior colliculus neurons are present caudally from the SC. The PV axonal projections were detected in the SGP rostro-caudally, suggesting that PV neurons might project rostrally from where their neuronal bodies lie in the ECIC.

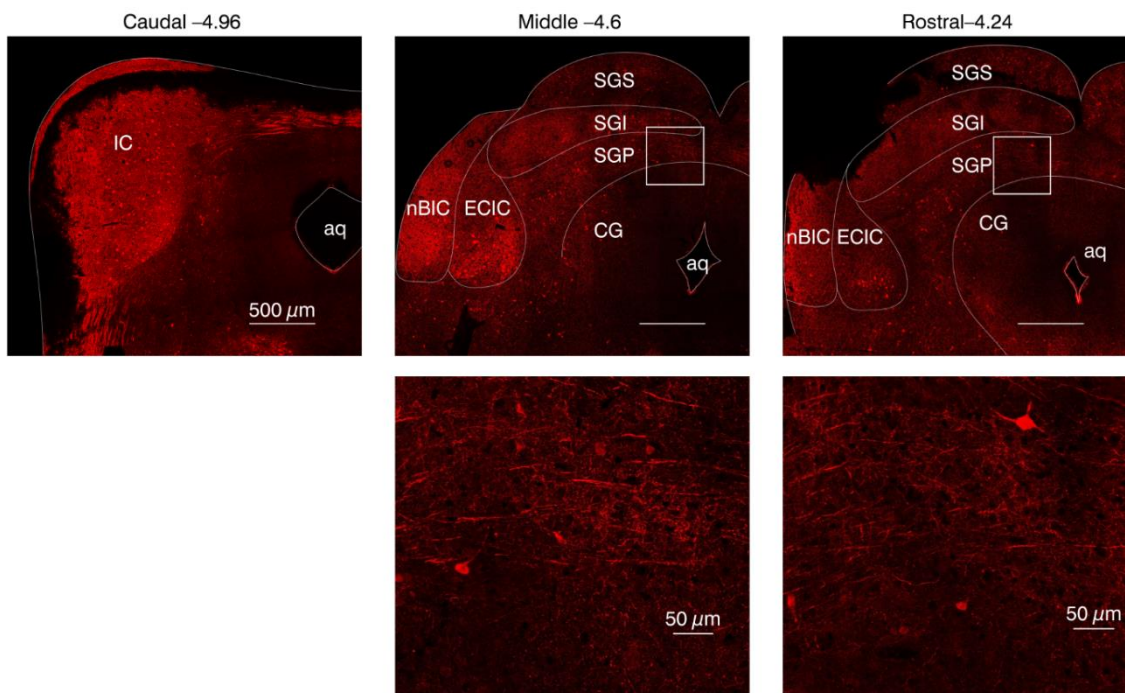


**Figure 3.15 PV positivity in the rostrocaudal extent of the IC to the SC in a WT CBA/Caj mouse**

The numbers on the top of the images are coordinates (in mm) relative to Bregma. Insets (bottom) show zoom-ins on PV positive axons in the regions in the SGP for the Middle and the Rostral sections. IC, inferior colliculus; SGS, stratum griseum superficiale; SGI, stratum griseum intermediale; SGP, stratum griseum profundum; CG, central grey; aq, aqueduct; ECIC, external cortex of the inferior colliculus; nBIC, nucleus of the brachium of the inferior colliculus.

### 3.3.2 PUTATIVE PV NEURONS IN THE nBIC/ECIC PROVIDE DIRECT INHIBITION BUT ALSO EXCITATORY SYNAPTIC CONNECTION TO THE SGP

Because the retrograde tracing experiments pointed out an anatomical connection of PV neurons in the nBIC/ECIC with the SGP layer of the mouse SC, I wanted to see whether these connections could also be confirmed physiologically. For this purpose, an AAV with a Cre-dependent ChR2.tdTomato vector was injected bilaterally into the nBIC/ECIC of the PV<sup>cre</sup> transgenic mouse line (B6.129P2-Pvalbtm1 (cre)Arbr/J, N = 2). In this mouse line, only the PV positive neurons should produce Cre recombinase. Therefore, although the



injected AAV is not neuron-type-specific, the Cre-dependence should confine ChR2.tdTomato expression exclusively to PV neurons.

The tdTomato signal was readily visible at the injection site (Fig. 3.16A, left hemisphere shown) and in the cytoplasm of the nBIC/ECIC neurons (Fig. 3.16B). Furthermore, these putative PV neurons seemed concentrated within the region corresponding to the ECIC (compare with Fig. 3.15 Middle and Rostral). Importantly, tdTomato filled axonal nerve endings in the SGP of the SC (Fig. 3.16C) were also observed. These projections can be furthermore seen in abundance in Figure 3.16A, top. Very few of the projections into the SGP take a dorsal turn and produce additional nerve endings in the SGI (Fig. 3.16A and C, top, arrows).

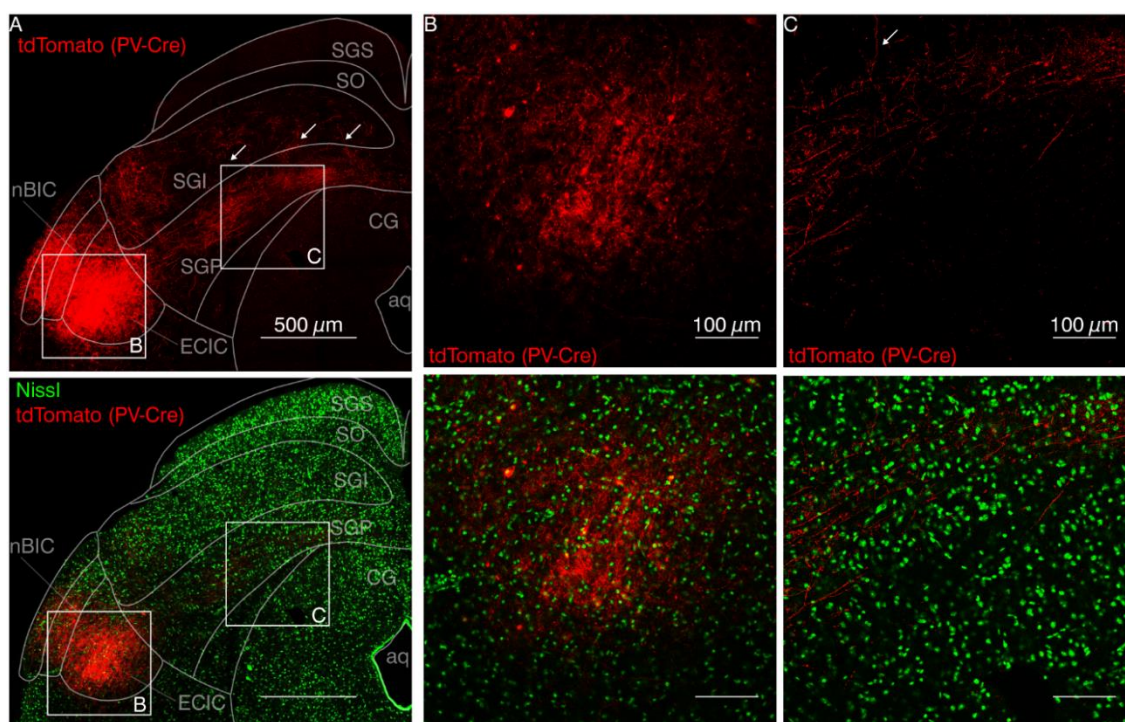


**Figure 3.16** Histological investigation of tdTomato positivity after the injection of Flex.ChR2.tdTomato into PVcre! mouse line

A–C, Confocal images of a mouse brain slice showing tdTomato fluorescence signal (top) and its overlay with Nissl staining (bottom) in the nBIC/ECIC and the SC. Regions within the white squares are shown magnified in (B) and (C). Arrows in the top image point towards axons projecting into the SGI. SGS,

stratum griseum superficiale; SO, stratum opticum; SGI, stratum griseum intermediale; SGP, stratum griseum profundum; CG, central grey; aq, aqueduct; ECIC, external cortex of the inferior colliculus; nBIC, nucleus of the brachium of the inferior colliculus.

Taken that an anatomical projection of the nBIC/ECIC PV neurons with the SGP using the PV<sup>cre</sup> mouse line was present, I wanted to determine whether there was a physiological connection between these structures and what its nature was. Three weeks after the injections, acute coronal brain slices of the SC were prepared. Recordings from SGP neurons with optical activation of the ChR2 in the axons of the putative PV nBIC/ECIC neurons were performed. Recordings were acquired from sixteen SGP neurons, out of which only five had any detectable optically-induced synaptic currents, indicating that this PV projection to the SC was relatively sparse (compared to the experiments where optically-induced currents were present in all SGP neurons recorded, Results 3.2). Surprisingly, I not only found inhibitory synaptic inputs but also excitatory inputs that the putative PV neurons in the nBIC/ECIC sent to the SGP.

The recordings from one SGP neuron with optically-induced direct inhibitory synaptic currents are presented in Figure 3.17. As shown in Figure 3.17B, top, there were no detectable EPSCs recorded in this SGP neuron, while a number of IPSCs were induced by stimulation of the dorso-lateral edge of the grid (Fig. 3.17B, bottom left) which were monosynaptic (Fig. 3.17B, bottom right). The individual traces from the stimulation locations 1 and 2 show that the amplitudes can be variable (Fig. 3.17C-D). Such recordings, however, were rare.



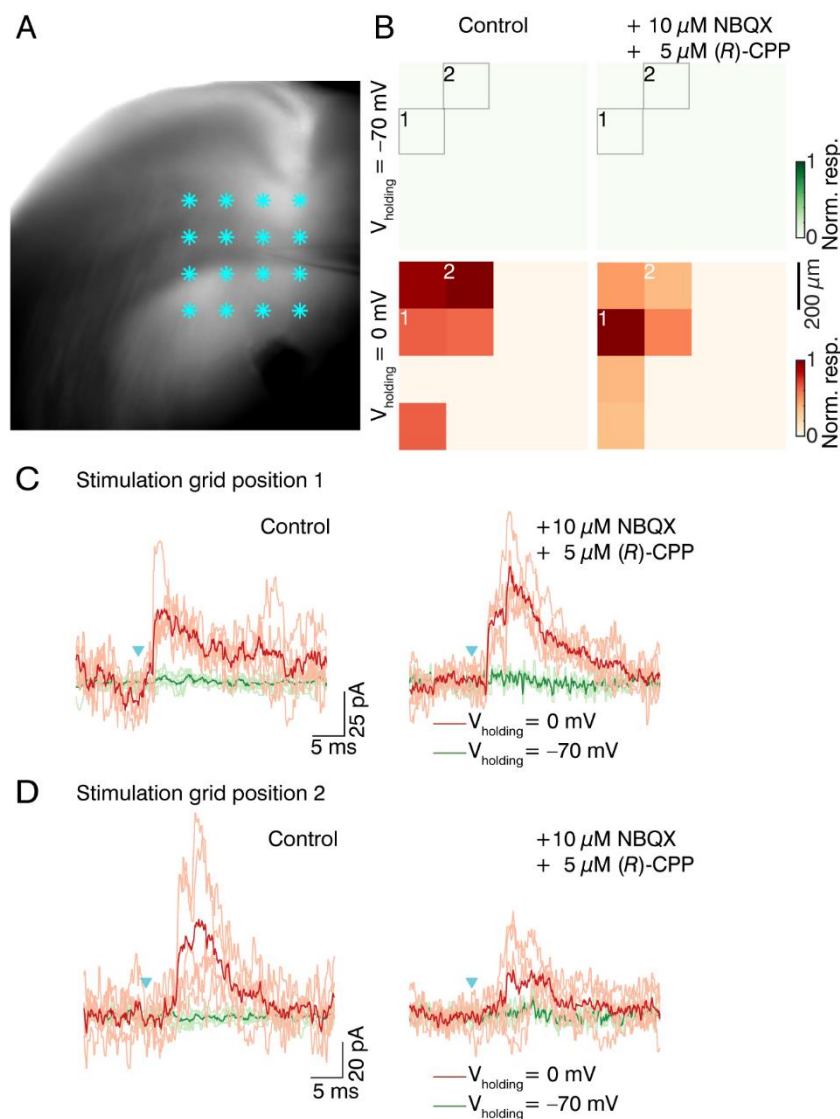


**Figure 3.17 Postsynaptic voltage-clamp recording of PV optical activation in a SGP neuron number 1, showing PV-mediated inhibition only**

**A**, Dot-grating image showing the SC brain slice with a recording electrode and positions of laser stimulation (cyan asterisks). **B**, Excitatory (top) and inhibitory (bottom) heat input maps constructed from peaks of the averaged EPSC and IPSC traces recorded in the SGP neuron upon laser stimulation at one of the 16 locations (shown in **A**). The maps were repeated in the presence of the drugs (right panels). The laser intensity was kept constant for all conditions. For the indicated positions 1 and 2, the EPSC and IPSC traces are shown in **C** and **D**, respectively. **C–D**, The EPSCs and the IPSCs recorded with the laser at the position 1 (**C**) and 2 (**D**) in control condition (left) and the drugs wash-in conditions (right). Lighter traces are single trials, darker traces are the averages. Cyan triangles represent the laser onset.

Another example recording of a single SGP neuron is shown in Figure 3.18. The stimulation grid was positioned in the vicinity of the SGP neuron recorded from in order to optically activate the presynaptic axons of the putative nBIC/ECIC PV neurons (Fig. 3.18A). Interestingly, with  $V_{\text{holding}} = -70$  mV, large EPSCs were obtained reliably from three positions (Fig. 3.18B). A plot of the largest EPSC (Fig. 3.18C) revealed a synaptic delay of  $2.7 \pm 0.0$  ms, suggestive of a monosynaptic connection. The excitatory heat input map (Fig. 3.18D) summarizes the locations of the EPSCs recorded. Although the recording for this neuron was done at  $V_{\text{holding}} = 0$  mV to test for IPSCs, there were no detectable currents at this holding potential (Fig. 3.18B, red traces). Two more SGP neurons were recorded with similar excitatory inputs and no inhibitory inputs (data not shown).

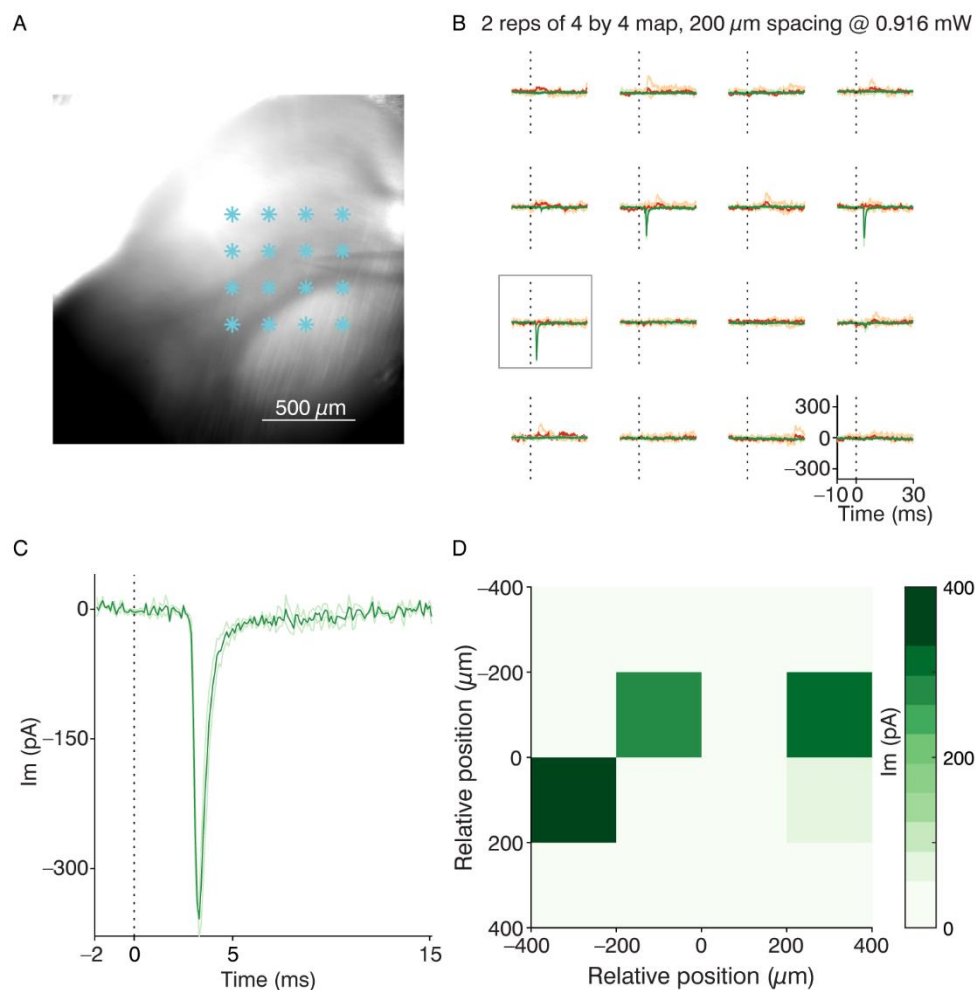


**Figure 3.18 Postsynaptic voltage-clamp recording of PV optical activation in a SGP neuron number 2, showing PV-mediated excitation only**

**A**, Dot-gradient image showing the SC brain slice with a recording electrode and positions of laser stimulation (cyan asterisks). **B**, Excitatory and inhibitory voltage-clamp recordings ( $V_{\text{holding}} = -70\ \text{mV}$ ,  $V_{\text{holding}} = 0\ \text{mV}$  respectively) with EPSCs and IPSCs induced by laser stimulation at one of the 16 positions. Lighter traces are single trials, darker traces are averages. Dotted lines represent the laser onset. The excitatory traces in the grey box are shown in **C**. **C**, Voltage-clamp traces of the largest EPSC recorded for this particular SGP neuron. Lighter traces are single trials, darker traces are the averages. Dotted lines represent the laser onset. **D**, Excitatory input map constructed from peaks of the averaged EPSC traces recorded in the SGP neuron upon laser stimulation at one of the 16 locations (shown in **A**).

Another example recording of a single SGP neuron is shown in Figure 3.19. This SGP neuron was recorded in the right SC hemisphere (Fig. 3.19A), unlike most of the previous recordings. Both excitatory and inhibitory maps in the control condition were recorded for this SGP neuron (Fig. 3.19B, left) and the inhibitory maps were repeated in the presence of the NBQX and (*R*)-CPP (Fig. 3.19B, right). The individual EPSC and IPSC traces for two laser grid positions are plotted in C and D. The recorded EPSC had a latency of  $3.0 \pm 0.2$  ms for the grid position 1 (Fig. 3.19C, left green traces). At the same position, there was an IPSC with an inward current preceding it (Fig. 3.19C, left red traces), suggestive of polysynaptically-mediated inhibition. Because the IPSC persisted when the drugs were in the bath (Fig. 3.19C, right red traces) with nearly no latency or amplitude differences (mean  $\pm$  SD latency control vs. drugs  $3.4 \pm 0.5$  ms vs.  $4.1 \pm 0.2$  ms; mean  $\pm$  SD amplitude control vs. drugs,  $52.9 \pm 28.8$  pA vs.  $60.7 \pm 15.3$  pA,  $p = 0.51$  Kruskal–Wallis test on amplitudes), this inhibition was direct inhibition-dominated. On the other hand, at the stimulation location 2 of the grid, the amplitude of the IPSC in the control condition versus drugs condition decreased (Fig. 3.19D, right red traces, mean  $\pm$  SD amplitude control vs. drugs,  $67.3 \pm 46.2$  pA vs.  $30.6 \pm 16.8$  pA), suggesting that the inhibitory current recorded from this location was a polysynaptic containing connection rather than direct inhibition-dominated. The statistical tests on the amplitudes however, showed nonsignificant result ( $p = 0.28$  Kruskal–Wallis test on amplitudes), concluding that the IPSC recorded at position 2 was also direct inhibition-dominated.

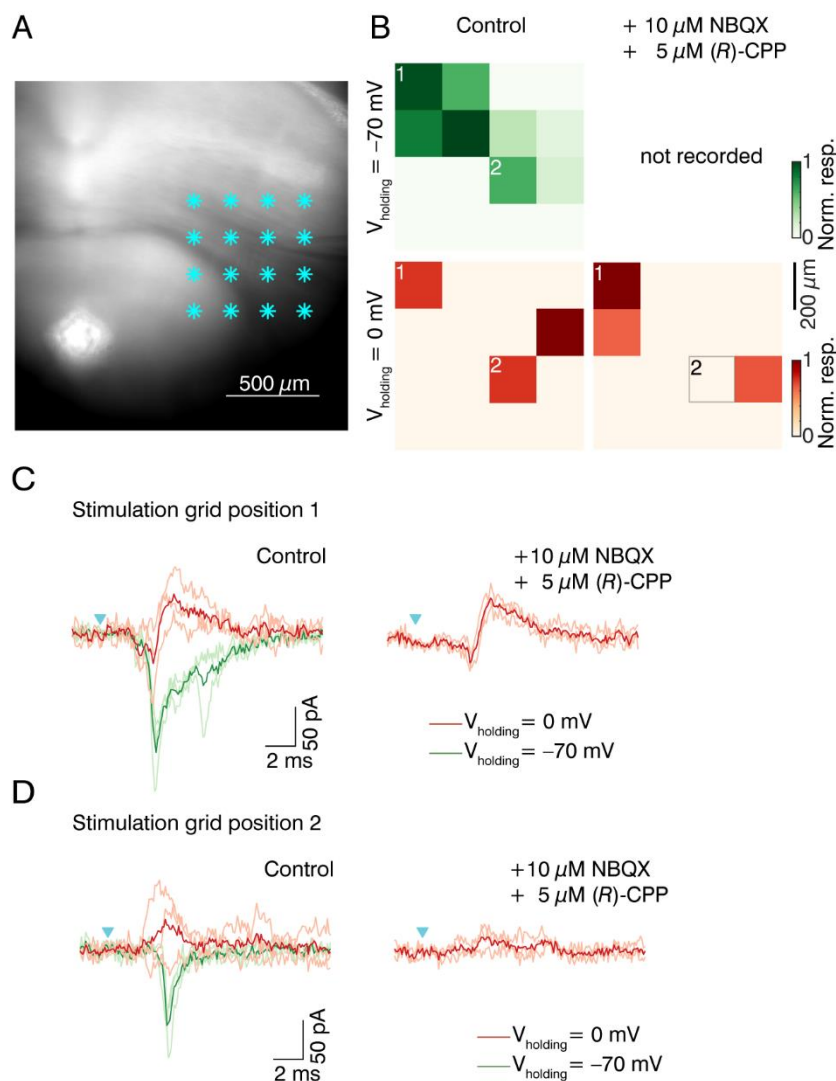


**Figure 3.19 Postsynaptic voltage-clamp recording of PV optical activation in a SGP neuron number 3, showing PV-mediated excitation and inhibition**

**A**, Dot-gradient image showing the SC brain slice with a recording electrode and positions of laser stimulation (cyan asterisks). **B**, Excitatory (top) and inhibitory (bottom) heat input maps constructed from peaks of the averaged EPSC and IPSC traces recorded in the SGP neuron upon laser stimulation at one of the 16 locations (shown in **A**). The maps were repeated in the presence of the drugs (right panels). For the indicated positions 1 and 2, the EPSC and IPSC traces are shown in **(C)** and **(D)**, respectively. Note that the excitatory map in the drugs condition was not acquired. **C–D**, The EPSCs and the IPSCs recorded with the laser at the position 1 (**C**) and 2 (**D**) in the control condition (left) and drugs wash-in condition (right). Lighter traces are single trials, darker traces are the averages. Cyan triangles represent the laser onset.

### 3.3.3 THE PVcre! MOUSE LINE DOES NOT DRIVE EXPRESSION IN AN EXCLUSIVE POPULATION OF PV NEURONS IN THE nBIC/ECIC

While the retrograde tracing experiments (Subsection 3.2.9) pointed towards the inhibitory SGP-projecting neurons in the nBIC/ECIC to be predominantly expressing PV, the results of the physiological experiments using PVcre! mouse line (Subsection 3.3.2) revealed both monosynaptic excitatory and inhibitory connections. Therefore, I performed immunohistological staining on one of the Flex.ChR2.tdTomato + PVcre! mice (N = 1 mouse) to confirm that the putative PV neurons in the nBIC/ECIC were indeed PV positive and whether they were inhibitory. Here, I counted the number of neurons in the nBIC/ECIC that showed as tdTomato positive and their immunoreactivity for PV antibody (Fig. 3.20) or GAD67 (Fig. 3.21). Out of 245 tdTomato nBIC/ECIC neurons, only 158 were positive for PV (65%, Table 7). Moreover, out of 65 tdTomato nBIC/ECIC neurons, only 35 were also positive for GAD67 (54%, Table 8). These data together suggest that in the PVcre! mouse line, there were non-PV neurons that expressed Cre recombinase or that over the course of the mouse development the PV-expression changed. Because there were discrepancies in the positivity of tdTomato neurons both for PV antibody and for GAD67 antibody, the possibility of errors due to histological preparation and staining (i.e. not sufficient fixation of PV/GAD67 in the neurons or antibody specificity issues) can be excluded. Considering that the retrograde tracing experiments showed at least 85% of SGP-projecting PV neurons to be inhibitory (17/20 in nBIC, 44/61 for ECIC, Table 6), these data indicate that the PVcre! line drives expression in a non-exclusive population of neurons in the nBIC/ECIC.

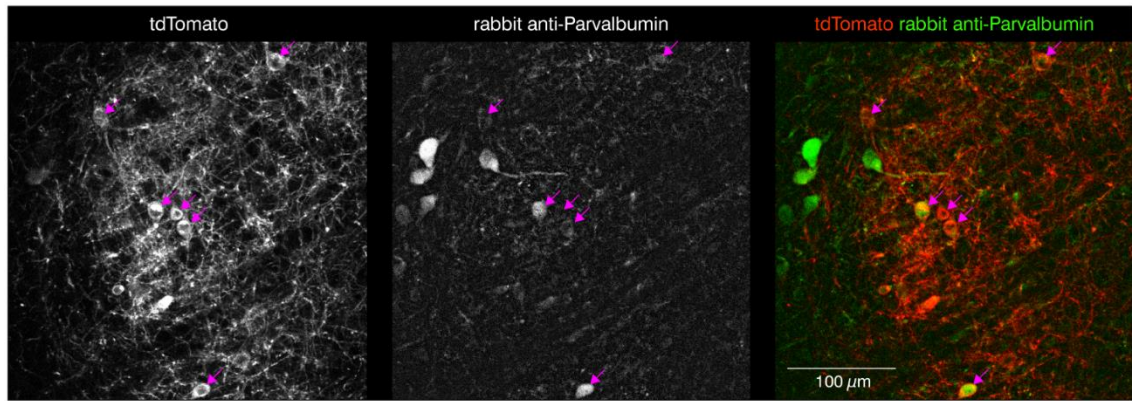


**Figure 3.20 tdTomato positive nBIC/ECIC neurons and their colocalization with PV antibody**

Example of a region within the ECIC in which the neurons and their positivity for PV was counted. Magenta arrows point towards tdTomato neurons within the example region which were tested for positivity for anti-PV.

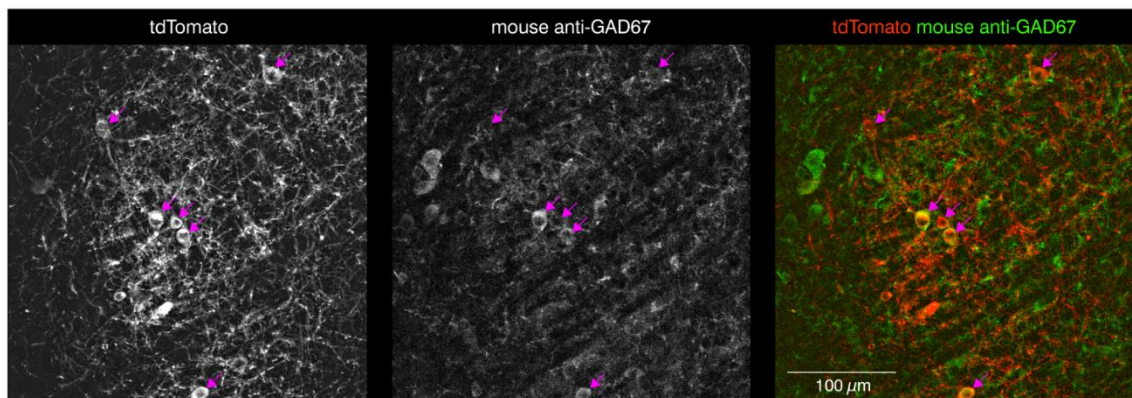


**Figure 3.21 tdTomato positive nBIC/ECIC neurons and their colocalization with GAD67 antibody**

Example of a region within the ECIC in which the neurons and their positivity for GAD67 was counted. Magenta arrows highlight tdTomato neurons within the example region which were tested for positivity for anti-GAD67.

**Table 7** | Number and percentage of tdTomato and PV positive nBIC/ECIC neurons

	tdTomato+	tdTomato + PV+
Overall count	245	158
% positive	100%	64.5%

N = 1

n = 36 tiles of nBIC/ECIC

**Table 8** | Number and percentage of tdTomato and GAD67 positive nBIC/ECIC neurons

	tdTomato+	tdTomato + GAD67+
Overall count	65	35
% positive	100%	53.9%

N = 1

n = 12 tiles of nBIC and ECIC

### 3.3.4 CONCLUSION

In this part of the thesis, I investigated the connectivity of PV neurons in the nBIC/ECIC with neurons residing in the SGP of the mouse SC. Histological analysis of this connectivity indicated that the direct inhibitory projection described in Results 3.2 could partially be PV-mediated (Table 6). Functional connectivity of PV nBIC/ECIC neurons and the SGP neurons was found to be inhibitory (Fig. 3.17) as would be predicted by the initial hypothesis. But, many excitatory connections were also recorded. Furthermore, the finding that only 65 % of putative PV neurons in the nBIC/ECIC were indeed PV positive together with the finding that only 53 % of those were inhibitory, raised questions over the validity of the PVcre! mouse line functional data. Thus, with the above-mentioned experiments, the hypothesis that the direct inhibitory connection to the SGP is provided by PV neurons in the nBIC/ECIC could not be confirmed.



### 3.4 MULTISENSORY INTEGRATION IN THE SGI

To study the integration of multisensory inputs in the SC, I established an *in vitro* preparation in which the visual and the auditory/multisensory inputs can be activated separately. Here, I prepared slices from one of the AAV.ChR2.eYFP injected animals according to the same protocol as described in Subsection 3.2.4. Thus, I gained the access to optical activation of the nBIC/ECIC axons, thereby activating the auditory/multisensory pathway. In addition, I have also assembled an electrical stimulation of the SGS layer of the mouse SC, thereby activating the visual pathway. An example recording of a neuron residing in the SGI layer with the stimulation paradigm is shown in Figure 3.22, left. The EPSCs were recorded at  $V_{\text{holding}} = -70$  mV upon different stimulation configurations (Fig. 3.22, recording traces). In Auditory/multisensory only condition, only laser stimulation was performed. In Auditory/multisensory + Visual 10 ms before condition, the electrical stimulation to the SGS preceded by 10 ms the laser stimulation. In Auditory/multisensory + Visual same time condition, the electrical stimulation to SGS was performed at the same time as the laser stimulation. Visual assessment of the traces suggests that when both modalities are stimulated at the same time, the currents they produce sum relatively linearly, a finding in line with previous evidence (Skaliora *et al.*, 2004), although with only electrical stimulation. It would however be interesting to see what happens in the current-clamp condition to the summed spikes that the modalities produce, and how the blocking of GABAergic receptors affects the summation.

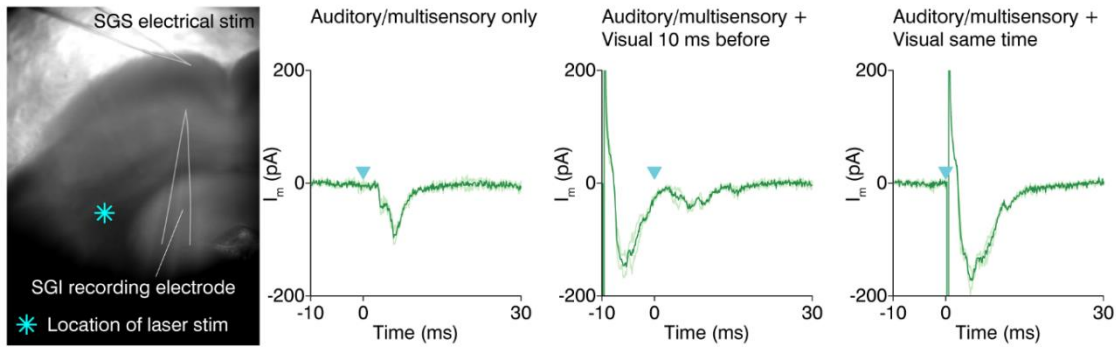


**Figure 3.22 Example SGI recording of auditory/multisensory and visual stimulation**

Dot contrast image showing the configuration of stimulation and recording (left). An electrode was placed in the SGS for electrical stimulation of the visual pathway. Cyan asterisk shows laser stimulation of ChR2 in the incoming nBIC/ECIC axons. The location of the recording electrode in the SGI is outlined for orientation. The recorded traces and their respective conditions, are shown. Cyan triangles show the laser onset. Individual repetitions are shown as lighter traces and darker traces are the averages.

Although the recordings presented in Figure 3.22 are only an example of a single SGI cell recording, it shows that in principle, such stimulation configuration would be feasible. Thus, this data work as a proof-of-principle that such methodological approaches can be used to study the integration of visual and auditory/multisensory inputs in the mouse SC.

---

## DISCUSSION

---

In this study, I characterized the electrophysiological profiles of neurons in the SGP layer of the SC in the mouse and the types of inputs they receive from the nBIC/ECIC. Electrophysiological and morphological profiling showed at least three types of neurons in the SGP consistent with types found in other SC layers. Surprisingly, each type of SGP neuron recorded from received a direct inhibitory connection in addition to a direct excitatory input. The excitation in some neurons drove feed-forward inhibition. I demonstrated the existence of distinct axonal trajectories from the nBIC/ECIC to the SGP, corroborated by my own histological evidence supporting a difference in the locations of the excitatory and inhibitory projection neuron somas within the nBIC/ECIC. Lastly, the direct inhibitory projection from nBIC/ECIC is mediated predominantly by parvalbumin-expressing neurons.

### 4.1 CELL TYPES WITHIN THE SGP

While the SC of the mouse contains three distinguishable granular layers (SGS, SGI, SGP), most of the previous literature focused on the SGS and SGI and not the SGP. As it is unclear whether the SGP is purely sensory (like the SGS) or multisensory/premotor (like the SGI), comparisons with the SGS/SGI literature are relevant. Previous work from the Isa laboratory has described at least six electrophysiologically distinct classes of neurons in the SGI (Saito & Isa, 1999), three out of which were also found in the SGP (late-spiking, spike-adapting, and fast-spiking). On the other hand, I did not encounter any burst-spiking or rapid-spike inactivation neurons in the SGP of the mouse SC, which could reflect the developmental stage of the animals I recorded from. The majority of GABAergic neurons in the SGI was identified to be fast-spiking (Sooksawate *et al.*, 2011),

indicating that the fast-spiking neurons in the SGP could also be part of the intra- and interlaminar inhibitory SC circuitry. In addition, it has been postulated that the large multipolar regular-spiking neurons in the SGI serve the major motor output of the SC (Sooksawate *et al.*, 2005). Anatomical studies have previously shown some multipolar neurons present in the SGP of the SC in the cat (Moschovakis & Karabelas, 1985), although it is unknown whether these neurons also project out of the SC. While I did not observe a cluster of regular-spiking neurons in the SGP of the mouse SC, the possibility that a small population of these neurons also exists in the SGP cannot be excluded.

#### **4.2 INPUT CIRCUITRY FROM THE nBIC/ECIC TO THE SGP**

An anatomical examination of the connections between the nBIC/ECIC and the SC has been performed in a number of species (Druga & Syka, 1984; Covey *et al.*, 1987; Jiang *et al.*, 1997; King *et al.*, 1998; Lesicko & Llano, 2018; Mellott *et al.*, 2018)(Druga & Syka, 1984; Covey *et al.*, 1987; Jiang *et al.*, 1997; King *et al.*, 1998; Lesicko & Llano, 2018; Mellott *et al.*, 2018). By injecting an AAV.ChR2.eYFP into the nBIC/ECIC and then imaging the eYFP signal in fixed SC slices, I also confirmed the anatomical projection from these auditory structures of the IC into the SGP layer of the SC in the mouse (Fig. 3.4, injection site in nBIC/ECIC and axons in the inset).

Electrical stimulation of the rat nBIC/ECIC showed an excitatory connection in the SGI (Skaliora *et al.*, 2004). The experimental paradigm presented in this thesis, which combines presynaptic activation of the nBIC/ECIC with simultaneous recordings in the SGP, extends these findings. While the presence of an excitatory connection was confirmed as described in the rat, I additionally described a mixed polysynaptic and monosynaptic inhibition in this

circuit (Fig. 4.1). The presence of the polysynaptic inhibition is perhaps not surprising as feed-forward inhibition is a common feature of input circuitry in many brain areas and was also described in the superficial and intermediate SC layers (Saito & Isa, 2003; Kardamakis *et al.*, 2015). It is likely performed by the fast-spiking population of neurons in the SGP, as they are known to be GABAergic in the SGI (Sooksawate *et al.*, 2011), but further experiments are required to address this question specifically (Fig. 4.1, dashed inhibitory synaptic connection in the SGP).

GABAergic projections from auditory structures to the SC have been described to originate in the ECIC of the cat (Appell & Behan, 1990) and in the nBIC of the guinea pig (Mellott *et al.*, 2018), but in both cases the percentages of GABAergic neurons was rather small (only 10% in Mellott *et al.* (2018)), and the studies therefore concluded that the contribution of direct inhibition to sensory processing in the SC was probably minor. Although the tracing data in Subsection 3.2.8 indicates comparably small percentages, I found that 100% of all SGP neurons recorded from had direct inhibitory inputs. Thus, although only few inhibitory neurons in the nBIC/ECIC project directly to the SGP, their axonal arbours must diverge massively to contact most, if not all neurons located in the medial part of the SGP of the mouse SC. Therefore, the functional implication of direct inhibition to the SGP is more substantial than previously thought (Fig. 4.1, dashed inhibitory axonal collateral of the inhibitory neuron).

The findings presented in this thesis furthermore show that the majority of the nBIC/ECIC GABAergic cells also co-localize with PV and to a very small extent with calbindin, while somatostatin was not detected at all in this region. Thus, identifying these inhibitory projection neurons revealed a PV positive subpopulation. Recently, PV positivity was investigated in the SGS and the SGI of the mouse SC (Villalobos *et al.*, 2018). In the SGI, high percentage of PV neurons also co-labelled with GAD67, while in the SGS this was about 40%. Interestingly,

a recently published article has presented a PV positive excitatory pathway from the SGS to PBg which, when activated, triggered various behaviours (fear responses, conditioned aversion, and depression-related behaviours) (Shang *et al.*, 2015). Thus, the PV neurons in the midbrain and the networks they mediate have more varied functions compared to those in the cortex, where PV positivity is usually related to local inhibitory neurons (for review see Hu *et al.* (2014)). Future experiments can target these projections in a cell-type specific manner for understanding the function of this direct inhibitory PV positive projection in the auditory circuit of the mouse SC.

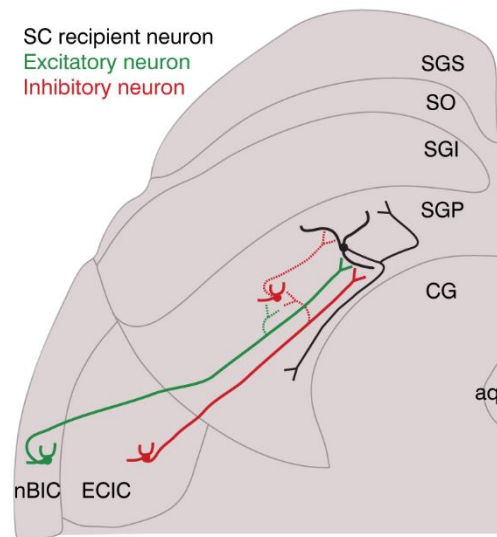


**Figure 4.1 Proposed scheme of the nBIC/ECIC projections into the mouse SC**

In addition to a direct excitatory projection from the nBIC (green excitatory neuron) to the SGP-residing neuron (black), a direct inhibitory connection originating in the ECIC (red inhibitory neuron) is also present. Secondly, a feed-forward inhibitory connection is mediated by an axonal branch of the direct excitation (dashed green synapse) possibly involving an SGP-residing inhibitory interneuron (dashed inhibitory connection within the SGP). Thirdly, a direct inhibitory synapse (dashed red synapse) onto an SGP-residing inhibitory interneuron. Dashed synapses are only proposed. Note that the excitatory projection from the ECIC is not shown, and the inhibitory ECIC neuron presumably has more axonal collaterals than shown. SGS, stratum griseum

superficiales; SO, stratum opticum; SGI, stratum griseum intermediale; SGP, stratum griseum profundum; CG, central grey; aq, aqueduct; ECIC, external cortex of the inferior colliculus; nBIC, nucleus of the brachium of the inferior colliculus.

#### **4.3 SPATIALLY DISTINCT EXCITATORY AND INHIBITORY INPUTS FROM THE nBIC/ECIC TO THE SGP**

A particularly striking finding was the apparent difference in the mediolateral distribution between monosynaptic excitatory and inhibitory inputs from the nBIC/ECIC to the SGP. ChR2-assisted circuit mapping experiments revealed that at least inhibitory axon trajectories are relatively concentrated to the medial side. Retrograde tracing and immunohistochemical analysis further confirmed that the inhibitory projection cell bodies are also concentrated toward the medial side within the nBIC/ECIC. Because the ECIC is located slightly caudally to the nBIC, and because the nBIC/ECIC are generally caudal to the SGP neurons to which they project (Franklin & George, 2007), it is possible that the medial bias of axon trajectories in the slices reflects the medially projecting ECIC axons as they traverse rostrally through the slices recorded from. This led me to conclude that the direct inhibitory input originates predominantly in the ECIC, whereas the excitatory inputs arise from both the nBIC and the ECIC. It should however be noted that due to the strict distance requirement between the stimulation and the recording ( $>400\ \mu\text{m}$ ), recordings for these experiments were restricted to the medial part of the SGP, and these interpretations may not fully generalize to the lateral segments of the SGP.

Another possible source of auditory inputs to the SC is the rostral pole of the IC (rpIC), as an anatomical projection from the rpIC has been characterized in the cat (Harting & Van Lieshout, 2000). Although the rpIC has been anatomically delineated in a Golgi study of the mouse (Meininger *et al.*, 1986), its

projections to the SC have not been characterized. Further investigations into the anatomical borders between the nBIC, the ECIC, and the rpIC, for example by single neuron tracing, will be necessary to disentangle the contribution of each of their projections to the SC.

#### **4.4 FUNCTIONAL IMPLICATIONS OF A DIRECT INHIBITORY nBIC/ECIC INPUT TO THE SC**

While it is generally accepted that feed-forward inhibition enforces a precise time window during which the postsynaptic neuron can be excited, the direct, long-range inhibitory projection described here enriches the patterning of input activity to the SGP. The fact that relatively few inhibitory neurons from the nBIC/ECIC project to most, if not all neurons in the medial SGP (the region I recorded from), indicates a broader divergence of these inputs compared to their excitatory counterparts. Interestingly, the nBIC/ECIC comprises GAD67 positive neurochemical modules, which are thought to receive axonal terminations predominantly from somatosensory structures (from the somatosensory cortex and the dorsal column nuclei), while the auditory inputs (from the auditory cortex and the ICC) terminate in the extramodular zones (Lesicko *et al.*, 2016). Furthermore, a recent study identified an excitatory auditory pathway from the ECIC extramodular zones to reach the SC in the mouse (Lesicko & Llano, 2018). Thus, the direct inhibitory inputs I recorded in the SGP may carry a mix of auditory, somatosensory, or even multisensory information, while the excitatory/feed-forward inhibitory inputs are predominantly auditory in nature. It is tempting to speculate that the larger divergence of the direct inhibitory inputs underlies a specific coding strategy the SGP employs to interpret its sensory inputs. For example, it is known that the nBIC contains multiple classes of spatially tuned auditory responsive neurons that do not necessarily mirror those found in the SC (Schnupp & King, 1997). It is therefore possible that the SC



refines its spatial tuning by drawing from the diversity of excitatory and inhibitory inputs from the nBIC/ECIC. Future *in vivo* studies of this complex circuitry thus have promise to disentangle the functional implications of its individual components for sensory integration and multimodal processing in the SC.

In a broader perspective, how could this complex auditory/somatosensory circuitry deal with eye movements that most mammals do? It is very well known that the barn owls do not make any eye movements, making the head and the eyes coordinates always in register with each other. Thus, aligned maps of visual and auditory space in the optic tectum are understandable. For most mammals however, any movement of either the head or the eyes independent of each other misaligns the register for the auditory (head-centred) and the visual (eye-centred) visual representations. For example, when looking to the front and the head is oriented also towards front, the eyes and the head coordinates are in register with each other. However, movement of the eyes with no movement of the head creates a misalignment to the head-centred coordinates. Similarly, movement of the head with no movement of the eyes creates a vice versa misalignment. It is entirely unclear how the SC circuitry produces the described maps of auditory space in register with the visual despite such shifts and misalignments and mammals.

Therefore, I put into question the robustness of the described auditory spatial maps in lower mammals. The data in these experiments were collected using multiunit recordings, where it is difficult to interpret how individual neurons respond. Furthermore, in the primates where there are single-cell SC recordings, the data shows a hybrid frame of reference (Maier & Groh, 2009). Here, the auditory representation is guided by a saccade production but otherwise there is no map-like auditory representation. Therefore, either the primates are an exception, or the issue of aligning the frames of reference of

auditory and visual system should be revisited in the SC of lower mammals with single-cell *in vivo* recordings.

Moreover, the complexity of frames of reference is further exacerbated by the fact that some mammals in addition to eye movements also perform ear movements. Directing the ears towards sound sources of interest was found to be mediated by the SC (Stein & Clamann, 1981). Two anatomical pathways for SC pinnae control have been found. First, a disynaptic pathway through the paralemniscal zone to motoneurons in the facial nucleus was suggested to be responsible for independent pinnae movements (Henkel, 1981). Second, also a disynaptic pathway through the pontine reticular formation to the motoneurons of the facial nucleus was suggested to coordinate movements of the pinna, eyes, and the head together (Grantyn *et al.*, 1987; May *et al.*, 1990). It would be interesting to see how the SC merges the disparate frames of reference to orient the head, the eyes, and the pinnae towards salient objects in space.

#### **4.5 METHODOLOGICAL LIMITATIONS**

ChR2-assisted circuit mapping is a method that was initially used in the neocortex with the purpose of mapping inter- and intra-laminar connections. In comparison to presynaptic stimulation by electric current, which requires the knowledge of anatomical connections, ChR2-assisted circuit mapping allows localizing presynaptic connections. Here, the cell body and the axons containing ChR2 in their membranes can be focally activated. While this is a powerful tool in modern neuroscience, it comes with some limitations. Firstly, activation of ChR2 in the soma and the axon produces identical postsynaptic currents, making the locations of the soma/axons indistinguishable from each other. Secondly, during the slicing process, the soma can become detached from its corresponding axon if they do not lie within the same slicing plane. Despite this, the activation

of ChR2 in the axon is possible in the slice and has been reported. Therefore, in this thesis, the interpretation of the results of ChR2-assisted circuit mapping in the nBIC/ECIC to SGP circuit has been made only in terms of the axons locations and not the somas (Subsections 3.2.4 and 3.2.6). In order to locate the presynaptic somas of SGP neurons in the nBIC/ECIC, I implemented two methodological strategies (Subsections 3.2.7 and 3.2.8). The physiological approach using a modified ChR2 construct with a Kv2.1 targeting motif has proven in my hands to be unsuccessful, because ChR2 was not exclusively expressed in the somas of transduced cells. Thus, the genetic strategy could not provide physiological evidence that the locations of SC-projecting neuron somas reflect the differences in the locations of inhibitory and excitatory axons in the nBIC/ECIC. However, the second strategy implementing retrograde tracing combined with immunostaining for GAD67 and calretinin provided at least anatomical evidence that the locations of somas within the nBIC/ECIC correspond to the differences between excitatory and inhibitory axonal projections to the SC.

An alternative strategy that has not been tested in this PhD thesis utilizes laser-scanning photostimulation (LSPS, Katz & Dalva, 1994; Shepherd, 2012). Using this method, laser-uncaging of glutamate at the nBIC/ECIC somas and dendrites produces APs, which propagate towards the SC. Because there are seldom any glutamate receptors on axons, the PSCs recorded at the SGP neurons evoked by laser stimulation at a particular location in the slice would indicate the presence of presynaptic neuron somas in that area. In this way, the experimenter would have the information about the location of the presynaptic somas in the nBIC/ECIC and also the nature of the synaptic contact, as this method is compatible with the voltage-clamp protocol utilized in this thesis to isolate excitatory and inhibitory connections in the same recording. Furthermore, the activation of the nBIC/ECIC neurons far (>400  $\mu\text{m}$ ) from the recording sites in the SGP, prevents direct dendritic activation of the recorded SGP neurons

themselves [a common issue of cortical LSPS circuit mapping (Shepherd, 2012)]. On the other hand, LSPS-based glutamate uncaging also has its limits. If the presynaptic neuron lies not in the slicing plane of the recorded postsynaptic neuron, the presynaptic axon and its soma get detached. Without the soma, the axons cannot be activated and thus some connections could be missed as a result of the slicing. Thus, while ChR2-assisted circuit mapping is a powerful method for locating the presynaptic axons and characterizing their connectivity with a postsynaptic neuron, LSPS-based glutamate uncaging provides a complementary approach to locate the presynaptic somas in the slice.

Another methodological limitation of the viral approach used in this thesis is neuronal specificity. The injection of AAV.ChR2.eYFP into the nBIC/ECIC transduced nBIC/ECIC neurons non-specifically. An alternative approach would be transsynaptic viral transduction combined with AAV.ChR2 delivery to a subpopulation of nBIC/ECIC neurons that receive inputs from somatosensory or auditory structures. For example, an injection of AAV.Cre into the spinal nucleus (Lesicko *et al.*, 2016) could provide Cre transsynaptically to the ECIC neurons within the GAD67 modules. The ECIC neurons within modules could then be infected with an AAV.ChR2 and their connectivity with the SGP (if it exists) could be probed specifically. Similarly, the auditory inputs of the extramodular ECIC could be injected with AAV.Cre and specifically their connectivity with the SGP could be studied. Such an approach has already been implemented to target specifically the corticotectal projections from the mouse primary auditory cortex to the SC (Zingg *et al.*, 2017). While in this publication the transsynaptic tagging was used to identify freezing/escape response circuits in the mouse, similar methodological approaches could be used in the nBIC/ECIC to scrutinize their inputs to the SGP. Furthermore, molecular specificity within the nBIC/ECIC could be utilized – parvalbumin positivity in the inhibitory ECIC neurons or calretinin positivity of extramodular ECIC neurons.

Yet another facet of methodological limitations concerns the use of transgenic animals, in the case of this thesis the PV<sup>cre</sup> mouse line. In this mouse line, all PV neurons should also express Cre recombinase. Therefore, an injection of an AAV.ChR2.tdTomato under Cre-dependent expression should label all PV neurons with tdTomato (and ChR2 to make them optically excitable). However, this exclusivity assumes no leakage of Cre expression to neurons not expressing PV. Because Cre antibodies have been until now unsuccessful to confirm the population of Cre-expressing neurons, despite recent efforts in the Bonhoeffer laboratory, results from any Cre-dependent viral transduction remain difficult to interpret. Indeed, the results of the PV-antibody immunohistology (Subsection 3.3.3) showed that 35% of the putative PV neurons did not express PV. It is currently unclear how such a discrepancy may arise, but it is clearly important to develop proper expression controls in transgenic animals if any scientific conclusions are to be drawn from datasets using such animals. Because the functions and the connectivity of PV neurons in the SC circuits seem to be diverse compared to those in the cortex, having a method to definitively confirm cell-specificity should be of foremost importance not just for this study, but also for all future studies involving Cre-dependent cell-specific expression.

#### **4.6 OUTLOOK AND FUTURE APPLICATIONS**

The main findings of this thesis are that neurons in the auditory-recipient SC layer receive previously underappreciated inhibition, which originates predominantly in the ECIC compared to the nBIC. In addition, there is an excitatory connection that originates from rather equivalent populations in both in the nBIC and the ECIC and to some extent drives feed-forward inhibitory networks in the auditory input layer of the SC.

I have speculated that the excitatory and inhibitory inputs in the ECIC may provide both auditory and somatosensory information to the SC. Because the ECIC contains molecularly defined modular and extramodular zones, their connectivity with the SC could be tested in a more specific fashion. For example, it would be interesting to see whether the calretinin neurons in the extramodular ECIC indeed provide the excitatory input to the SC. Along these lines, it should be confirmed whether the PV neurons located within the ECIC modules provide the SC with monosynaptic inhibition. If these two pathways do exist, it would be very interesting to see whether they also have distinct roles in audio-somatosensory processing and what the nature of their inputs is. A set of *in vivo* experiments could be carried out with stimulation of the mouse vibrissae alone or in a combination with an auditory stimulus. Here, recordings from the modular and the extramodular ECIC would lay groundwork for how separate or multisensory these two pathways are.

Although excitatory inputs to the SGP originate both in the nBIC and the ECIC, because of the presence of the modules/extramodules in the ECIC, perhaps those specific nBIC excitatory inputs are important for auditory coding. Excitation and feed-forward inhibition are believed to provide a window-of-opportunity in which the excitation carries information about an event, excites the postsynaptic partner and then the lagging inhibition abruptly terminates the excitation. In this way, the same brain circuit could detect fast successive events. A way of testing whether such mechanisms are at play in the auditory circuit of the SC could be by a combination of *in vivo* behavioural experiments with some perturbation. For example, the activity of SGP neurons could be recorded during a presentation of a sound stimulus and then during a presentation of a sound stimulus coupled with the infusion of GABA<sub>A</sub> receptors blocker into the SC. If the molecular identity of the local SC inhibitory neurons was known, the perturbation could be done in a cell-type specific manner, for example by using

optogenetics, however such manipulation would need to overcome many technical hurdles.

In general, the existence of direct inhibition in the nBIC/ECIC-SC circuit could have implications for the construction of the reported map of auditory space in small mammals. Firstly, the relationship between frequency tuning and spatial tuning of the SC neurons could be investigated *in vivo* by recording the activity of SGP neurons upon presentation of sounds (pure tones) from different azimuthal locations. Secondly, it would be interesting to see what the inactivation of the ECIC inhibition does to the tuning of the SC neurons.

Furthermore, *in vitro* experiments could be carried out to study the integration of auditory/multisensory with the visual inputs. Firstly, it would be interesting to see whether columnar-like organization present in the SGS-SGI circuit also exists for the auditory/multisensory circuits in the SC. This could be performed by single-cell SGI recordings coupled with presynaptic stimulation in the SGP along its latero-medial axis. If this is the case, recordings from SGI neurons combined with within column SGS stimulation (visual) and within column SGP stimulation (auditory/multisensory) could be performed. I have performed preliminary experiments in which the visual pathway was stimulated electrically and the auditory/multisensory pathway was stimulated optogenetically (Fig. 3.22). In terms of postsynaptic currents, the multimodal inputs summed linearly. This finding goes in line with previously reported *in vitro* study on multisensory integration (Skaliora *et al.*, 2004). The relevant questions here however, should be whether the stimulation of the multimodal inputs can induce spikes in the SGI neurons (or even bursting responses). Because we now know that the SGP neurons are under strong inhibitory influence from the ECIC (in addition to the SNr tonic inhibition of the SGI), it would be very interesting to see how the multimodal inputs summate once the very strong inhibition is blocked pharmacologically.

Moreover, prior to this thesis, anatomical tracing studies provided evidence for an inhibitory projection from the nBIC/ECIC to the SC. However, the number of such projections was very low (~10 % in Mellott *et al.*, 2018). Although the retrograde tracing results of this thesis showed similarly small numbers of inhibitory neurons in the nBIC/ECIC, the physiological experiments showed that the direct inhibition is extensive and that all SGP neurons do indeed receive it. Such findings lead to a hypothesis that the axonal arbours of the inhibitory nBIC/ECIC neurons are massive and contact multiple SGP neurons. There is however no evidence to support this hypothesis. Thus, single-cell nBIC/ECIC tracing should be performed to investigate this possibility.

Lastly, taking into account all that is still unknown about SC spatial coding (modality-specific codes, disparate frames of reference, and shifts that independent eyes/ears movements produce), future experiments could give more insights. Today it is possible to perform experiments in head-fixed and freely-moving animals, making it feasible to test how these spatial issues are resolved. For example, cutting one of the eye muscles could give us information into how spatial coding changes. In the head-fixed preparation, one could correlate the eye position with the auditory space alignment. In a freely-moving preparation, one could measure spatial auditory responses in an arena with multiple speakers. Thus, modern technologies promise to resolve outstanding questions regarding the spatial coding in the SC.

## **4.7 CONCLUSIONS**

In conclusion, this thesis characterized the circuits of auditory inputs in the SC of the mouse. Firstly, I confirmed that the auditory SC layer is populated by three distinguishable classes of neurons, which resemble types of neurons found in other SC layers. The nBIC/ECIC in the IC, that provide auditory inputs



to the SC, innervate most, if not all SGP neurons by a direct excitatory connection, as well as a direct inhibitory connection. This was a surprising finding considering the mere 15% of SC-projecting GABAergic neurons reported in the nBIC/ECIC in this thesis and 10% in Mellott *et al.* (2018). Channelrhodopsin-assisted circuit mapping and retrograde anatomical tracing further revealed distinct excitatory and inhibitory projection trajectories to the SGP and cell body distributions, suggesting a functional segregation between the direct excitatory and inhibitory inputs. Histological analysis furthermore indicated that the majority of the direct inhibitory neurons are parvalbumin positive.



## REFERENCES

- Aitkin LM, Kenyon CE & Philpott P (1981). The representation of the auditory and somatosensory systems in the external nucleus of the cat inferior colliculus. *J Comp Neurol* **196**, 25–40.
- Aitkin LM & Phillips SC (1984). The interconnections of the inferior colliculi through their commissure. *J Comp Neurol* **228**, 210–216.
- Albano J, Norton T & Hall WC (1979). LAMINAR ORIGIN OF PROJECTIONS FROM THE SUPERFICIAL LAYERS OF THE SUPERIOR COLLICULUS IN THE TREE SHREW, *TUPAIA GLIS*. *Brain Res* **173**, 1–11.
- Appell PP & Behan M (1990). Sources of subcortical GABAergic projections to the superior colliculus in the cat. *J Comp Neurol* **143**, 143–158.
- Baker CA, Elyada YM, Parra A & Bolton MML (2016). Cellular resolution circuit mapping with temporal-focused excitation of soma-targeted channelrhodopsin. *Elife* **5**, 1–15.
- Benedetti F (1991). The postnatal emergence of a functional somatosensory representation in the superior colliculus of the mouse. *Dev Brain Res* **60**, 51–57.
- Cajal RS (1888). Estructura de los centros nerviosos de las aves. *Rev Trimest Histol Norm y Patol* **1**, 1–10.
- Campbell RAA, Doubell TP, Nodal FR, Schnupp JWH & King AJ (2006). Interaural Timing Cues Do Not Contribute to the Map of Space in the Ferret Superior Colliculus: A Virtual Acoustic Space Study. *J Neurophysiol* **95**, 242–254.
- Carlile S & Pettigrew AG (1987). Distribution of frequency sensitivity in the superior colliculus of the guinea pig. *Hear Res* **31**, 123–136.

- Castro-Alamancos MA & Favero M (2016). Whisker-related afferents in superior colliculus. *J Neurophysiol* **115**, 2265–2279.
- Chevalier G & Mana S (2000). Honeycomb-like structure of the intermediate layers of the rat superior colliculus, with additional observations in several other mammals: AChE Patterning. *J Comp Neurol* **419**, 137–153.
- Coleman JR & Clerici WJ (1987). Sources of projections to subdivisions of the inferior colliculus in the rat. *J Comp Neurol* **262**, 215–226.
- Covey E, Hall WC & Kobler JB (1987). Subcortical connections of the superior colliculus in the mustache bat, *Pteronotus parnellii*. *J Comp Neurol* **263**, 179–197.
- Cusick CG & Kaas JH (1982). Retinal projections in adult and newborn grey squirrels. *Dev Brain Res* **4**, 275–284.
- Dillingham CH, Gay SM, Behrooz R & Gabriele ML (2017). Modular-extramodular organization in developing multisensory shell regions of the mouse inferior colliculus. *J Comp Neurol* **525**, 3742–3756.
- Doubell TP, Baron J, Skalióra I & King AJ (2000). Topographical projection from the superior colliculus to the nucleus of the brachium of the inferior colliculus in the ferret: Convergence of visual and auditory information. *Eur J Neurosci* **12**, 4290–4308.
- Drager UC & Hubel DH (1975). Physiology of visual cells in mouse superior colliculus and correlation with somatosensory and auditory input. *Nature* **253**, 203–204.
- Drager UC & Hubel DH (1976). Topography of visual and somatosensory projections to mouse superior colliculus. *J Neurophysiol* **39**, 91–101.
- Druga R & Syka J (1984). Projections from auditory structures to the superior

colliculus in the rat. *Neurosci Lett* **45**, 247–252.

Edwards SB, Ginsburgh CL, Henkel CK & Stein BE (1979). Source of subcortical projections to the superior colliculus in the cat. *J Comp Neurol* **184**, 309–330.

Edwards SB & Henkel CK (1978). Superior colliculus connections with the extraocular motor nuclei in the cat. *J Comp Neurol* **179**, 451–467.

Endo T, Tarusawa E, Notomi T, Kaneda K, Hirabayashi M, Shigemoto R & Isa T (2008). Dendritic  $I_h$  Ensures High-Fidelity Dendritic Spike Responses of Motion-Sensitive Neurons in Rat Superior Colliculus. *J Neurophysiol* **99**, 2066–2076.

Faye-Lund H & Osen KK (1985). Anatomy of the inferior colliculus in rat. *Anat Embryol (Berl)* **171**, 1–20.

Feldman SG & Kruger L (1980). An axonal transport study of the ascending projection of medial lemniscal neurons in the rat. *J Comp Neurol* **192**, 427–454.

Franklin KBJ & George P (2007). *The Mouse Brain in Stereotaxic Coordinates Third Edition*. Elsevier, New York.

Gaese BH & Johnen A (2000). Coding for auditory space in the superior colliculus of the rat. *Eur J Neurosci* **12**, 1739–1752.

Gale SD & Murphy GJ (2014). Distinct representation and distribution of visual information by specific cell types in mouse superficial superior colliculus. *J Neurosci* **34**, 13458–13471.

García Del Caño G, Uria I, Gerrikagoitia I & Martínez-Millan L (2004).

Connection from the Dorsal Column Nuclei to the Superior Colliculus in the Rat: Topographical Organization and Somatotopic Specific Plasticity in Response to Neonatal Enucleation. *J Comp Neurol* **468**, 410–424.

- Grantyn A & Grantyn R (1982). Axonal Patterns and Sites of Termination of Cat Superior Colliculus Neurons Projecting in the Tecto-Bulbo-Spinal Tract. *Exp Brain Res* **46**, 243–256.
- Grantyn A, Jacques VO & Berthoz A (1987). Reticulo-spinal neurons participating in the control of synergic eye and head movements during orienting in the cat. *Exp Brain Res* **66**, 355–377.
- Graybiel AM (1975). Anatomical organization of retinotectal afferents in the cat: An autodiographic study. *Brain Res* **96**, 1–23.
- Grothe B (2003). New roles for synaptic inhibition in sound localization. *Nat Rev Neurosci* **4**, 1–11.
- Grothe B & Pecka M (2014). The natural history of sound localization in mammals – a story of neuronal inhibition. *Front Neural Circuits* **8**, 1–19.
- Grothe B, Pecka M & McAlpine D (2010). Mechanisms of Sound Localization in Mammals. *Physiol Rev* **90**, 983–1012.
- Grundy D (2015). Principles and standards for reporting animal experiments in The Journal of Physiology and Experimental Physiology. *J Physiol* **593**, 2547–2549.
- Harting JK & Van Lieshout DP (1991). Spatial relationships of axons arising from the substantia nigra, spinal trigeminal nucleus, and pedunculo-pontine tegmental nucleus within the intermediate gray of the cat superior colliculus. *J Comp Neurol* **305**, 543–558.
- Harting JK & Van Lieshout DP (2000). Projections from the rostral pole of the inferior colliculus to the cat superior colliculus. *Brain Res* **881**, 244–247.
- Helms MC, Özen G & Hall WC (2004). Organization of the intermediate gray layer of the superior colliculus. I. Intrinsic vertical connections. *J*

*Neurophysiol* **91**, 1706–1715.

Henkel CK (1981). Afferent Sources of a Lateral Midbrain Tegmental Zone Associated With the Pinnae in the Cat as Mapped by Retrograde Transport of Horseradish Peroxidase. *J Comp Neurol* **203**, 213–226.

Hikosaka O & Wurtz RH (1983). Visual and oculomotor functions of monkey substantia nigra pars reticulata. I. Relation of visual and auditory responses to saccades. *J Neurophysiol* **49**, 1268–1284.

Hu H, Gan J & Jonas P (2014). Fast-spiking, parvalbumin+ GABAergic interneurons: From cellular design to microcircuit function. *Science* (80- ); DOI: 10.1126/science.1255263.

Hubel DH, LeVay S & Wiesel TN (1975). Mode of termination of retinotectal fibers in macaque monkey: An autoradiographic study. *Brain Res* **96**, 25–40.

Huerta MF, Frankfurter AJ & Harting JK (1981). The trigeminocollicular projection in the cat: Patch-like endings within the intermediate gray. *Brain Res* **211**, 1–13.

Huerta MF & Harting JK (1982). Projections of the superior colliculus to the supraspinal nucleus and the cervical spinal cord gray of the cat. *Brain Res* **242**, 326–331.

Inayat S, Barchini J, Chen H, Feng L, Liu X & Cang J (2015). Neurons in the most superficial lamina of the mouse superior colliculus are highly selective for stimulus direction. *J Neurosci* **35**, 7992–8003.

Isa T, Endo T & Saito Y (1998). The visuo-motor pathway in the local circuit of the rat superior colliculus. *J Neurosci* **18**, 8496–8504.

Jiang ZD, Moore DR & King AJ (1997). Sources of subcortical projections to the superior colliculus in the ferret. *Brain Res* **755**, 279–292.

- Kanaseki T & Sprague JM (1974). Anatomical organization of pretectal nuclei and tectal laminae in the cat. *J Comp Neurol* **158**, 319–337.
- Kardamakis AA, Saitoh K & Grillner S (2015). Tectal microcircuit generating visual selection commands on gaze-controlling neurons. *Proc Natl Acad Sci* **112**, 1956–1965.
- Katz LC & Dalva MB (1994). Scanning laser photostimulation: a new approach for analyzing brain circuits. *J Neurosci Methods* **54**, 205–218.
- Killackey HP & Erzurumlu RS (1981). Trigeminal projections to the superior colliculus of the rat. *J Comp Neurol* **201**, 221–242.
- King a J & Hutchings ME (1987). Spatial response properties of acoustically responsive neurons in the superior colliculus of the ferret: a map of auditory space. *J Neurophysiol* **57**, 596–624.
- King AJ, Jiang ZD & Moore DR (1998). Auditory brainstem projections to the ferret superior colliculus: Anatomical contribution to the neural coding of sound azimuth. *J Comp Neurol* **390**, 342–365.
- Knudsen EI (1982). Auditory and Visual Maps of Space in the Optic Tectum of the Owl. *J Neurosci* **2**, 1177–1194.
- Knudsen EI & Knudsen PF (1983). Space-Mapped auditory projections from the inferior colliculus to the optic tectum in the barn owl (*Tyto alba*). *J Comp Neurol* **218**, 187–196.
- Knudsen EI & Konishi M (1978). Space and frequency are represented separately in auditory midbrain of the owl. *J Neurophysiol* **41**, 870–884.
- Kudo M & Niimi K (1980). Ascending projections of the inferior colliculus in the cat: an audiographic study. *J Comp Neurol* **191**, 545–556.



- Lee J & Groh JM (2014). Different stimuli, different spatial codes: A visual map and an auditory rate code for oculomotor space in the primate superior colliculus. *PLoS One*; DOI: 10.1371/journal.pone.0085017.
- Lee PH, Helms MC, Augustine GJ & Hall WC (1997). Role of intrinsic synaptic circuitry in collicular sensorimotor integration. *Proc Natl Acad Sci* **94**, 13299–13304.
- Lesicko AMH, Hristova TS, Maigler KC & Llano DA (2016). Connectional modularity of top-down and bottom-up multimodal inputs to the lateral cortex of the mouse inferior colliculus. *J Neurosci* **36**, 11037–11050.
- Lesicko AMH & Llano DA (2018). Neurons projecting from the lateral cortex of the inferior colliculus to the superior colliculus are found in auditory-recipient extra-modular zones PS 51. In *41st Annual MidWinter Meeting, Association for Research in Otolaryngology*, pp. 29–30.
- Luksch H (2009). Optic Tectum: Sensorimotor Integration. *Encycl Neurosci* 263–269.
- Luksch H, Cox K, Karten HJ & Rwh ZI Der (1998). Bottlebrush Dendritic Endings and Large Dendritic Fields : Motion-Detecting Neurons in the Tectofugal Pathway. *J Comp Neurol* **396**, 399–414.
- Luksch H & Golz S (2003). Anatomy and physiology of horizontal cells in layer 5b of the chicken optic tectum. *J Chem Neuroanat* **25**, 185–194.
- Luksch H, Karten HJ, Kleinfeld D & Wessel R (2001). Chattering and differential signal processing in identified motion-sensitive neurons of parallel visual pathways in the chick tectum. *J Neurosci* **21**, 6440–6446.
- Lund RD, Land PW & Boles J (1980). Normal and abnormal uncrossed retinotectal pathways in rats: An HRP study in adults. *J Comp Neurol* **189**,

711–720.

Lünenburger L, Kleiser R, Stuphorn V, Miller LE & Hoffmann KP (2001). A possible role of the superior colliculus in eye-hand coordination. *Prog Brain Res* **134**, 109–125.

Ma TP, Cheng H -W, Czech JA & Rafols JA (1990). Intermediate and deep layers of the macaque superior colliculus: A golgi study. *J Comp Neurol* **295**, 92–110.

Maier JX & Groh JM (2009). Multisensory guidance of orienting behavior. *Hear Res* **258**, 106–112.

Major DE, Luksch H & Karten HJ (2000). Bottlebrush dendritic endings and large dendritic fields: Motion- detecting neurons in the mammalian tectum. *J Comp Neurol* **423**, 243–260.

Major DE, Rodman HR, Libedinsky C & Karten HJ (2003). Pattern of retinal projections in the California ground squirrel (*Spermophilus beecheyi*): Anterograde tracing study using cholera toxin. *J Comp Neurol* **463**, 317–340.

Mana S & Chevalier G (2001). The fine organization of nigro-collicular channels with additional observations of their relationships with acetylcholinesterase in the rat. *Neuroscience* **106**, 357–374.

May J, Vidal P & Baker R (1990). Synaptic Organization of Tectal-Facial Pathways in Cat II . Synaptic Potentials Following Midbrain Tegmentum Stimulation. *J Neurophysiol* **64**, 381–402.

May PJ (2006). The mammalian superior colliculus: Laminar structure and connections. *Prog Brain Res* **151**, 321–378.

May PJ & Porter JD (1992). The laminar distribution of macaque tectobulbar and tectospinal neurons. *Vis Neurosci* **8**, 257–276.

- Meininger V, Pol D & Derer P (1986). The inferior colliculus of the mouse. A Nissl and Golgi study. *Neuroscience* **17**, 1159–1179.
- Mellott JG, Beebe NL & Schofield BR (2018). GABAergic and non-GABAergic projections to the superior colliculus from the auditory brainstem. *Brain Struct Funct* **0**, 1–14.
- Meredith MA & Stein BE (1986). Visual, auditory, and somatosensory convergence on cells in superior colliculus results in multisensory integration. *J Neurophysiol* **56**, 640–662.
- Middlebrooks C & Knudsen EI (1984). A neural code for auditory space in the cat's superior colliculus. *J Neurosci* **4**, 2621–2634.
- Middlebrooks JC & Knudsen EI (1987). Changes in external ear position modify the spatial tuning of auditory units in the cat's superior colliculus. *J Neurophysiol* **57**, 672–687.
- Miyashita T, Shao YR, Chung J, Pourzia O & Feldman DE (2013). Long-term channelrhodopsin-2 (ChR2) expression can induce abnormal axonal morphology and targeting in cerebral cortex. *Front Neural Circuits* **7**, 1–10.
- Moschovakis AK & Karabelas AB (1985). Observations on the somatodendritic morphology and axonal trajectory of intracellularly HRP-labeled efferent neurons located in the deeper layers of the superior colliculus of the cat. *J Comp Neurol* **239**, 276–308.
- Murray EA & Coulter JD (1982). Organization of tectospinal neurons in the cat and rat superior colliculus. *Brain Res* **243**, 201–214.
- Nathanson JL, Yanagawa Y, Obata K & Callaway EM (2009). Preferential labelling of inhibitory and excitatory cortical neurons by endogenous tropism of adeno-associated virus and lentivirus vectors. *Neuroscience* **161**,

441–450.

Nodal FR, Doubell TP, Jiang ZD, Thompson ID & King AJ (2005). Development of the projection from the nucleus of the brachium of the inferior colliculus to the superior colliculus in the ferret. *J Comp Neurol* **485**, 202–217.

Özen G, Augustine GJ & Hall WC (2000). Contribution of Superficial Layer Neurons to Premotor Bursts in the Superior Colliculus. *J Neurophysiol* **84**, 460–471.

Palmer AR & King AJ (1982). The representation of auditory space in the mammalian superior colliculus. *Nature* **299**, 248–249.

Petreaanu L, Huber D, Sobczyk A & Svoboda K (2007). Channelrhodopsin-2-assisted circuit mapping of long-range callosal projections. *Nat Neurosci* **10**, 663–668.

Petreaanu L, Mao T, Sternson SM & Svoboda K (2009). The subcellular organization of neocortical excitatory connections. *Nature* **457**, 1142–1145.

Pettit DL, Helms MC, Lee P, Augustine GJ & Hall WC (1999). Local Excitatory Circuits in the Intermediate Gray Layer of the Superior Colliculus. *J Neurophysiol* **81**, 1424–1427.

Phongphanphanee P, Kaneda K & Isa T (2008). Spatiotemporal Profiles of Field Potentials in Mouse Superior Colliculus Analyzed by Multichannel Recording. *J Neurosci* **28**, 9309–9318.

Pollack JG & Hickey TL (1979). The distribution of retino–collicular axon terminals in rhesus monkey. *J Comp Neurol* **185**, 587–602.

Saito Y & Isa T (1999). Electrophysiological and morphological properties of neurons in the rat superior colliculus. I. Neurons in the intermediate layer. *J Neurophysiol* **82**, 754–767.

- Saito Y & Isa T (2003). Local excitatory network and NMDA receptor activation generate a synchronous and bursting command from the superior colliculus. *J Neurosci* **23**, 5854–5864.
- Schiller PH & Stryker M (1972). Single-unit recording and stimulation in superior colliculus of the alert rhesus monkey. *J Neurophysiol* **35**, 915–924.
- Schnupp JW & King AJ (1997). Coding for auditory space in the nucleus of the brachium of the inferior colliculus in the ferret. *J Neurophysiol* **78**, 2717–2731.
- Shang C, Liu Z, Chen Z, Shi Y, Wang Q, Liu S, Li D & Cao P (2015). A parvalbumin-positive excitatory visual pathway to trigger fear responses in mice. *Science (80- )* **348**, 1472–1477.
- Shepherd GMG (2012). Circuit mapping by ultraviolet uncaging of glutamate. *Cold Spring Harb Protoc* **7**, 998–1004.
- Sholl BDA (1953). Dendritic organization in the neurons of the visual and motor cortices of the cat. *J Anat* **87**, 387–407.
- Skaliora I, Doubell TP, Holmes NP, Nodal FR & King AJ (2004). Functional topography of converging visual and auditory inputs to neurons in the rat superior colliculus. *J Neurophysiol* **92**, 2933–2946.
- Sooksawate T, Isa K, Behan M, Yanagawa Y & Isa T (2011). Organization of GABAergic inhibition in the motor output layer of the superior colliculus. *Eur J Neurosci* **33**, 421–432.
- Sooksawate T, Saito Y & Isa T (2005). Electrophysiological and morphological properties of identified crossed tecto-reticular neurons in the rat superior colliculus. *Neurosci Res* **52**, 174–184.
- Sparks DL (1986). Translation of sensory signals into commands for control of

saccadic eye movements: role of primate superior colliculus. *Physiol Rev* **66**, 118–171.

Sprague JM & Meikle THJ (1965). The Role of the Superior Colliculus Behavior in Visually Guided Behavior. *Exp Neurol* **11**, 115–146.

Stein BE & Clamann HP (1981). Control of Pinna Movements and Sensorimotor Register in Cat Superior Colliculus. *Brain, Behav Evol* **19**, 180–192.

Stein BE, Magalhaes-Castro B & Kruger L (1975). Superior colliculus: visuotopic-somatotopic overlap. *Science* **189**, 224–226.

Stein BE, Meredith AM, W HS & McDade L (1989). Behavioral Indices of Multisensory Integration: Orientation to Visual Cues is Affected by Auditory Stimuli. *J Cogn Neurosci* **1**, 12–24.

Stein BE & Stanford TR (2008). Multisensory integration: Current issues from the perspective of the single neuron. *Nat Rev Neurosci* **9**, 255–266.

Stein BE, Stanford TR & Rowland BA (2014). Development of multisensory integration from the perspective of the individual neuron. *Nat Rev Neurosci* **15**, 520–535.

Suter B, O'Connor T, Iyer V, Petreanu L, Hooks B, Kiritani T, Svoboda K & Sheperd G (2010). Ephus: multipurpose data acquisition software for neuroscience experiments. *Front Neural Circuits* **4**, 1–12.

Tehovnik EJ (1989). Head and body movements evoked electrically from the caudal superior colliculus of rats: Pulse frequency effects. *Behav Brain Res* **34**, 71–78.

Tigges J & Tigges M (1981). Distribution of retinofugal and corticofugal axon terminals in the superior colliculus of squirrel monkey. *Investig Ophthalmol Vis Sci* **20**, 149–158.

- Triplett JW, Phan A, Yamada J & Feldheim DA (2012). Alignment of Multimodal Sensory Input in the Superior Colliculus through a Gradient-Matching Mechanism. *J Neurosci* **32**, 5264–5271.
- Truszkowski TLS, Carrillo OA, Bleier J, Ramirez-Vizcarrondo CM, Felch DL, McQuillan M, Truszkowski CP, Khakhalin AS & Aizenman CD (2017). A cellular mechanism for inverse effectiveness in multisensory integration. *Elife* **6**, 1–11.
- Villalobos CA, Wu Q, Lee PH, May PJ & Basso MA (2018). Parvalbumin and GABA Microcircuits in the Mouse Superior Colliculus. *Front Neural Circuits* **12**, 1–16.
- Wiberg M, Westman J & Blomqvist A (1984). The projection to the mesencephalon from the sensory trigeminal nuclei. An anatomical study in the cat. *Brain Res* **311**, 225–244.
- Wiberg M, Westman J & Blomqvist A (1987). Somatosensory projection to the mesencephalon: An anatomical study in the monkey. *J Comp Neurol* **264**, 92–117.
- Wilson JJ, Alexandre N, Trentin C & Tripodi M (2018). Three-Dimensional Representation of Motor Space in the Mouse Superior Colliculus. *Curr Biol* **28**, 1744–1755.e12.
- Winer J a, Larue DT, Diehl JJ & Hefti BJ (1998). Auditory cortical projections to the cat inferior colliculus. *J Comp Neurol* **400**, 147–174.
- Winer J & Schreiner C (2005). *The Inferior Colliculus*. Springer Science+Business Media, New York.
- Wise SP & Jones EG (1977). Somatotopic and columnar organization in the corticotectal projection of the rat somatic sensory cortex. *Brain Res* **133**, 223–

235.

Wurtz RH (2018). Corollary Discharge Contributions to Perceptual Continuity Across Saccades. *Annu Rev Vis Sci* **4**, 215–237.

Zingg B, Chou X lin, Zhang Z gang, Mesik L, Liang F, Tao HW & Zhang LI (2017). AAV-Mediated Anterograde Transsynaptic Tagging: Mapping Corticocollicular Input-Defined Neural Pathways for Defense Behaviors. *Neuron* **93**, 33–47.



## **PUBLICATION**

Bednárová V, Grothe B, Myoga MH (2018). Complex and spatially segregated auditory inputs of the mouse superior colliculus. *J Physiol*

<https://doi.org/10.1113/JP276370>



# CURRICULUM VITAE

Veronika Bednářová

## Education

---

- Oct 2014 – present      **PhD in Systemic Neurosciences**  
**Graduate School of Systemic Neurosciences (GSN),**  
**Ludwig-Maximilians-Universität (LMU), Munich**  
  
In the laboratory of Prof. Grothe, under supervision of M. Myoga I investigated auditory circuits of the mouse superior colliculus
- Oct 2013 – Sept 2014      **Fast-track PhD, GSN, LMU, Munich**  
  
Rigorous year of courses covering all modern neuroscience research – from computation, through molecules and systems to philosophy
- Sept 2019 – June 2012      **BSc Hons in Anatomy, Developmental and Human Biology, King's College London, London, United Kingdom**  
  
First two years provided a thorough grounding in cellular, developmental, and human biology with elective courses in second and third years focusing on neuroscience

## Scholarships and prizes

---

- 2018      Third place poster prize, GSN Retreat, LMU Munich
- 2017 – 2018      Stipend from the GSN, LMU Munich
- 2015 – 2017      Boehringer Ingelheim Fonds PhD Fellowship
- 2013 – 2015      Stipend from the GSN, LMU Munich
- 2012      Awarded Student Laboratory Experience Grant from British Society for Neuroendocrinology. (£1,200 and £1,000 for the cost of consumables)
- 2011      First place poster prize, Amgen Scholars, Cambridge, UK

## Language and computing skills

---

Languages	Slovak (mother tongue), English (expert), German (conversational)
Computing	MS Office, Matlab, Python, Adobe Illustrator

## Additional courses and research experience

---

Spring 2016	<b>Communication Seminar, Cold Spring Harbor, USA</b>  Boehringer Ingelheim Fonds led seminar on presentation skills, writing skills, and Adobe Illustrator skills
Summer 2015	<b>Neurophotonics summer School, Quebec, Canada</b>  10-days long course on various super-resolution techniques with hands-on 3-days project
Since 2013	<b>Soft skill courses offered by the GSN</b>  A variety of 2-day courses on topics including PhD management, scientific writing, oral presentation and poster skills
Summer 2012	<b>Research Internship, Division of Women's Health, King's College London, United Kingdom</b>  Anterograde tracing of neurones of the amygdaloid nucleus, practical experience with immunocytochemistry, rodent handling
Summer 2011	<b>Amgen Scholars Programme, Karolinska Institutet, Stockholm, Sweden</b>  Practical utilization of ELISA for detection of cytomegalovirus antibodies, development of practical research skills

## EIDESSTATTLICHE VERSICHERUNG/AFFIDAVIT

Hiermit versichere ich an Eides statt, dass ich die vorliegende Dissertation „**Complex and spatially segregated auditory inputs of the mouse superior colliculus**“ selbstständig angefertigt habe, mich außer der angegebenen keiner weiteren Hilfsmittel bedient und alle Erkenntnisse, die aus dem Schrifttum ganz oder annähernd übernommen sind, als solche kenntlich gemacht und nach ihrer Herkunft unter Bezeichnung der Fundstelle einzeln nachgewiesen habe.

I hereby confirm that the dissertation „**Complex and spatially segregated auditory inputs of the mouse superior colliculus**“ is the result of my own work and that I have only used sources or materials listed and specified in the dissertation.

15/October/2018

---

München, den (Munich, date)

Veronika Bednárová

---

Unterschrift (signature)



## DECLARATION OF AUTHOR CONTRIBUTION

Experimental design: VB, MHM, BG

Setup design/assembly: VB, MHM

Conducting all experiments: VB

Analysis all experiments, including writing analysis scripts in Matlab: VB, MHM

Visualizing the results of experiments: VB

Supervision, project administration, funding acquisition: MHM, BG

Thesis writing: VB

Thesis revising: VB, MHM, BG

Date, place:

Signature Veronika Bednárová:

Signature Dr. Michael H Myoga:

Signature Prof. Dr. Grothe:

